LOCAL STRAIN DEVELOPMENT IN HIGH TEMPERATURE RUAL INTERMETALLIC ALLOYS

by

Aomin Wu

A dissertation submitted in partial fulfillment
of the requirements for the degree of
Doctor of Philosophy
(Materials Science and Engineering)
in The University of Michigan
2006

Doctoral Committee:

Professor Tresa M. Pollock, Chair
Professor Emeritus Ronald Gibala
Assistant Professor Krishnakumar R. Garikipati
Professor Marc De Graef, Carnegie Mellon University

© Aomin Wu 2006
All Rights Reserved

DEDICATION

To my family

ACKNOWLEDGEMENTS

It's been an extremely memorable experience for me during this four and a half years study at the University of Michigan. The successful completion of my Ph.D. degree, as partially represented by the thesis, is not only due to the efforts of myself, but also due to the generous help and patient guidance of a number of people, most notably my advisor Professor Tresa M. Pollock, and Dr. Qiang Feng. The insightful thoughts and comments by the dissertation committee on my research are highly appreciated. My special thanks go to Chris Torbet for his ingenious engineering designs that are critical to the success of my experiments. And I would also like to extend my great gratitude to the supporting staffs in EMAL at the University of Michigan, who have made my research progress as smoothly as possible. Of course, there are also the members in Pollock's and Jones' research groups I would like to thank for sharing many of the happy moments during these past several years.

Finally, I would like to thank my family for their ever lasting support, encouragement and inspiration since the first day I came into this world.

TABLE OF CONTENTS

LIST OF TABLES

LIST OF FIGURES

ABSTRACT

LOCAL STRAIN DEVELOPMENT IN HIGH TEMPERATURE RUAL INTERMETALLIC ALLOYS

by

Aomin Wu

Chair: Tresa M. Pollock

The limited ductility in many high temperature B2 aluminides has significantly hindered their integration into structural components in bulk form in areas such as aircraft engines and commercial power generators. Compared to other high temperature B2 aluminides, RuAl displays a very high melting temperature (T_m ~2068˚C) and unusually high compression ductility, which is thought to arise from its diverse slip behavior and the two phase microstructure. The objective of this study is to examine the plastic behavior of this compound in greater detail, with emphasis on developing a quantitative understanding of the straining processes at the scale of the microstructure. Several advanced experimental techniques, including a newly developed surface displacement mapping technique, orientation imaging microscopy, nanoindentation, focused ion beam and transmission electron microscopy are utilized to investigate the strain development behavior at the local microstructural scale of three different RuAl alloys, each with varying volume fraction of a secondary δ-Ru phase. This research is unique in that it directly connects the local straining behavior to the microstructure as well as to the underlying dislocation activity. It is found that a

significant degree of strain heterogeneity developed in RuAl alloys after a few percent nominal deformation, with strains varying by a factor of 10～300％ from the mean imposed strains within the neighborhood of several grains. The characteristics of such heterogeneity vary with the amount of δ-Ru phase present. This δ phase serves as a compliant layer by deforming preferentially during deformation and redistributing strain in the local microstructural areas. In single phase RuAl, the straining of grains is dominated by the <110>{110} slip system in comparison to the <100>{110} system under the local microstructural conditions studied. By examining the details of strain heterogeneity and local lattice distortion, it is found that large strain gradients in the vicinity of grain boundaries are not associated with variations in the density of geometrically necessary dislocations.

CHAPTER 1

INTRODUCTION

This chapter covers the basics of the plastic behavior of B2 aluminide, the deformation characteristics of RuAl, including relevant microstructural features that affect its plastic behavior. Also included is a brief review on strain heterogeneity and the role of geometrically necessary dislocations. Finally, the objectives and experimental implementation of the research are outlined with a description of key experimental techniques.

1.1 Background of RuAl Intermetallic Alloys

There has been a great deal of interest in recent years in high temperature intermetallic compounds, which exhibit a combination of high melting point, high specific strength, and good resistance to oxidation and corrosion [1, 2]. However, many intermetallics are known for their low tensile ductility at ambient temperatures. Intermetallics that do possess finite room temperature ductility, such as TiAl, often suffer from a high degree of variability in this property [3]. In the TiAl system, premature failure is associated with microstructural regions of the order of several grain diameters that accumulate high strains locally. Such strain heterogeneities are also observed in multi-grain finite element simulations of TiAl [4]. However, the origin of such experimentally observed strain heterogeneities and the corresponding models required to capture such plastic behavior are not yet well understood.

The intermetallic alloy RuAl, with a melting temperature of 2068˚C, displays a very unusual plastic behavior compared to other types of B2 intermetallics [5-11]. It is for this reason that RuAl has recently been considered as a bond coat for ZrO_2-based thermal barrier coatings (TBCs) [12, 13]. The high temperature capability and potentially excellent mechanical behavior of RuAl has triggered

extensive interest in this particular alloy with the expectation that one day it could be applied in bulk form in high temperature structural components. However, much investigation is still needed to fully understand the plastic behavior as well as other properties before this system can be utilized on a commercial scale.

1.2 Deformation Characteristics of B2 Aluminides

Intermetallic B2 aluminides have been the subject of a wide range of microstructure, processing and deformation studies [2, 14-16]. However, most high temperature B2 intermetallics exhibit brittle behavior. Deformation and transmission electron microscopy studies on B2 aluminides reveal a spectrum of slip behavior with <100>, <110> and/or <111> dislocation glide, as shown in Fig. 1.1, depending on alloy composition and deformation temperature [2]. At ambient temperature, the plastic behavior of low melting point compounds is distinctively different from high melting point compounds. Slip in low temperature compounds such as FeAl occurs primarily by glide of <111> dislocations on {110} planes. Conversely, in high temperature compounds such as NiAl, deformation is controlled by motion of <100> dislocations on {100} and {110} planes [2, 15]. Regardless of slip system, mechanical properties may also be limited by dislocation mobility in high temperature B2 aluminides [8]. Thus brittleness may arise due to lack of dislocation mobility and/or insufficient number of independent slip systems to satisfy the Von Mises criterion [17]. NiAl is an example of a high temperature B2 aluminide without sufficient dislocation mobility [8] or a sufficient number of slip systems [15]. In this case, polycrystalline NiAl fails in a brittle manner at low strains.

The intermetallic RuAl, with a melting temperature of 2068˚C, exhibits unusual plastic behavior compared to other high temperature B2 intermetallics. It possesses unusually high room temperature “chisel toughness” [5] and displays diverse deformation characteristics [6-11, 18]. In binary RuAl, deformation occurs on <100>{110} and <110>{110} slip systems [7], whereas in ternary RuAl-based systems with additions of either Pt or Ta, dislocation glide occurs primarily on the <111>{110} system [9-11]. Slip on either a combination of <100>{110} and

<110>{110} systems (binary RuAl) or <111>{110} systems (ternary RuAl) can provide sufficient modes of deformation for compatible straining of a polycrystalline material. Accompanying the ample number of slip systems is a high apparent dislocation mobility in this class of materials [8, 10, 11].

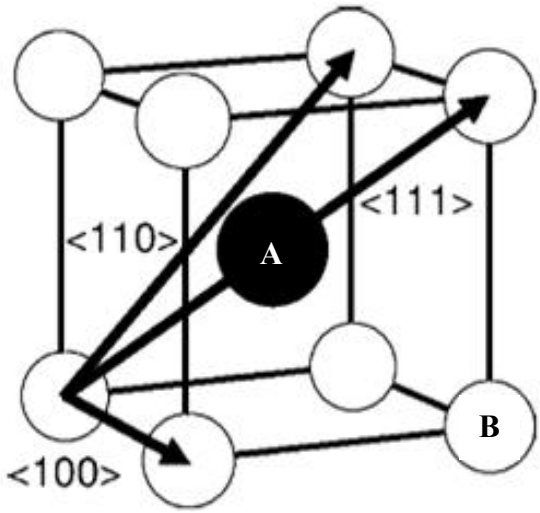

Fig. 1.1 B2 structure with possible slip vectors.

1.3 Microstructure and Phases in RuAl

The B2 intermetallic RuAl only exists within a narrow compositional range near stoichiometry, according to the Ru-Al binary phase diagram [19], Fig. 1.2. Most RuAl-based alloys often have a two phase microstructure consisting of a B2 RuAl matrix and HCP Ru-rich δ phase, as shown in Fig. 1.3. The δ phase usually appears along grain boundaries and, with increasing levels of Ru, within grain interiors. Such secondary δ phase is thought to significantly affect the mechanical behavior of RuAl-based alloys [20, 21]. Research by Fleisher *et al.* [20] has shown that the two phase version of RuAl alloys were tougher than the Al rich single phase material. In addition, the Ru-rich alloys exhibit a higher degree of transgranular fracture, while the Al-rich alloys are prone to low energy intergranular fracture. Wolff [21] suggested that the grain boundary δ phase in Ru-rich alloys adopts the function of a compliant layer, which modifies the local cracking and deformation processes at the crystalline interfaces, aiding grain to grain compatibility during deformation. Wolff and coworkers further investigated the mechanical properties and the role of the

grain boundary δ phase in several ternary RuAl alloy systems with addition of Ni, Co and Ti. They found that the grain boundary δ phases in all the alloy systems studied had higher measured hardness value than the RuAl matrix before deformation [22]. They suggested that the improved toughness in Ru-rich two phase alloys possibly has to do with the additional deformability of HCP δ phase under local grain boundary constraints. Nonetheless, the approach Wolff *et al.* used to compare the relative hardness of the two different phases was questionable, for they didn't take into account the indentation size effect arising from using different loading force [23], particularly in the lower end of the loading spectrum.

Although the exact mechanism that leads to the improved ductility and toughness in the Ru-rich RuAl alloys is still unclear, the positive contribution of grain boundary δ phase to the overall mechanical response of RuAl is apparent. Experiments are needed to better understand the role of the second phase in plastic deformation in order to provide input for the optimization of the microstructure for future alloy design.

The mechanical properties of RuAl-based alloys are also affected by several different alloy addition elements, most notably boron, which was found to increase the ductility of the stoichiometric and Ru-rich alloys approximately two fold with only 0.5% addition [6]. However, the exact mechanism through which boron contributes to the improved ductility of RuAl is still unclear [24]. Other alloying additions that have been discovered to have positive effects on the mechanical properties of RuAl include Sc, which aids to increase the high temperature strength without deteriorating room temperature toughness [6]; Ta and Pt, which alter the slip behavior of RuAl from a combination of <100>{110} & <110>{110} to <111>{110} as mentioned earlier [9-11].

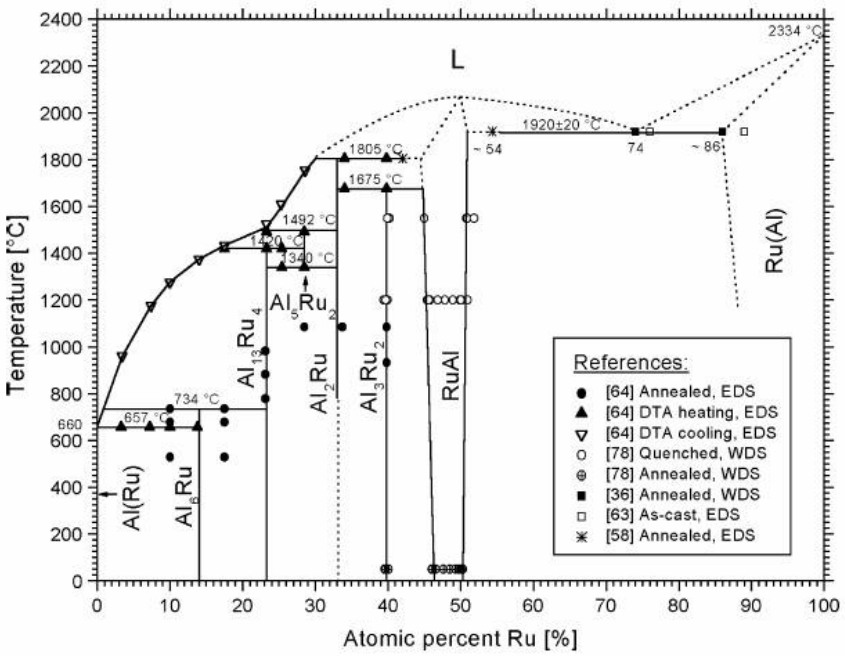

Fig. 1.2 Current Ru-Al binary phase diagram, adapted from Mücklich *et al.* [19]

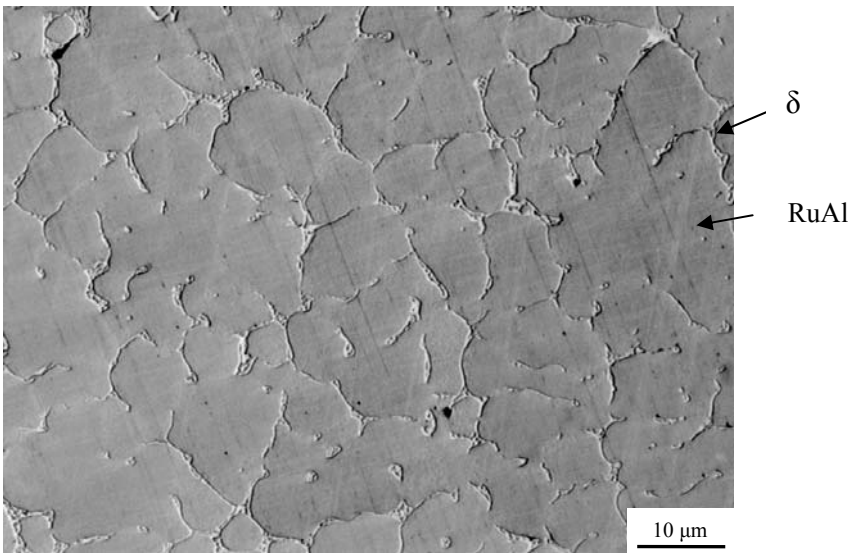

Fig. 1.3 Two phase microstructure of 53Ru47Al

1.4 Deformation Heterogeneity and Geometrically Necessary Dislocation

To understand the plastic behavior of RuAl at the microstructural scale, experimental study of its deformation at this scale is inevitable. In addition, such experimental investigation also provides an opportunity to assess more general issues related to deformation heterogeneity at the micro scale relevant to the broader class of intermetallic and metallic materials. Particularly, the author is interested in evaluating the relationship between deformation heterogeneity and geometrically necessary dislocation. The contemporary viewpoint of this topic is briefly mentioned below.

When key microstructural features are of the scale of a few microns or smaller, the deformation of materials often displays unusual behavior in that "size effects" are frequently observed. In a number of experiments including torsion of copper wire [25], bending of ultra thin beams [26], micro indentation of metal [27-29] and deformation of composites [30], the strength of the materials increased significantly when the scale characterizing deformation heterogeneity reduced to the order of several tens of microns. However, such size dependent behaviors were not observed in tension tests at the same scale [25]. The unique feature associated with the aforementioned experiments which exhibited strengthening effects at the micro scale is the development of large strain gradients. It is believed that the failure of classical plasticity theories to predict size-dependent plastic behavior is due to their inability to capture the role of strain gradients in the constitutive equations with explicit length scale parameters.

In recent years, extensive efforts have been devoted to developing new strain gradient plasticity theories that are scale sensitive [25, 31-34]. In addressing the issue of strain gradients, one widely-adopted way is to subdivide dislocations into two distinctive categories, statistically stored dislocations (SSD) and geometrically necessary dislocations (GND), to better characterize their roles during material hardening. By definition SSDs are those that glide and are randomly trapped by the stress fields of each other and provide hardening, while GNDs are those that have the

additional role to support lattice curvature in the presence of strain gradients [35]. The classic Taylor relation that associates shear strength with the total dislocation density has then been modified accordingly to take into account the contribution from different dislocations [25]:

$$\tau = C'Gb\sqrt{\rho_{SSD} + \rho_{GND}} \tag{1.1}$$

where G is the shear modulus, b the magnitude of Burgers vector, C' is a constant, and ρ_{SSD} and ρ_{GND} are the density of statistically store dislocations and geometrically necessary dislocations, respectively. Strain gradient theory based on GNDs suggests that the density of GNDs scales with the magnitude of lattice curvature, since more GNDs are needed to support the higher degree of lattice incompatibility. Although the theory of GNDs has gained significant recognition, its theoretical robustness lacks critical experimental support, mainly due to the difficulty of measuring gradients of strain at micro scale along with the associated density of GNDs present. Recent advancements in orientation imaging microscopy (OIM) have enabled estimates of the density of GNDs through precise measurement of lattice distortions at localized areas [36-38]. This suggests a new path to examine the relationship between strain gradient and GND. The only critical information missing is the local strain gradient present at the same measured area.

The following briefly describes the theoretical framework for estimating the density of GNDs from the measured lattice curvature data:

The continuity requirement of the displacement field $\mathbf{u}(\mathbf{x})$ around any closed loop demands:

$$\oint_C du_i = \oint_C \beta_{ij} dx_j = 0 \tag{1.2}$$

where β_{ji} is the distortion tensor defined by $du_i=\beta_{ij}dx_j$, which describes the state of distortion around an infinitesimal neighborhood of position $\mathbf{x}$. The distortion tensor can be further separated into elastic and plastic components:

$$\beta_{ij} = \beta_{ij}^e + \beta_{ij}^p \tag{1.3}$$

Applying Stokes' theorem to equation (1.2) and substituting the distortion tensor by its different components results in:

$$\oiint_S (e_{rsi}\beta^e_{sj,r} + e_{rsi}\beta^p_{sj,r})n_j ds = 0 \tag{1.4}$$

where S is any continuous surface bounded by the loop C. Given that equation (1.4) holds true anywhere in the lattice, this requires:

$$e_{rsi}\beta^e_{sj,r} = -e_{rsi}\beta^p_{sj,r} \tag{1.5}$$

The integral of $e_{rsi}\beta^p_{sj,r}$ around a continuous surface bounded by a Burgers circuit yields the total plastic distortion within the circuit, which equals the net Burgers vector of the circuit:

$$B_i = -\oiint_S e_{rsi}\beta^p_{sj,r} n_j ds \tag{1.6}$$

while at the same time, the net Burgers vector can also be interpreted in terms of the dislocation tensor $\boldsymbol{\alpha}$:

$$B_i = \oiint_S \alpha_{ij} n_j ds \tag{1.7}$$

Taking into account equation (1.5), (1.6) and (1.7) gives:

$$\alpha_{ij} = e_{rsi}\beta^e_{sj,r} \tag{1.8}$$

By definition, the elastic distortion tensor consists of the elastic strain tensor $\boldsymbol{\varepsilon^e}$ and the elastic rotation tensor $\boldsymbol{\omega^e}$, which essentially describes the orientation change of the crystal lattice. Therefore, equation (1.8) can be rewritten as:

$$\alpha_{ij} = e_{rsi}(\varepsilon^e_{sj,r} + \omega^e_{sj,r}) \tag{1.9}$$

Upon removal of the long-range elastic stress field, the elastic strain term in (1.9) vanishes, and Nye's original formulation of the dislocation tensor [36] is obtained:

$$\alpha_{ij} = e_{rsi}\omega^e_{sj,r} \tag{1.10}$$

Equation (1.10) establishes a direction relationship between the dislocation tensor and the curvature of crystal lattice, which can be measured experimentally by OIM. On the other hand, Nye [36] shows that there exists a precise connection between the dislocation tensor and the local dislocation network in the neighborhood of interest:

$$\alpha_{ij} = \sum_{k=1}^{K} \rho^k b^k_i z^k_j \tag{1.11}$$

where K denotes the number of available dislocation type, and b^k and z^k denote the

Burgers vector and line direction of type k dislocations, respectively. Since GNDs are considered to support the curvature in the crystal lattice, the distortion contributed to $\boldsymbol{\alpha}$ is believed to result from GNDs.

When the types and density of GNDs are known, the dislocation tensor $\boldsymbol{\alpha}$ is precisely determined by equation (1.11). However, the reverse is not true given that there are essentially infinite combinations of dislocations that satisfy a certain shape distortion. Therefore, when estimating the total density of GNDs from the measured lattice curvature, a lower bound solution of the total density is adopted as the final result for it is considered to generate the minimum amount of distortion energy within the bulk.

1.5 Objectives and Experimental Implementation of the Research

Given the availability of multiple slip systems and the existence of different phases in RuAl, the aim of this research was to examine the plastic behavior of this compound in greater detail, with an emphasis on developing a quantitative understanding of the straining process at the scale of the microstructure. To accomplish this, a newly established experimental high-resolution surface displacement mapping technique [39] was employed to measure strains developed on a grain-to-grain basis. The influence of microstructure and slip system activity on strain distribution has been studied by: 1.) assessment of Schmid factors for possible slip systems within individual grains using EBSD-generated orientation data; 2.) analysis of straining patterns characterized via strain mapping, and 3.) characterization of post-deformed dislocation substructures within relevant grains via FIB-assisted removal of foils for TEM observation. The impact of the secondary Ru-rich δ phase on local straining was also analyzed through assessment of its hardness change during deformation by nano-indentation. In addition, part of the investigation has been devoted to understanding the strain heterogeneity developed at the local microstructural scale with a particular emphasis on the relationship between strain gradients and the density of geometrically necessary dislocations. GND density is estimated through the direct measurement of lattice curvature in the

post-deformed specimen via OIM. Results are compared to the strain distribution profiles at the same local area obtained by strain mapping. Since several complicated and relatively new experimental techniques are utilized in this research, it is worth describing each of them briefly.

1.5.1 Surface Displacement Mapping

The non-contact measurement of strain during deformation has been a subject of intensive research [40, 41]. Non-contact methods are obviously favored due to the minimum disturbance they impose on the measured targets. The frequently applied methods include Moire techniques [42], laser interferometry [43], holographic techniques [44], and speckle correlation techniques [45]. These techniques use either ordered or random grids projected onto the specimen surface. Following deformation and comparison to a reference grid of the same sort, it is possible to acquire displacement information, and therefore calculate strains. Such techniques can measure very small strains on sample surfaces but are not suited to small areas. In addition, all of these techniques require very stable optical setups during measurement and hence lack the flexibility to accommodate different testing requirements.

Direct measurement techniques [46] which apply physical grids to the sample surface and directly measure the distortion accompanying the deformation of the sample avoid the need for optical setups and, at the same time, can easily fit in different testing situations. These methods can provide displacement mapping to within the accuracy of one pixel.

The surface displacement mapping technique applied in the present research makes another leap forward from previous direct measurement techniques in that it not only increases precision of displacement mapping by utilizing the rich grayscale information within the images but also minimizes mapping errors by incorporating the entire marker locating and matching routines into computer programs so that the involvement of human operator is reduced to a minimum.

The application of surface displacement mapping starts by surface marker

preparation during which an ordered array of markers is deposited onto the well-polished sample surface by vacuum evaporation of Au through fine scale nickel mesh screen affixed to the surface. Markers made up of either Au have the advantage of generating strong back-scattered signals in the SEM due to their large atomic number. This enables them to have sharp contrast in the SEM images acquired under the back-scattered mode. Obtaining good markers is critical to the success of surface displacement mapping. Failure to do so will impose tremendous difficulties in the subsequent mapping procedures. Fig. 1.4 shows an example of both good markers and bad markers.

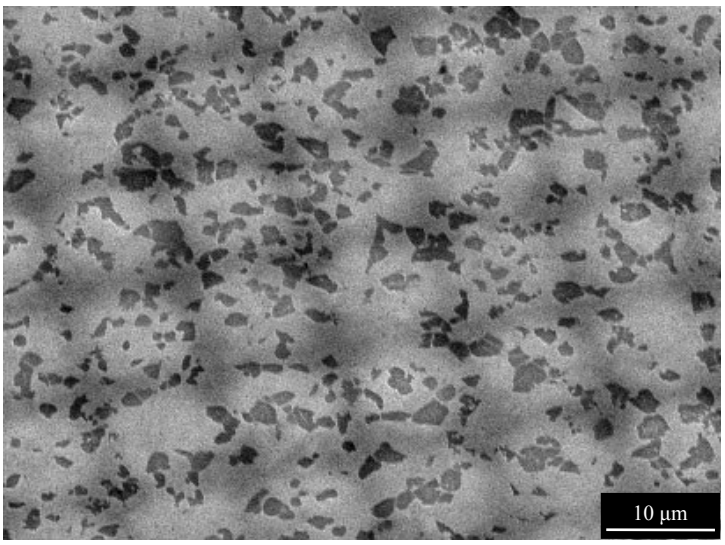

(a)

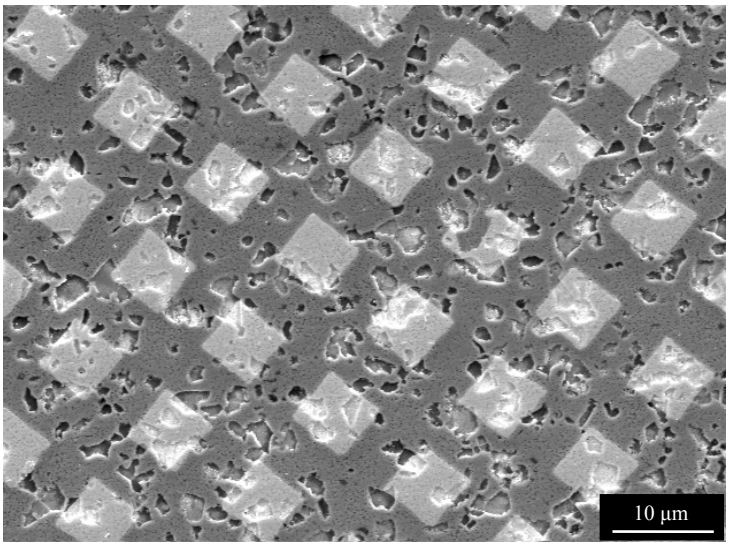

(b)

Fig. 1.4 Example of markers deposited on etched IN100, (a) markers are diffusive and poorly defined, (b) markers are crispy and clearly defined.

Following marker deposition, two images of a selected region of the microstructure (now covered with markers) are taken in the SEM, one before sample deformation and one after. These before/after images are then input to a computer program written in interactive data language (IDL) which automatically carries out a series of image processing algorithms to calculate displacements and strains. The program first asks the human operator to click on two adjacent markers through which it is able to determine the approximate marker spacing. The operator is then required to randomly choose three more markers so that the program can define a standard marker profile by averaging the information from the five initially identified. Armed with the digitized marker profile and marker spacing information, the program will then go on to determine the location of all the markers in both before and after images within sub pixel accuracy through a convolution algorithm that employs all the grayscale information within the images. The images are then aligned by manually selecting a common origin. Following that, for each of the markers in the before image, its counterpart in the deformed image is found by the program and the two markers are paired. The pairing procedure repeats for each marker in the before image until most of the markers are paired. A few near-edge markers are typically not considered due to a slight mismatch between the before and after images. The displacement of an individual marker is then calculated simply by subtracting the coordinates between marker in before and after images. After all displacements are found in this fashion, a polynomial fitting function maps the locations of the marker and its surrounding markers in the distorted image to the corresponding markers in the reference image through the following relation:

$$X_i = \sum_{i,j} K_{i,j} X_o^j Y_o^i \tag{1.12}$$

$$Y_i = \sum_{i,j} L_{i,j} X_o^j Y_o^i \tag{1.13}$$

where X_i and Y_i are locations of the marker in the after image, X_o and Y_o are locations in the before image, and $K_{i,j}$ and $L_{i,j}$ are the x and y coefficients of the

polynomial. Strains can then be calculated from the displacements obtained through the following equations:

$$\varepsilon_{xx} = \frac{\partial}{\partial X_o} \sum_{i,j} K_{i,j} X_o^j Y_o^i - 1 \tag{1.14}$$

$$\varepsilon_{yy} = \frac{\partial}{\partial Y_o} \sum_{i,j} L_{i,j} X_o^j Y_o^i - 1 \tag{1.15}$$

$$\gamma_{xy} = \frac{1}{2}\left(\frac{\partial}{\partial X_o} \sum_{i,j} L_{i,j} X_o^j Y_o^i + \frac{\partial}{\partial Y_o} \sum_{i,j} K_{i,j} X_o^j Y_o^i\right) \tag{1.16}$$

In addition to the individual strain components, a Von Mises effective strain is defined and used frequently to evaluate straining of the material. Note that since the out of plane displacements are not captured during the experiment, the surface displacement mapping technique is inherently two dimensional. Thus, the Von Mises effective strain is defined in a two dimensional context, assuming all the out of plane strain components to be zero:

$$\varepsilon_{eff} = \sqrt{\frac{2}{9}\left(\varepsilon_{xx}^{\ 2} + \varepsilon_{yy}^{\ 2} + (\varepsilon_{xx} - \varepsilon_{yy})^2 + 6\varepsilon_{xy}^{\ 2}\right)} \tag{1.17}$$

where $\varepsilon_{xz} = \varepsilon_{yz} = \varepsilon_{zz} = 0$

Application of this technique has proven to be successful for investigating local strain inhomogeneities. A prior study utilizing this technique has demonstrated close agreement between uniaxial macroscopically imposed strains and the same component of strain average over a large number of surface grains [39]. A more detailed description of the surface displacement technique can be found in the paper by Biery *et al.* [39].

1.5.2 Orientation Imaging Microscopy

As an important microstructural characterization tool for the investigation of

crystallographic orientations, orientation imaging microscopy (OIM®) utilizes the electron back-scattered diffraction (EBSD) patterns generated by an impinging electron beam upon a tilted sample surface to back calculate crystallographic orientations of the microstructure at the sample surface. By rastering the beam across an area of interest on the surface, complete three dimensional orientation information of the microstructure under survey can be obtained. This information is crucial for understanding the role of texture and its evolution during deformation [47, 48].

Modern OIM systems can trace their origin back to the early work on observation of high-angle Kikuchi patterns by Meibon, Rupp and Boersch in the 1930s [49, 50]. Since then, it has gradually evolved through improved instrumentation into the current highly sophisticated and highly automated systems. Fig. 1.5 is a brief summary of the milestones in its development.

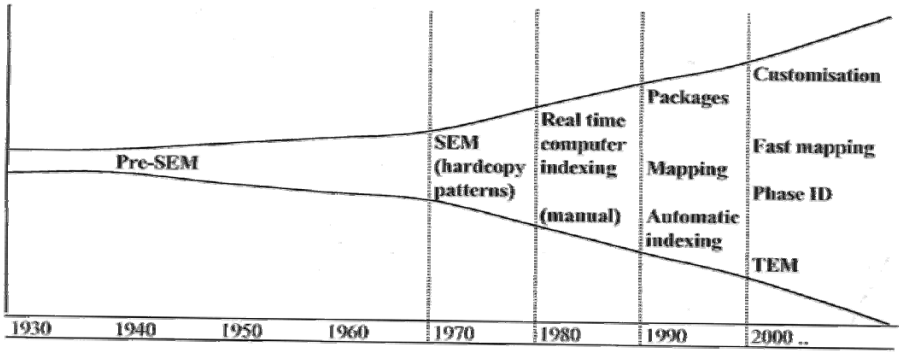

Fig. 1.5 Timeline summarizing the landmarks in EBSD development [51]

Present day OIM systems usually come as optional hardware and software modules attached to the scanning electron microscope. Fig. 1.6 illustrates its common set up. Aside from the SEM hardware, it includes a phosphor detector, a digital CCD camera imaging system, and a computer control and analysis system linked to CCD to process the captured EBSD signals. During the experiment, the sample is tilted relative to the incident beam to increase the yield of back-scattered electrons coming out of the sample surface. However, the tilting of sample has mixed effects. On the one hand, a larger tilting angle leads to a stronger

back-scattered signal and thus a better signal to noise ratio. On the other hand, the distortion in SEM imaging also increases with the amount of tilting. Such distortion will lead to inaccuracy of beam raster and varying beam-specimen interaction volume throughout the experiment. As a compromised solution, 70˚ tilt is considered ideal for most application.

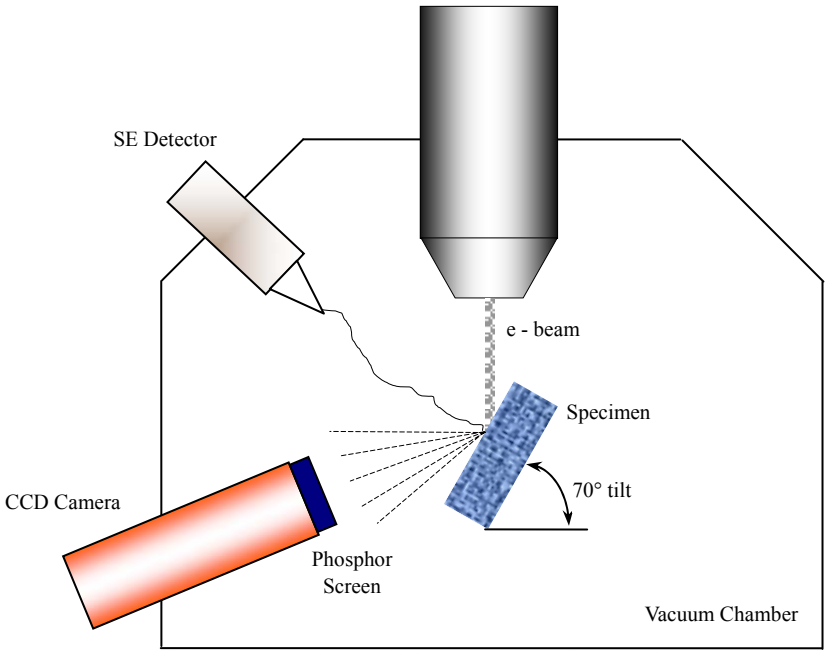

Fig. 1.6 Schematic for OIM experimental setup. Reproduced from B. S. El-Dasher [52].

The information obtained from OIM experiments, or EBSD patterns (namely Kikuchi patterns, Fig. 1.7 & Fig. 1.8) carry with them plentiful crystallographic information for the microstructure being investigated. Each band within the Kikuchi patterns represents a set of crystallographic planes upon which the diffraction of electrons satisfies the Bragg condition, as shown in Fig. 1.9:

$$n\lambda = 2d \sin \theta_B \qquad (1.18)$$

where λ is the wave length of the incident electrons, d is the spacing between crystallographic planes and θ_B is the Bragg angle. Since diffraction by crystallographic planes occurs in three dimensional space, the electrons Bragg

diffracted by a set of planes will form two cones, the intersection of which upon the detecting screen yields the band one can observe during experiments, as shown in Fig. 1.10. By analyzing the width of bands and their relative position with respect to each other in the Kikuchi patterns, one can back calculate to find the corresponding crystal structure and orientations that generate them. Today, this process has become part of the highly automated computer software.

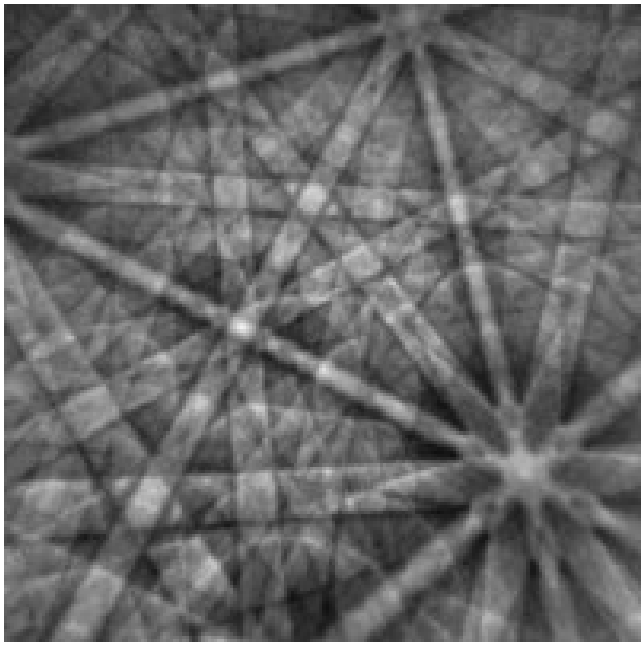

Fig. 1.7 Example of Kikuchi pattern observed in OIM experiments.

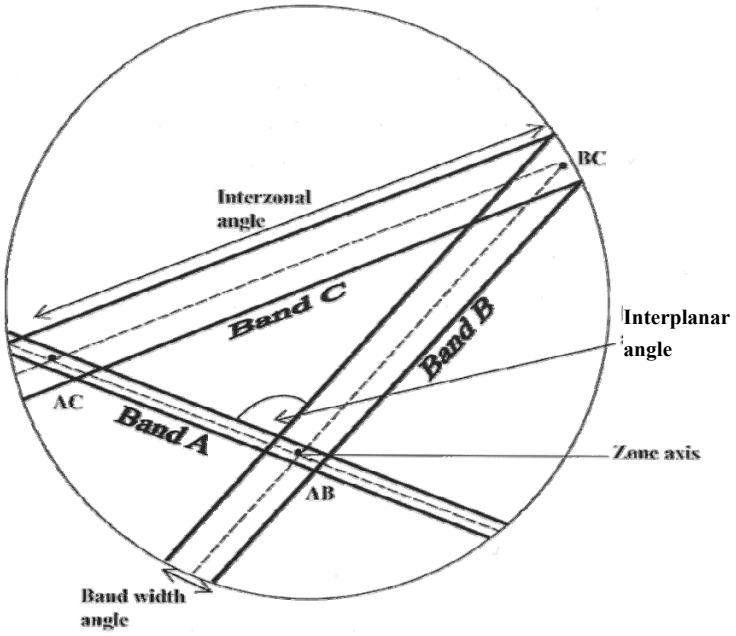

Fig. 1.8 The geometry of Kikuchi patterns carries with it rich information of crystallographic structure [51].

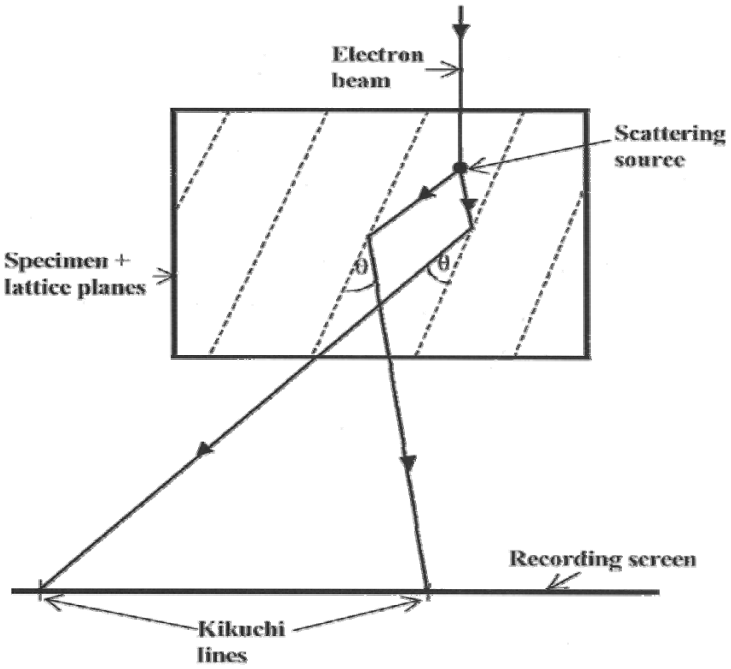

Fig. 1.9 2D schematic illustration of the formation of Kikuchi lines via diffraction of electrons by lattice planes (dashed lines), for the case of electron transmitted through the specimen [51].

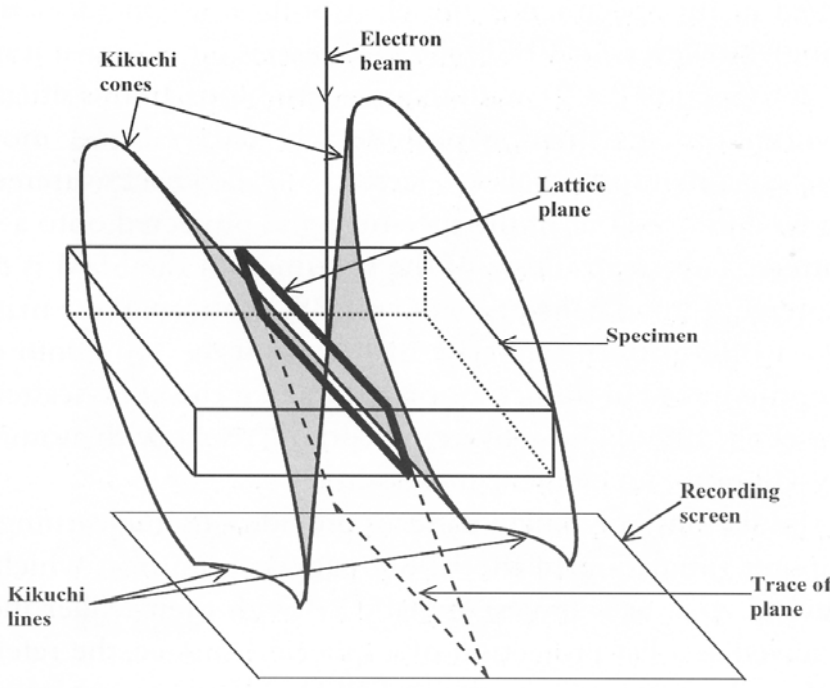

Fig. 1.10 3D representation of the formation of Kikuchi lines via diffraction of electrons by lattice planes (dashed lines), for the case of electron transmitted through the specimen [51].

The ability to survey a large surface area with high precision in a single scan is limited by the beam aberrations due to excessive tilting. The further away the beam is deflected to reach the off center area, the more imprecise it is in terms of beam positioning. From a practical point of view, the maximum area included in one single scan should not exceed 500μm×500μm. Survey of larger areas can be achieved by multiple scans together with SEM stage movement. The final result can then be obtained by post-scan stitching of results of smaller areas [52].

1.5.3 Nanoindentation

Appearing in the early 20th century, indentation tests were first performed by Brinell to measure plastic properties of materials [53, 54]. Later in the 1970s, it was found that the elastic modulus could also be determined from the indentation load-displacement curve [55]. To date, indentation has become a convenient way to obtain information on local material properties such as elastic modulus and hardness.

While conventional indentation tests focus on the scale of millimeters when making an indent, nanoindentation goes orders of magnitude smaller in indentation size, usually on the order of micron. The magnitudes of the loads are small in nanoindentation and are typically in the micro Newton range, while conventional methods are typically in the Newton range. Moreover, unlike conventional indentation tests, where the area of contact is calculated from direct measurements of the dimensions of the residual impression left in the specimen surface upon the removal of load, the nanoindentation test measures the depth of penetration together with the known geometry of the indenter to provide an indirect measure of the area of contact at full load. The slope of the elastic unloading dP/dh curve, Fig. 1.11, allows the specimen modulus and hardness to be determined. The relation between depth of penetration and residual contact area differs with different shape of the indenter. And there exist different theories for calculating modulus and hardness for experiments using different shape of indenter.

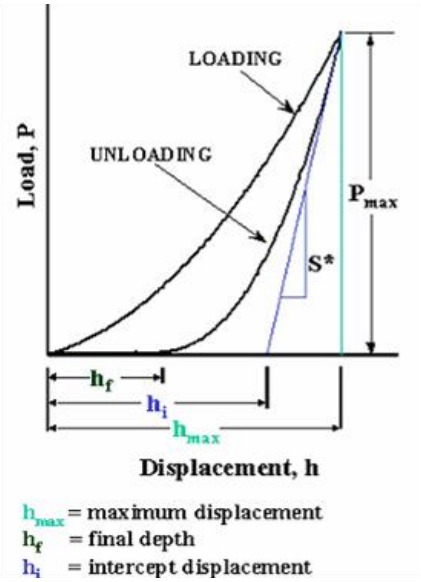

Fig. 1.11 Load-depth compliance curve of indentation experiment

The Nano-indenter® II operating at UM uses a standard diamond Berkovich tip as indenter. In this case, the expected relation between load and depth for an elastic-plastic contact is given by [23]:

$$h = \sqrt{P}[(3\sqrt{3}H\tan^2\varphi)^{-\frac{1}{2}} + [\frac{2(\pi-2)}{\pi}]\frac{\sqrt{H\pi}}{2\lambda E^*}] \qquad (10)$$

$$\frac{1}{E^*} = \frac{(1-\nu^2)}{E} + \frac{(1-\nu'^2)}{E'} \qquad (11)$$

where E^* is the "reduced modulus" or "combined modulus" of the indenter and the specimen, H is the hardness number, P is the indenter load, h is the total depth of penetration, φ is the semi-angle of the indenter tip, and λ is the geometry correction factor for the indenter tip.

In practice, several factors affect the accuracy of indentation results. These include the indentation size effect, the phenomenon of piling-up and sinking-in, initial penetration depth, drifting behavior, instrument compliance, and indenter geometry. A detailed discussion of the application of the technique can be found elsewhere [23, 56] .

1.5.4 FIB – Assisted TEM Dislocation Substructure Study

The focused ion beam (FIB) technique was mainly developed between late 1970s and early 1980s [57], and quickly applied to the semiconductor industry as a powerful tool for device modification, mask repair and failure analysis [58-60]. Recently, its application also extends into the micro fabrication of MEMS [61, 62].

FIB systems use a liquid metal ion source (LMIS), particularly gallium, as their source for operation. The LMIS is well known for its high intensity, compact structure and excellent reliability. During operation, the liquid metal forms a cone held by its own surface tension and nearby electric field at the source tip. Upon application of an extracting electrical field, a jet of fluid is emitted from the apex of the liquid metal cone and goes through a series of adjustment before it is finally used to perform the imaging, sputtering or deposition work [63].

In the imaging mode, shown in Fig. 1.12, the incoming gallium ions knock out secondary ions and electrons from the specimen surface, which are then collected by a biased detector to analyze the morphological information contained within them; In the milling mode, shown in Fig. 1.13, the incoming gallium ion flux increases significantly such that the major interaction between gallium ions and specimen becomes the physical sputtering of sample material. In the deposition mode, shown in Fig. 1.14, a gas precursor containing the target deposition material is released onto the specimen surface. Upon bombardment of gallium ions, the chemical bonds within gas molecules break and leave the target material deposited on the surface. Other volatile reaction products are extracted through the vacuum system. Nowadays, the commercial FIB systems can achieve resolution as high as 7nm in imaging, milling and deposition, as in the case of the FEI® Nova 200 Nanolab FIB system that now operates at UM.

The current research utilizes the versatile precision milling capability of FIB to section TEM foil from representative local microstructure for dislocation substructure analysis. Foils prepared using this method can be directly put under observation in TEM, circumventing all the grinding, dimpling and even sometimes

the ion milling procedure required by traditional preparation method. Details of the TEM foil preparation procedure by FIB will be addressed in a later section.

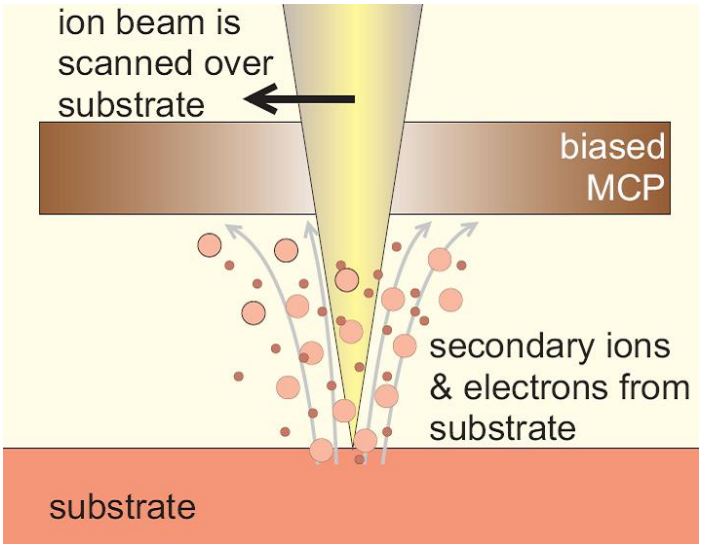

Fig. 1.12 Imaging mode of FIB, adapted from Reyntjens *et al.* [63]

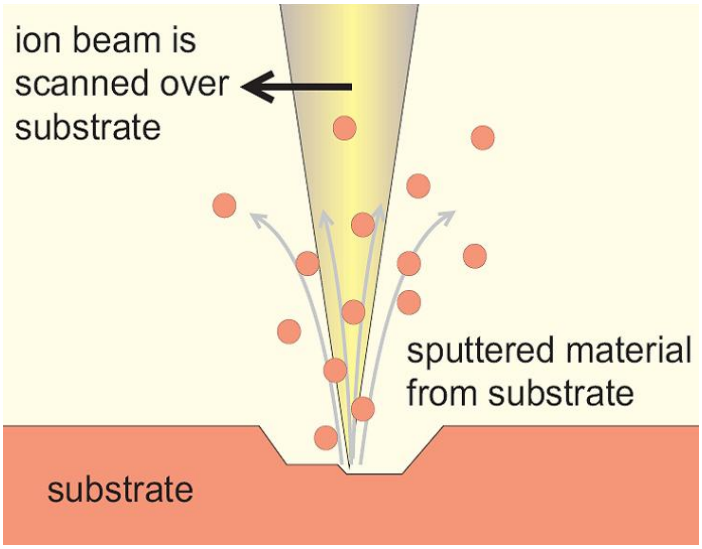

Fig. 1.13 Milling mode of FIB , adapted from Reyntjens *et al.* [63]

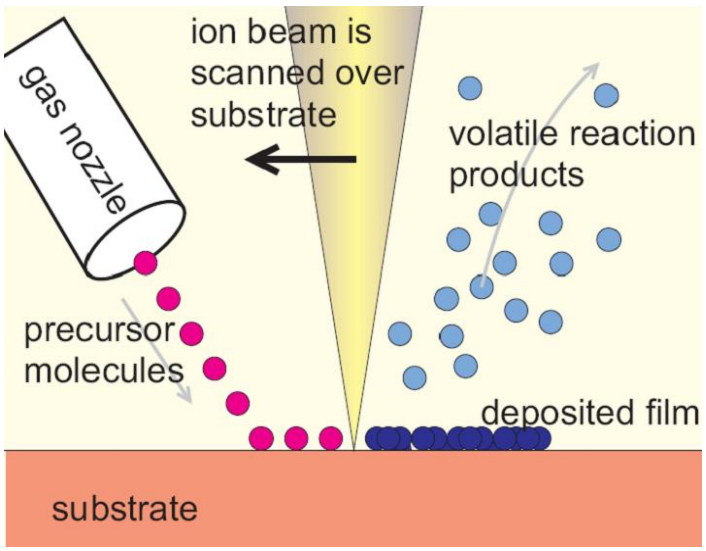

Fig. 1.14 Deposition mode of FIB, adapted from Reyntjens *et al.* [63]

CHAPTER 2

EXPERIMENTAL

2.1 Alloy Composition and Processing

Three different compositions of polycrystalline RuAl alloys were investigated. Compositions were selected with the aim of obtaining microstructures with varying amounts of the Ru-rich δ phase at grain boundaries. The nominal compositions of the alloys studied are: 48Ru52Al, 52Ru48Al and 48Ru50Al2Nb-0.5B.

The 48Ru52Al and 52Ru48Al alloys were fabricated at the University of Michigan. Charge materials consisted of 99.98% pure ruthenium sponge and 99.9% pure aluminum granules and melted into near spherically shaped buttons by levitation melting in a MCGS5 Crystalox system equipped with a copper cold crucible. Due to the very large difference in densities and vapor pressures between the two elements, some volatilization of Al during melting occurs (Al mass lost was calibrated at ~1 wt% for the system).Therefore excessive Al is added in the charge to compensate for loss of Al during fabrication. Melting is conducted by back filling the chamber with Argon to minimize the vaporization of Al. The 48Ru50Al2NB-0.5B alloy was melted into disk shaped buttons by electric arc melting carried out at Pittsburgh Materials Technology Inc., Pittsburgh, PA. All the alloys were then subjected to a homogenization heat treatment in an inert gas environment. The 48Ru52Al and 52Ru48Al were heat treated at 1350˚C for 36 hours; 48Ru50Al2b-0.5B was homogenized at 1500˚C for 24 hours

2.2 Compression Sample Fabrication

Samples for compression testing were sectioned from the melt buttons by electro discharge machining (EDM) to a final dimension of 5mm×5mm×10mm. The surface

selected for surface displacement mapping of each sample was mechanically polished down to 0.05μm Al_2O_3 finish before electropolishing in an electrolyte of 10% lactic acid, 7% sulfuric acid, 3% nitric acid, 2% hydrofluoric and methanol in the temperature range of -30~40˚C at 20~25 volts [64].

2.3 Surface Displacement Mapping

2.3.1 Marker Deposition

After polishing, markers were deposited on the as-polished surface by vacuum evaporation of Au through 2000 lines/inch commercially available nickel mesh grids. The nickel mesh was affixed to the polished sample surface by single-sided sticky tape. It was then wetted by ethanol and a cotton swab was used to press the mesh against the sample surface to ensure flat contact between the two. Following that, the sample was put inside a Centon Accum® vacuum evaporation system for gold deposition for about 12~15 seconds.

2.3.2 Compression Tests

Ex-situ surface displacement mapping tests were carried out by means of stepped loading, where the sample was imaged in the SEM between loading intervals. Compression tests were conducted at a strain rate of the order 10^{-4}/s by utilizing a compression fixture in an Instron model 5582 screw driven machine. The displacement between platens of the compression fixture was measured by a pair of linear variable capacitance transducers. Four steps of loading were each conducted for 48Ru52Al and 52Ru48Al and one step for 48Ru50Al2Nb-0.5B. The details of loading are listed in Table 2.1. Between each loading step, the specimen was taken for imaging in a Philips XL30 field emission gun SEM system. A specially designed stage was used to mount the specimen during imaging, as shown in Fig. 2.1. This stage serves to maintain the specimen orientation during imaging between different loading steps.

Table 2.1 Summary of Stepped Loading Tests

Alloy	Overall plastic strains accumulated within the specimen after each loading step (%)			
	Step 1	Step 2	Step 3	Step 3
48Ru52Al	1.50	2.07	3.14	3.65
52Ru48Al	1.12	1.78	2.99	3.96
48Ru50Al2Nb-0.5B	1.61	-	-	-

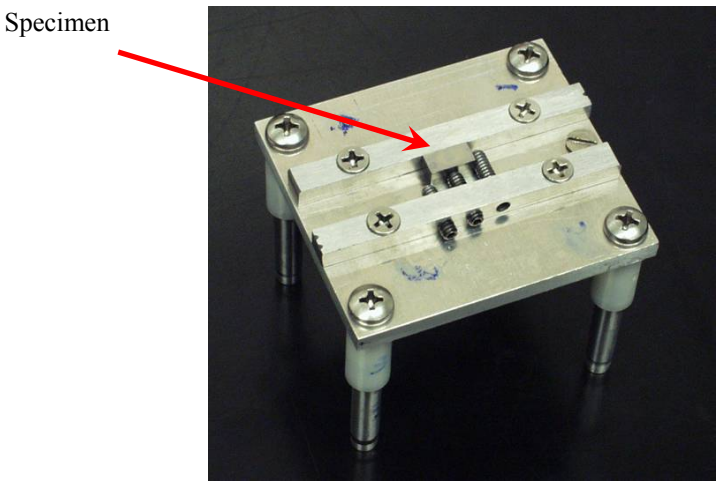

Fig. 2.1 Stage for holding compression sample in SEM

2.3.3 Strain Calculation

The before and after images from each set of test were input into a computer code written in the Interactive Data Language (IDL) by Biery and De Graef, which automatically calculated displacement and strain on a SUN Blade 1000 Unix workstation.

2.4 Orientation Imaging Microscopy Observation

OIM experiments were conducted for undeformed samples of 48Ru52Al and 52Ru48Al in a Philips XL30 field emission gun SEM equipped with TSL OIM® modulus. The scan step size was 3μm for 48Ru52Al and 5μm for 52Ru48Al, respectively. The resultant scan data were input into a Matlab program designed to calculate Schmid factors for each of the grains investigated. The program first converts the raw scan data containing crystallographic orientations of each grain into orientation vectors expressed in an external coordinate system which includes the loading direction as one of its three principal axes. Schmid factors are then calculated by taking dot products between direction of loading and directions of slip plane normals and individual slip directions. Details of the code can be found in Appendix I.

Another set of OIM experiments focusing on retrieving the lattice curvature information within the post-deformation microstructure were conducted on the 48Ru52Al alloy following its last step of loading test. The specimen was re-electropolished before orientation mapping. Two OIM experiments were conducted in a Philips XL40 field emission gun SEM equipped with TSL OIM® module in Carnegie Mellon University at Pittsburgh, PA, USA. One scan surveyed a large area using a step size of 1μm while the other used a 0.5μm step size to focus on a particular grain boundary region where significant strain gradients were detected during strain mapping. The acquired orientation data from the second scan were then input into a set of FORTRAN codes provided by El-Dasher *et al.* [52], which utilizes the linear simplex method to solve for the lower bound solution of the total GND density. Modifications to the code were made to tailor it to fit in the different slip systems and lattice parameter of B2 RuAl, i.e. to replace the <111>{110} slip system

in aluminum with <100>{110} & <110>{110} slip systems in RuAl, and to use 0.298nm as the lattice parameter.

2.5 Nanoindentation

Nanoindentation tests, conducted both for undeformed and deformed samples of two phase 52Ru48Al, were carried out in a Nano-indenter® II manufactured by Nano Instruments Inc. The applied indentation loading force was 12000μN (c.a. 1.2g). A standard diamond Berkovich tip was used as indenter. The RuAl intermetallic phase and δ phase were both investigated before and after sample deformation.

2.6 TEM Observation

Several representative grains that accumulated different amounts of strain after deformation of single phase 48Ru52Al were selected for dislocation substructure analysis by TEM. A series of TEM foils were prepared by FIB machining in a FEI Nova Nanolab dual beam system. A modified version of the standard "cross-section" and "lift-out" techniques [65, 66] as used for preparation of such foils. Using these foils dislocation substructure studies were carried out in a Philips CM-12 (LaB_6 source) transmission electron microscope with a double tilt holder. Seven to ten different diffraction vectors (**g**) from three different zone axes— <100>, <110> and <111>—were used to determine the Burgers vectors of the dislocations. Since the foil preparation is a critical part in the dislocation analysis, it deserves some additional description here.

2.6.1 Procedure for TEM Foil Preparation by FIB

TEM foil preparation by FIB can be conducted step by step manually or through specially written scripts such as AutoTEM by FEI®, which is capable of manipulating the system to automatically carry out a series of milling and polishing operations. However, the success of auto milling depends heavily upon the precision positioning of the ion beam during milling which, unfortunately, is often disturbed by the target specimen itself. The high sensitivity of the ion beam to the slight amount of charge pile-ups on the sample surface inevitably causes beam drifting during milling. For

RuAl, the drift can be as much as 1μm in the beam raster direction and one fifth of that in the orthogonal direction.

Given such challenges, manual operation is the only suitable way for the preparation of TEM foils from RuAl alloys in this research. Since the manual foil preparation usually involves multiple steps of delicate handling of specimen, it is thus worth some detailed description here.

Starting with the bulk sample, the manual preparation proceeds by:

1. Deposit 1μm thick Pt protective layer at region of interest through ion-assisted gas injection system (GIS).
2. Mill two staircase-shaped recessions on both sides of the future foil location with high ion current density (5nA or 7nA).
3. Mill the foil down to a thickness (1μm~2μm) appropriate for subsequent lift-off process with intermediary ion current densities (3nA & 1nA).
4. Weld fine tip plucker to one end of the foil by Pt deposition and lift the foil off by cutting it free from bulk.
5. Transport the as-cut foil to a semi-circular copper TEM grid with protruding platforms and weld the foil to one of the platforms by Pt deposition.
6. Mill the foil to near-finished thickness (~300nm) at low ion current density (0.1nA).
7. Polish foil in low voltage precision ion milling system (PIPS^{TM}) to further thin the foil to electron-transparent thickness (~100nm) and remove ion-induced surface damage.

The typical size of the foils fabricated using this method was about 15μm×5μm×0.1μm. It is necessary to point out that step 7 is important for TEM studies requiring the identification of Burgers vector of the dislocations, for it can remove most of the damage on the foil surface that was caused by the bombardment of high energy gallium ions. Typical working conditions for this step in a Gatan 691 Precision Ion Milling System (PIPS^{TM}) for a foil with initial thickness of about 300nm are: 4keV, 3rpm, 5° incident angle, 10μA beam current and 8~10 minutes polishing time at Dual Beam mode. The total preparation time for each individual foil by this

technique is in the range of 7~8 hours.

CHAPTER 3

RESULTS

3.1 Single Phase 48Ru52Al

3.1.1 Microstructure

Fig. 3.1 shows the initial microstructure of 48Ru52Al with markers deposited on surface. Grain boundaries were artificially highlighted for easy recognition. Grain sizes in the post heat-treated materials were typically in the range of 200~400μm.

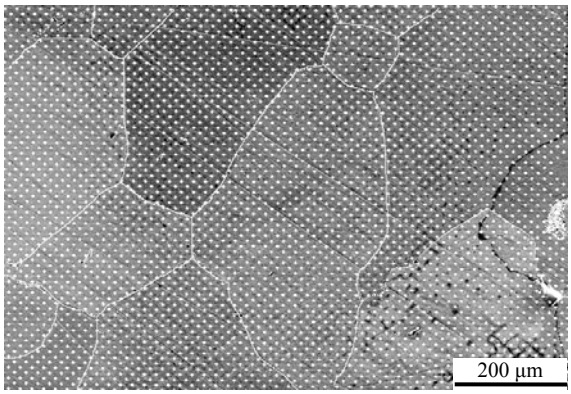

Fig. 3.1 SEM image of the microstructure of single phase 48Ru52Al alloy. Bright spots are gold markers deposited on the sample surface. Grain boundaries were highlighted for better viewing of their location.

3.1.2 Displacement and Strain Maps

Fig. 3.2 ~ Fig. 3.8 show the maps of displacement and strain components including: x–displacement maps, y–displacement maps, root mean square displacement maps, x–strain maps, y–strain maps, xy–strain maps (shear) and the Von

Mises effective strain maps after each of the 4 stepped loading compression tests of the same cluster of grains. In these maps, “x” denotes direction that was perpendicular to the external loading direction while “y” denotes direction that was parallel to the external loading direction. The root mean square displacement was calculated as the square root of the sum of the square of “x” displacement and “y” displacement. The reference point for all the displacement calculation was set at the center of the images. As a corollary, areas further away from the center typically display larger displacement in magnitude. This holds true for all the displacement maps.

All the maps were overlaid with the original microstructural image. For each of the displacement and strain components, the maps from 4 loading steps were plotted under the same linear color scale for easy comparison. Only the left portion of the maps were provided for step 2, 3 and 4 due to an intergranular crack initiated at the grain boundary on the upper right portion of the microstructure (marked in Fig. 3.2(b) & Fig. 3.8(a)) after step 1, leading to calculation failure thereabout. Several representative grains were selectively labeled as “A”, “B”, “C” and “D” in the strain maps for later reference.

In Fig. 3.2, the x–displacement maps, the initial horizontal displacement was relatively homogeneous across the entire cluster of grains after step 1 of 1.50% plastic strain, with outer regions particular the lower left and lower right displaying a slightly larger displacement than the central regions. It is not unusual given that all the calculation of displacement based its origin upon the center of the images. Therefore, the magnitude of the displacement calculated for markers further away from the center should be larger than those close to the center under ideally homogeneous deformation. This holds true for all difference components of the displacement maps, but not for any of the strain maps where the strains truly reflect the magnitude of local deformation around the microstructure regions. At higher loading levels, the x-displacement maps became more inhomogeneous in the lower portion while the upper portion remains fairly uniform with the average displacement increased in magnitude.

In Fig. 3.3, the y–displacement maps, just as in the x-displacement maps the degree of displacement heterogeneity increased with increasing loading level. There was an appreciable difference between the magnitudes of maximum and minimum of y displacement (14.22μm V.S. -9.09μm).

In Fig. 3.4, the root mean square displacement maps, the contours were far from being symmetric which would otherwise be expected in a perfectly homogeneous deformation scenario. This is obviously due to the influence of local microstructure.

In Fig. 3.5, the x–strain maps, strain fluctuation can be seen across the entire local microstructure after step 1, with patches of relatively low and high strain regions coexisted. Neighboring grains displayed different degrees of straining, with grain "A" accumulated slightly higher strains than the rest of the grains and grain "C" accumulated the least amount of strains. Such strain concentration difference persisted and became more prominent in the subsequent loading stages. The highest strains first appeared around a grain boundary triple point apparently due to the excessive local geometry constraints. It then extended further into nearby regions, particularly along the grain boundary regions on the highly strained grain "A" side before finally settled into several isolated high strain regions within grain "A". It is interesting to see that as strains increased to higher levels, there were still some regions exhibiting compressive strains after step 4, though a very small amount, especially in the low strain grain "C".

In Fig. 3.6, the y–strain maps, the deformation of local microstructure was again inhomogeneous with grain "A" accumulating much higher strains (roughly 3X) than the rest of its neighbors after step 4. The highest strain also developed at the same grain boundary triple point and evolved mostly within grain "A", just as in the case of the x-strain maps. A slight amount of tensile strain was also observed within grain "C" as well as in some other grains. This is consistent with the observation of compressive strain in the same locations in the x-strain maps. The average of strains within y-strain maps after each step is: 1.31%, 2.23%, 3.52% and 3.93%, respectively. The slight deviation of the mapped strains from the nominal imposed strains is normal given that the former strains were measured from a highly localized and anisotropic region.

In Fig. 3.7, the xy-strain (shear) maps, the strain heterogeneity pattern was

different from those displayed in x-strain and y-strain maps. There were both positive and negative shear strains across the entire local microstructural region and the magnitude of their maxima and minima was approximately equal to each other. The highest strains appeared in several different locations and no longer favored only the grain boundary triple points. Appearance of both negative and positive shear strains in grain "A" after step 4 indicated a more complex shape change in it. Meanwhile, grain "C" still had the lowest amount of straining among its neighbors.

In Fig. 3.8, the Von Mises effective strain maps, examination reveals significant strain heterogeneity developing early in the straining process, with a strong local microstructural influence. Individual grains, for example grains "A", "B" and "C", accumulated different amounts of strain after each step of deformation. Grain "A" deformed to a greater degree compared to its neighboring grains, accumulating the highest strains at an early stage of deformation, and continuing to be the most heavily deformed grain throughout the tests. Grain "B" experienced a lower degree of straining compared to grain "A". The strains within grain "B" gradually built up as the overall imposed strain increased. At the end of step 4, it accumulated the second highest strains among the grains within the field of view. Grain "C" was the least favorably prone to deformation, with very low strain levels even after the majority of its neighboring grains underwent a rather large degree of deformation. The highest strains appeared at a grain boundary triple point during all four stages of deformation, apparently due to the geometric constraints which built up stress locally. As the nominal strain increased following each loading step, the highest strains gradually evolved into a narrow band of approximately 20μm wide along the grain boundary on the high-strain-grain (grain "A") side. Several other high strain regions were observed near grain boundaries within the same grain. A close comparison of the four effective strain maps in Fig. 3.8 indicates that the pattern of strain heterogeneity that developed at the very early stage of deformation persisted to the higher strain levels.

According to strain maps statistics, summarized in Table 3.1, the maximum strain found in the effective strain map within each step was approximately 3X of the average value of the entire map, while the minimum strain was almost an order of

magnitude lower than the average.

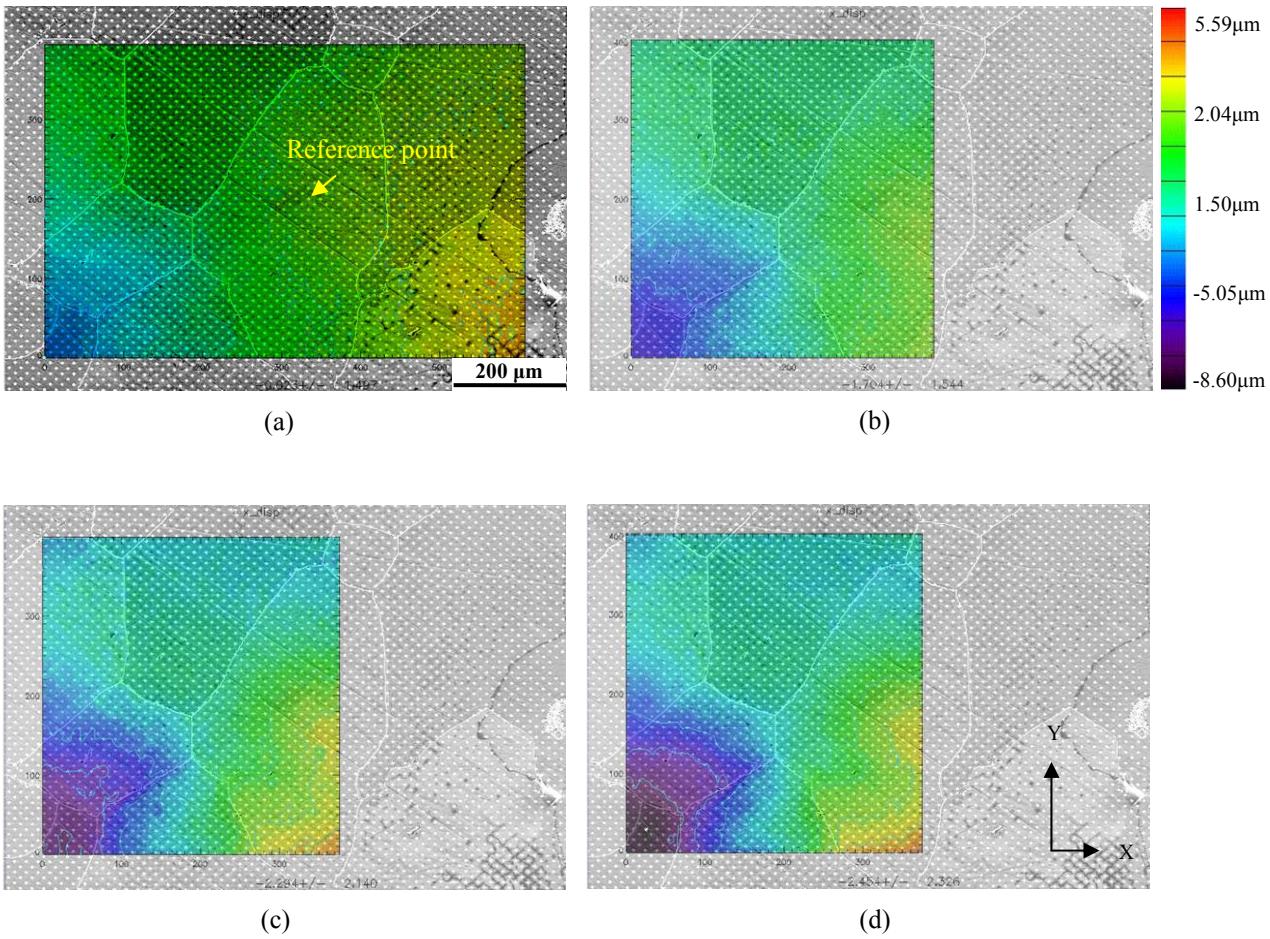

Fig. 3.2 X-displacement maps of single phase 48Ru52Al after (a) step i, 1.50% plastic strain; (b) step ii, 2.07% plastic strain; (c) step iii, 3.14% plastic strain and (d) step iv, 3.65% plastic strain.

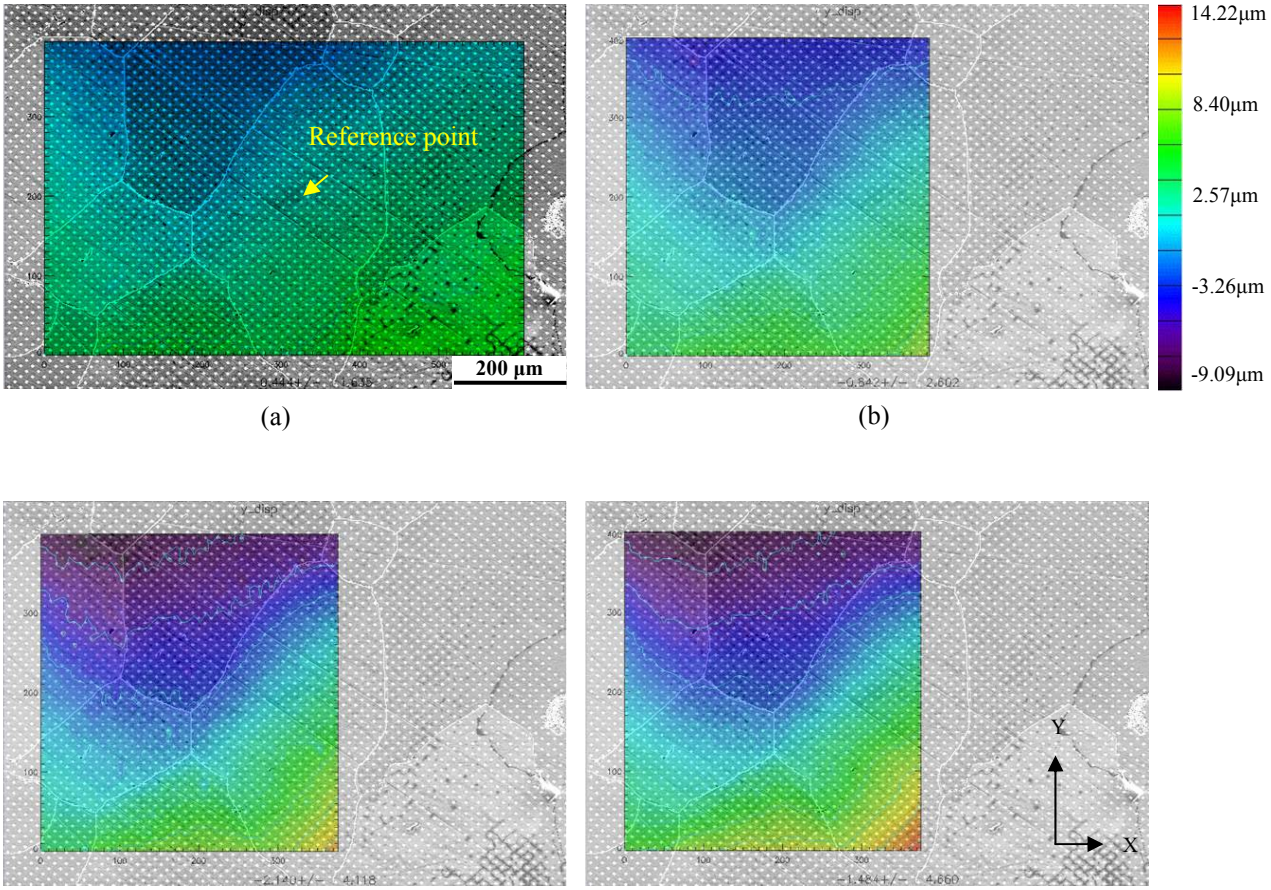

Fig. 3.3 Y-displacement maps of single phase 48Ru52Al after (a) step i, 1.50% plastic strain; (b) step ii, 2.07% plastic strain; (c) step iii, 3.14% plastic strain and (d) step iv, 3.65% plastic strain.

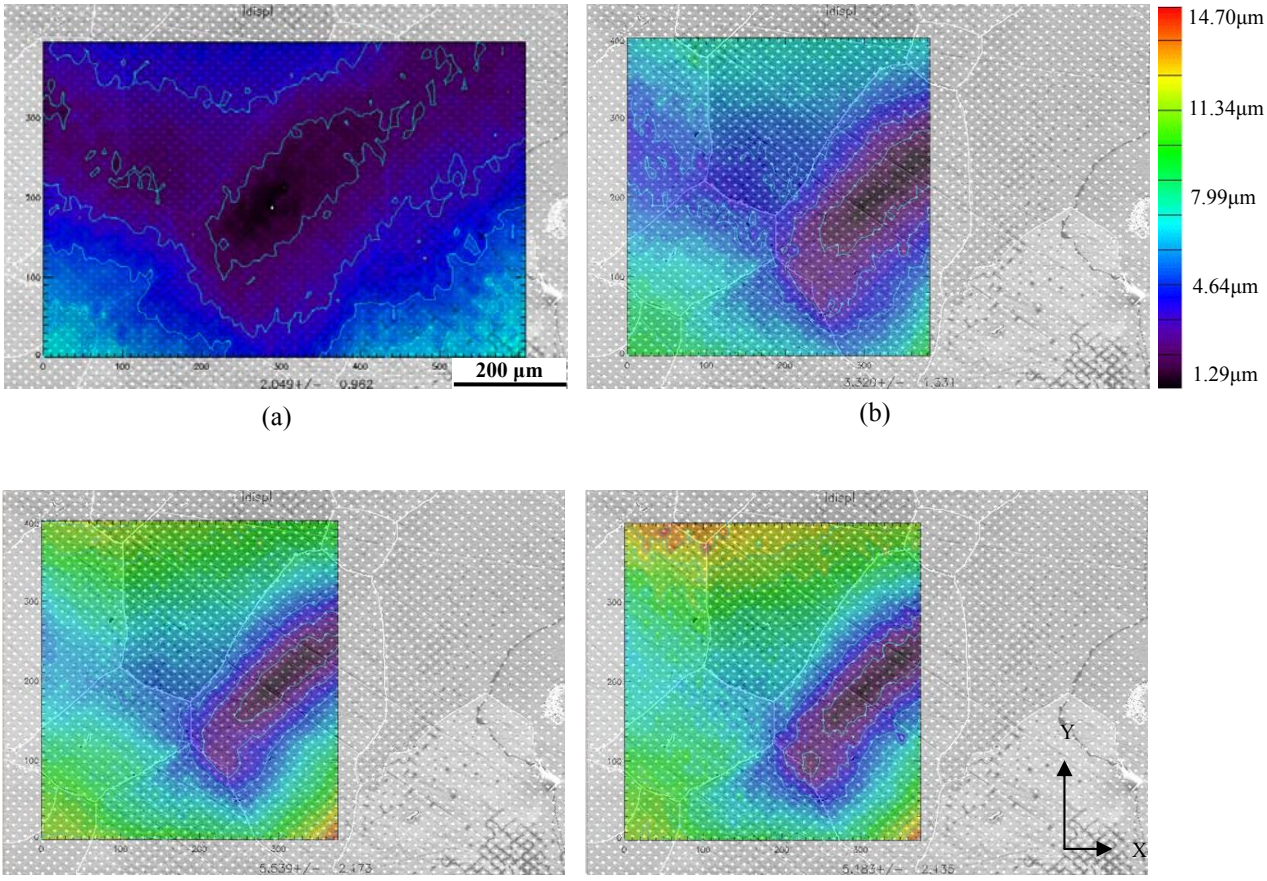

(a) (b)

(c) (d)

Fig. 3.4 Root mean square displacement maps of single phase 48Ru52Al after (a) step i, 1.50% plastic strain; (b) step ii, 2.07% plastic strain; (c) step iii, 3.14% plastic strain and (d) step iv, 3.65% plastic strain.

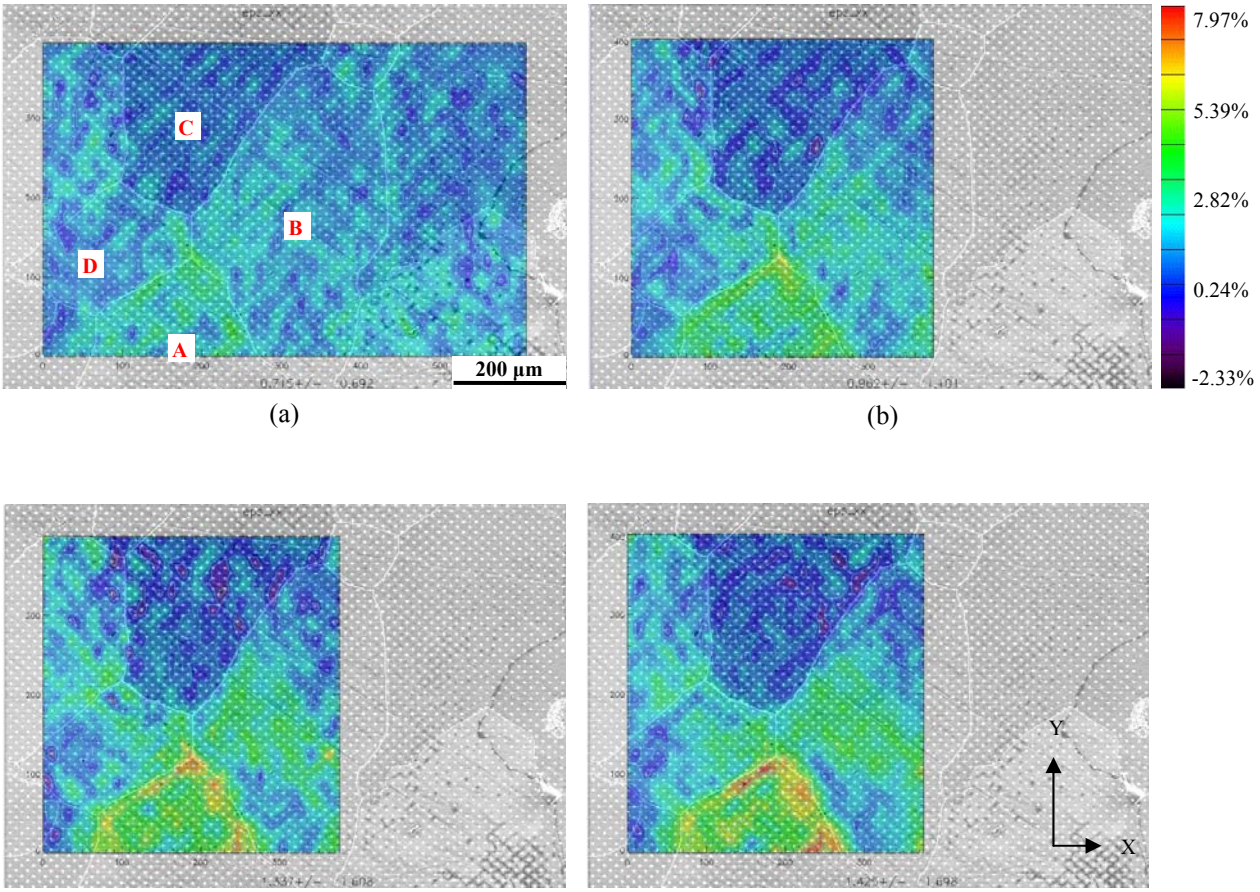

Fig. 3.5 X-strain maps of single phase 48Ru52Al after (a) step i, 1.50% plastic strain; (b) step ii, 2.07% plastic strain; (c) step iii, 3.14% plastic strain and (d) step iv, 3.65% plastic strain.

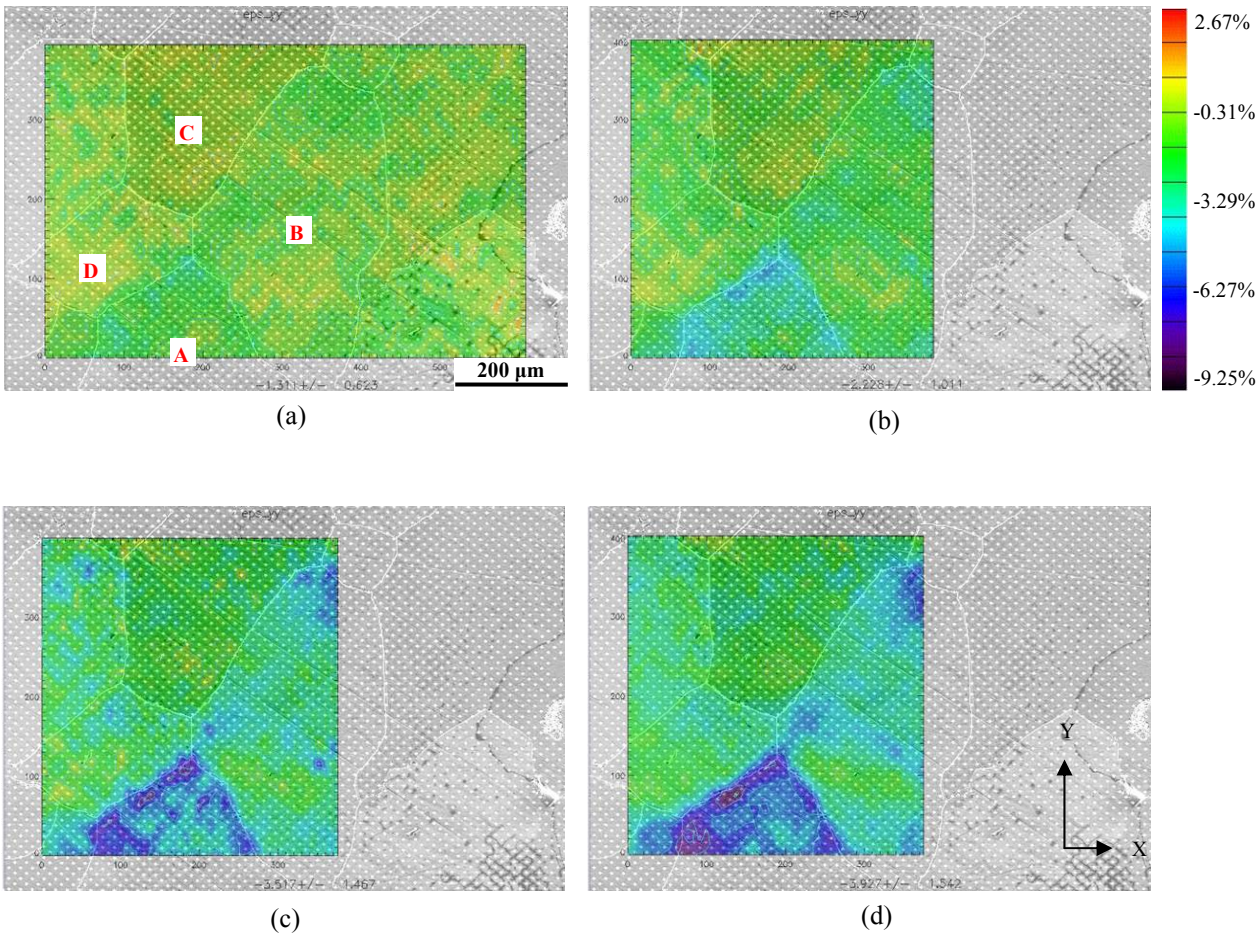

Fig. 3.6 Y-strain maps of single phase 48Ru52Al after (a) step i, 1.50% plastic strain; (b) step ii, 2.07% plastic strain; (c) step iii, 3.14% plastic strain and (d) step iv, 3.65% plastic strain.

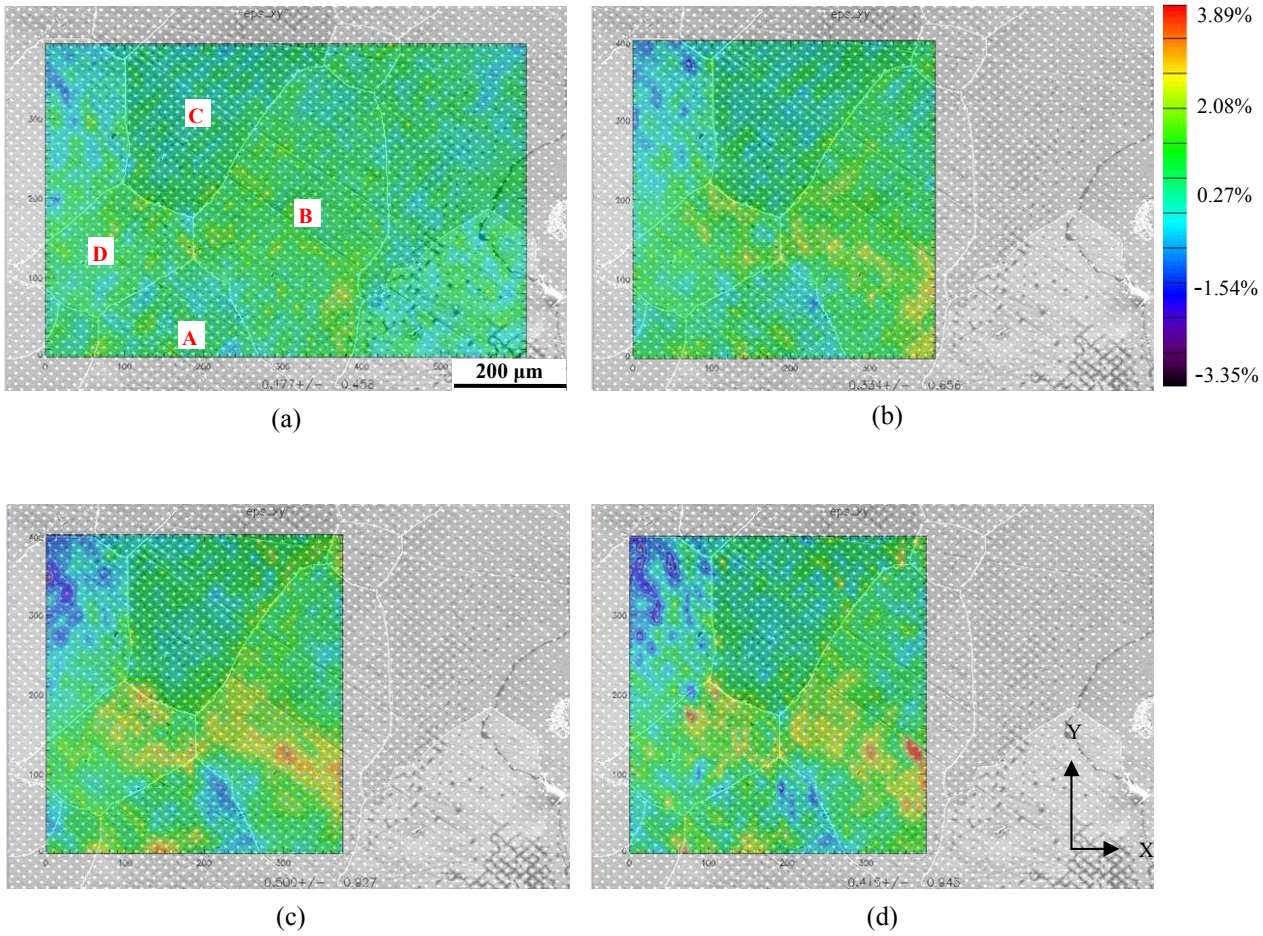

Fig. 3.7 XY-strain maps of single phase 48Ru52Al after (a) step i, 1.50% plastic strain; (b) step ii, 2.07% plastic strain; (c) step iii, 3.14% plastic strain and (d) step iv, 3.65% plastic strain.

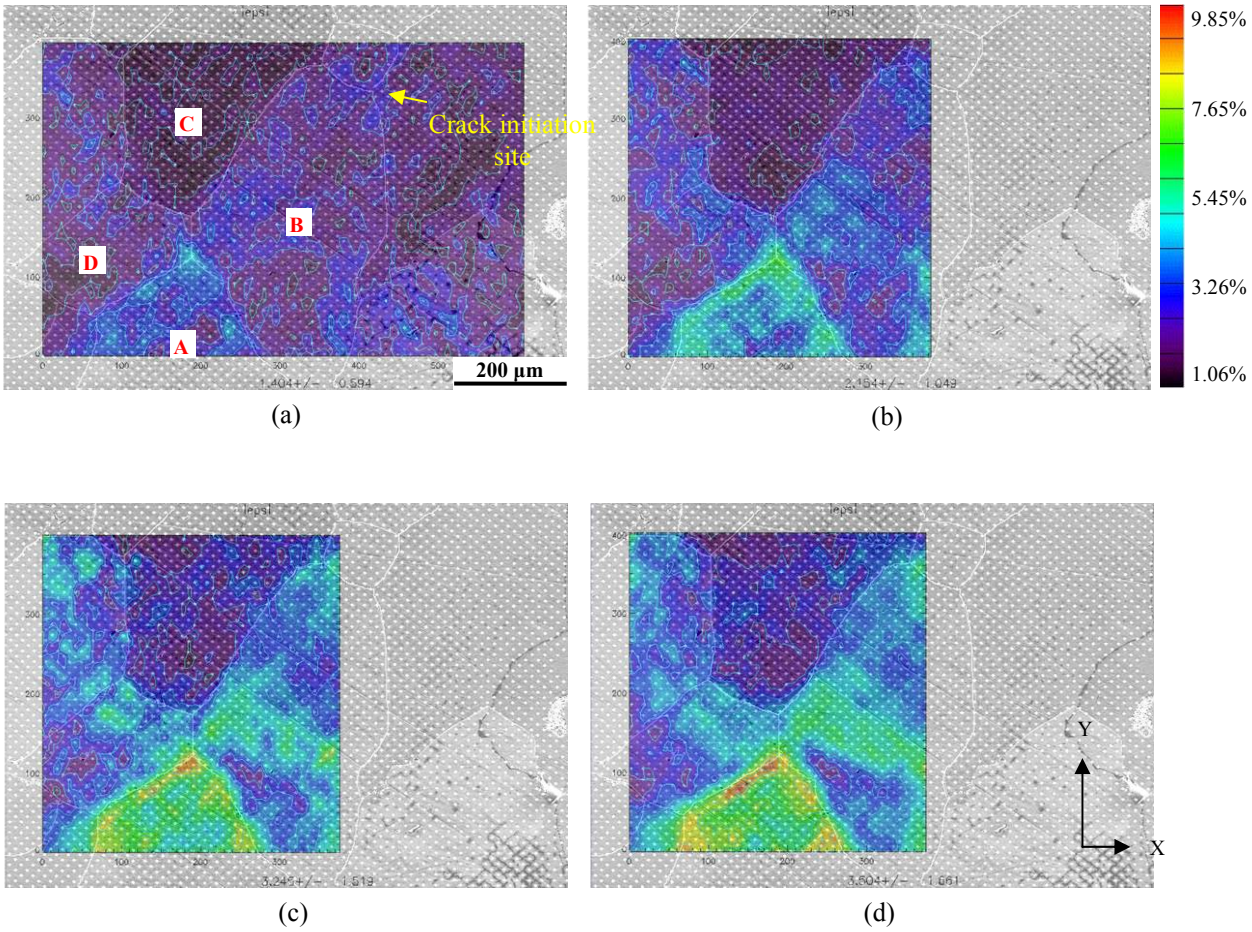

Fig. 3.8 Von Mises effective strain maps of single phase 48Ru52Al after (a) step i, 1.50% plastic strain; (b) step ii, 2.07% plastic strain; (c) step iii, 3.14% plastic strain and (d) step iv, 3.65% plastic strain.

Table 3.1 Statistics of effective strain maps of single phase 48Ru52Al alloy

	Nominal imposed strain	Avg. strain in the map	Std. dev. of Avg. strain	Max. in the map	Max. /Avg. strain ratio	Min. in the map	Min/Avg. strain ratio
Step 1	1.50%	1.40%	0.59%	4.49%	3.21	0.08%	0.06
Step 2	2.07%	2.15%	1.05%	6.45%	3.00	0.27%	0.13
Step 3	3.14%	3.25%	1.52%	9.47%	2.91	0.34%	0.10
Step 4	3.65%	3.50%	1.66%	9.85%	2.81	0.54%	0.15

3.1.3 Schmid Factor Calculation

Grain orientations within the cluster of grains being investigated here were acquired by EBSD analysis before sample deformation. Results are shown in Fig. 3.9(a). Note that the map only presents orientations that were along the out of plane direction. The in-plane orientations are not shown but were readily extracted from the EBSD scan data. With the input of point-wise orientation data and considering the loading direction (along "y"), it is possible to evaluate the contributions of individual slip systems during straining by calculating their respective Schmid factors among these grains. A Matlab program (see Appendix I) was used to conduct the calculation and the results are shown in Fig. 3.9(b) ~ Fig. 3.9(d). Note that all the Schmid factor plots were drawn under the same color scale (from 0.024~0.490). Fig. 3.9(b) is a composite Schmid factor plot, which adopted the maximum calculated Schmid factor between the two slip systems at each data point. Fig. 3.9(c) ~ Fig. 3.9 (d) are the Schmid factor plots for individual <100>{110} and <110>{110} slip systems.

Considering the composite Schmid plot in Fig. 3.9(b), there is only a minor variation in Schmid factor from grain to grain. For example, grain "A" has essentially the same Schmid factor as grain "C". This suggests that if both slip systems were equally favorably activated during deformation, there would be no preference for excessive straining between these two individual grains. However, this is not true, as was demonstrated by the effective strain maps showing significant differences in the strain concentrations within grain "A" and grain "C". On the other hand, Schmid plots for the individual slip systems show substantial differences in Schmid factor among neighboring grains. In the <100>{110} Schmid plot, Fig. 3.9(c), grain "A" has the smallest Schmid factor, followed by grain "B" with an intermediate Schmid factor and grain "C" with the largest among the three. In the <110>{110} Schmid plot, Fig. 3.9(d), exactly the opposite is observed. Comparing to the amount of strain developed within these grains, Fig. 3.8(d), there exists a close correlation between large <110>{110} Schmid factors and high strain concentration among these grains. This indicates that the <110>{110} slip system may be favored within the grains analyzed

in the experiments.

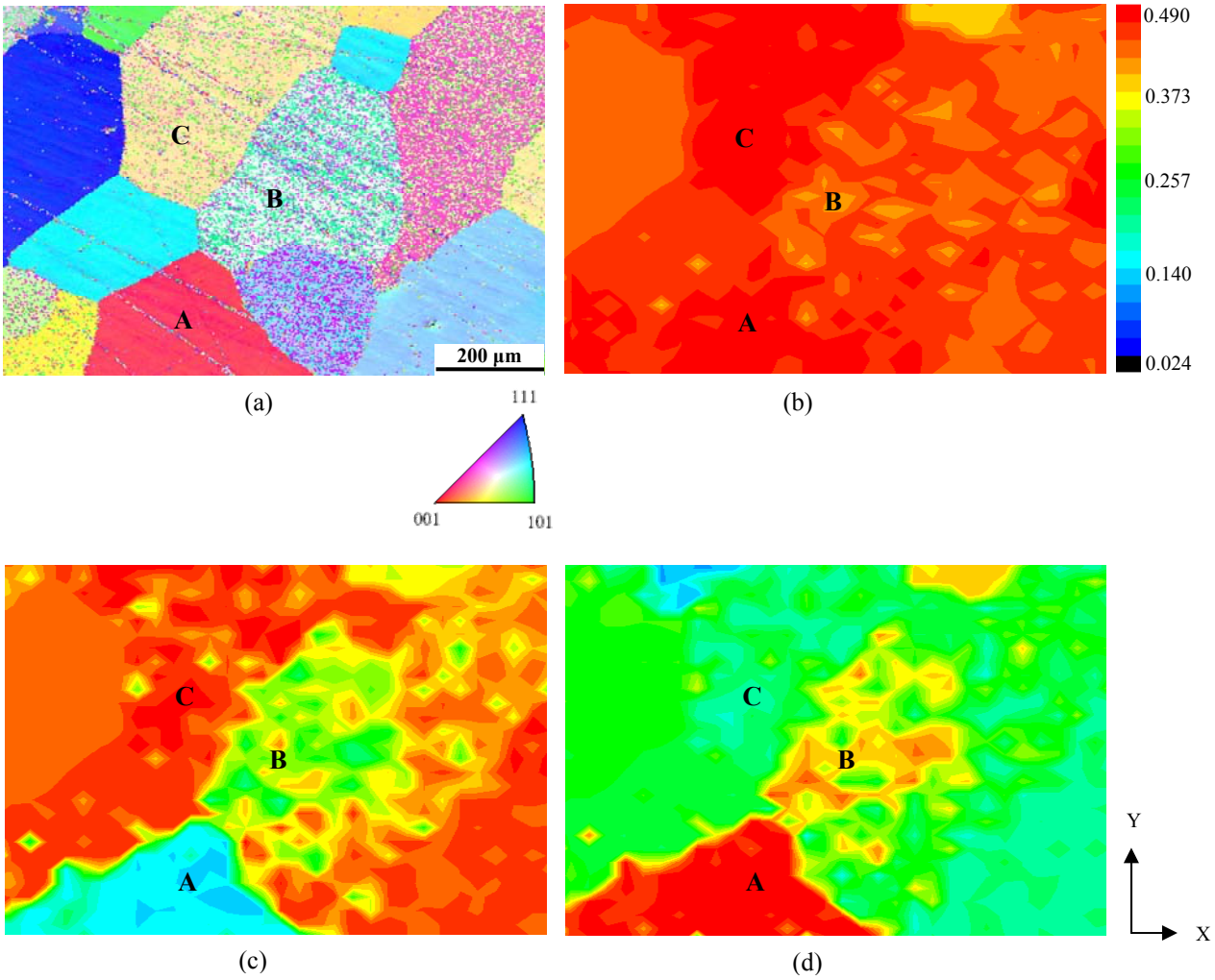

Fig. 3.9 (a) Grain orientation map of 48Ru52Al alloy before deformation, obtained by EBSD, (b) Composite Schmid factor plot for the maximum of <100>{110} or <110>{110}slip, (c) Schmid factor plot for <100>{110}slip system, (d) Schmid factor plot for <110>{110} slip system

3.1.4 FIB-assisted Dislocation Substructure Analysis

Based on the strain mapping and Schmid factor analysis results, a series of thin foils were fabricated from grain "A" and "C" by FIB for further dislocation substructure study in the TEM. The results are presented below.

Fig. 3.10(a) ~ Fig. 3.10(f) shows a series of dislocation bright field images taken under different diffraction conditions from the foil cut from the most heavily strained grain "A". Some randomly distributed dark spots can be seen in the background of the images. These are the result of surface foil damage by the impinging ion beam that was not completely removed during final polishing in PIPS.

The area shown is characterized by the presence of a high density of tangled dislocations. Such characteristic substructure was also observed in other regions of the foil. This is consistent with the high strain concentration in the grain. Dislocations near the center of the images have been identified as having Burgers vector of $[1\bar{1}0]$, given their invisible conditions at g=$[\bar{1}\bar{1}0]$ and g=$[\bar{1}\bar{1}1]$. Another set of <110> type dislocations were also identified near the lower left corner of the images. Significant density reduction at g=$[\bar{1}00]$ and g=$[0\bar{1}1]$ in this region as compared to g=$[\bar{1}01]$ suggest that the majority of the dislocations have a [011] Burgers vector. The presence of <100> type dislocations was less frequently observed. One example is a short segment near the middle left side of the images that was identified as having a [010] Burgers vector, given its invisibility conditions at g=$[\bar{1}00]$ and g=$[\bar{1}01]$. Clearly, the density of <110> type dislocations is significantly higher than that of <100> type. In addition, a small number of $[\bar{1}11]$ dislocations were also observed near the upper right side of the images with invisible conditions at g=$[\bar{1}\bar{1}0]$ and g=$[0\bar{1}1]$.

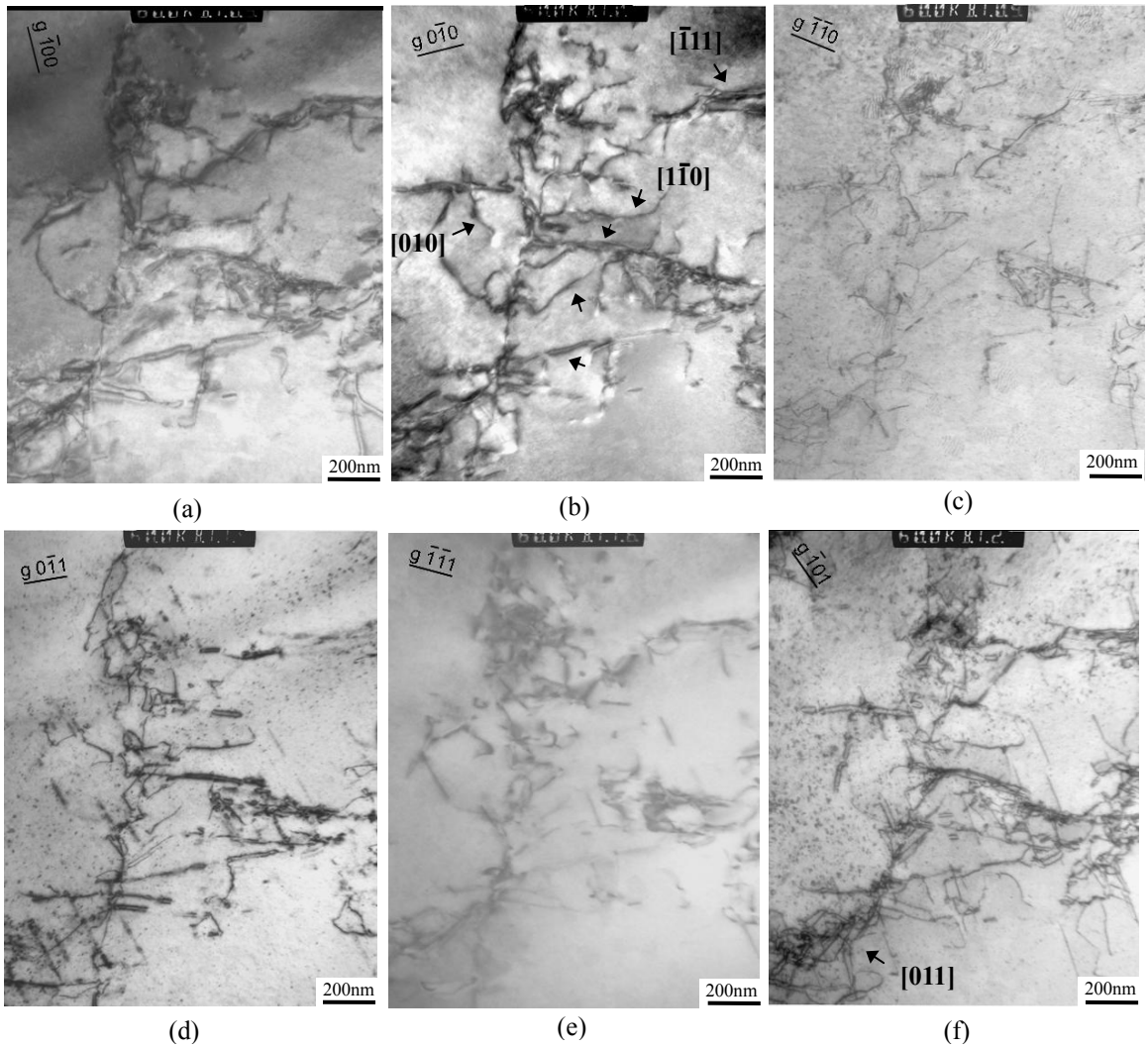

Fig. 3.10 Bright field images of dislocation network observed in FIBed TEM foil from high strain grain "A". Dislocations of <110>, <100> and <111> type Burgers vector were found. The majority of dislocations were identified as having Burgers vector of <110> type.

Fig. 3.11(a) ~ Fig. 3.11(f) shows a series of dislocation bright field images taken under different diffraction conditions from the foil cut from the least strained grain "C". The dislocation density within the foil cut from this grain is indeed very low. The area shown in Fig. 3.11(a) ~ Fig. 3.11(f) represents one of the few regions within the foil that contained a significant density of dislocations. Dislocations within this region can be characterized by the presence of several long segments, a few dipole loops and aggregates of very short entangled segments. A majority of dislocations become invisible with g=[$1\bar{1}0$] and g=[$\bar{1}0\bar{1}$], indicating that their Burgers vectors are of [$11\bar{1}$] type. However, since <111> slip is not the major type of active slip identified in this material [7], and given the very low strain concentration within this grain, it is likely that these <111> type dislocations did not result from dislocation motion but rather remain as a result of the high temperature processing of the original material. The presence of <111> dislocations following processing of this compound has also been previously observed [67].

A comparative dislocation substructure study using materials from the same processing batch (i.e. identical processing conditions) prior to deformation was conducted in order to determine the initial dislocation content. A TEM foil was prepared using the same FIB-assisted fabrication method. Fig. 3.12(a) ~ Fig. 3.12(f) shows a series of dislocation bright field images taken under different diffraction conditions from the foil cut randomly from another sample of 48Ru52Al before deformation. A survey over the entire foil suggested that the dislocation density was low and comparable to that found in low strain grain "C". Using invisibility conditions, two segments of dislocations were identified as having Burgers' vector of [111] type, due to invisible conditions at g=[$0\bar{1}1$] and g=[$1\bar{1}0$]. This confirms that the existence of <111> dislocations is common among this batch of 48Ru52Al alloys following heat treatment before deformation. Although the amount of <111> dislocations detected in this case is somewhat less than those observed in grain "C", this is not unexpected given the typical grain to grain variation in dislocation density.

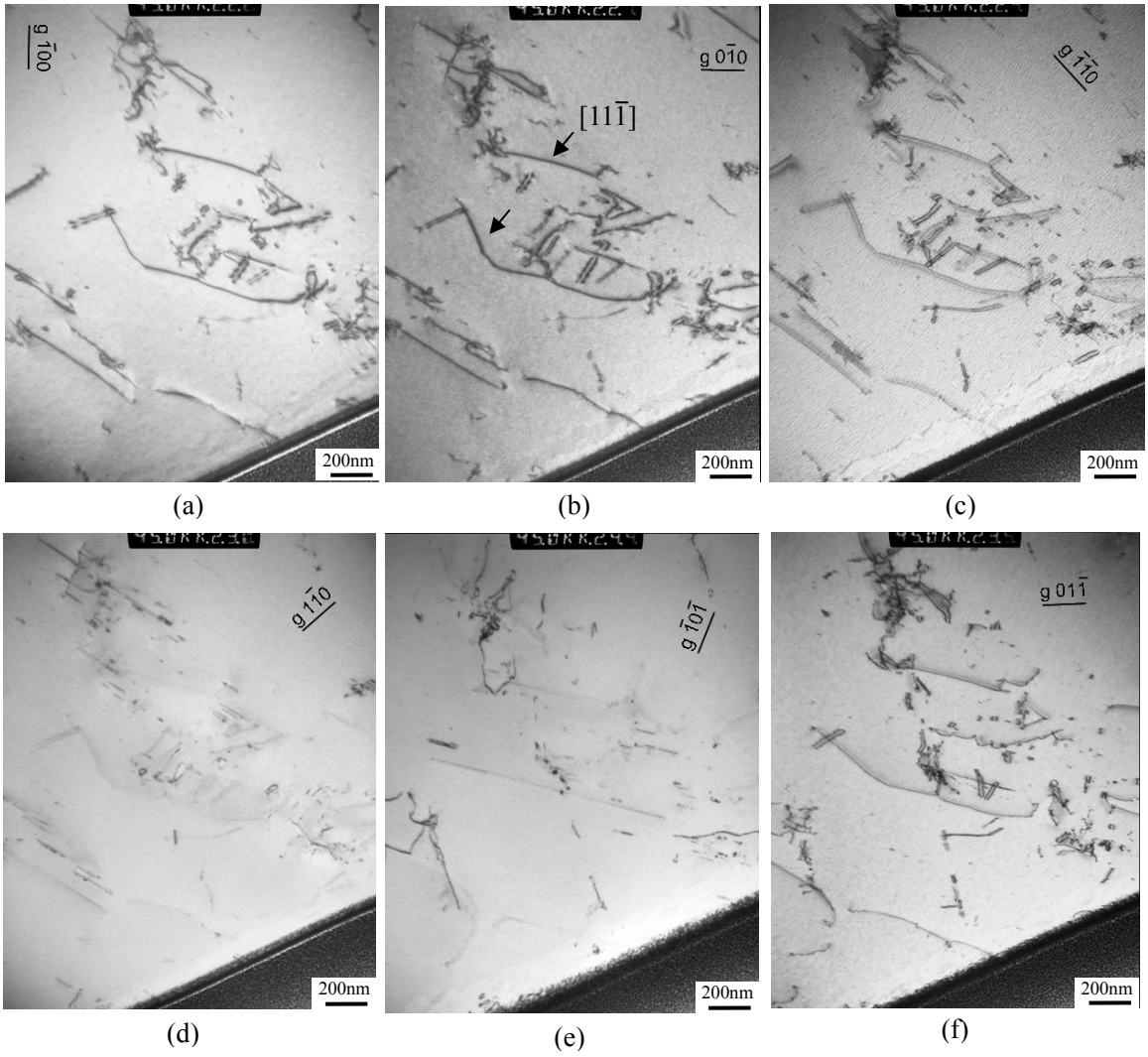

Fig. 3.11 Bright field images of dislocations observed in FIBed TEM foil from low strain grain "C". A majority of dislocations were identified as having <111> type Burgers vector. They are likely remnants left by the processing of the original material.

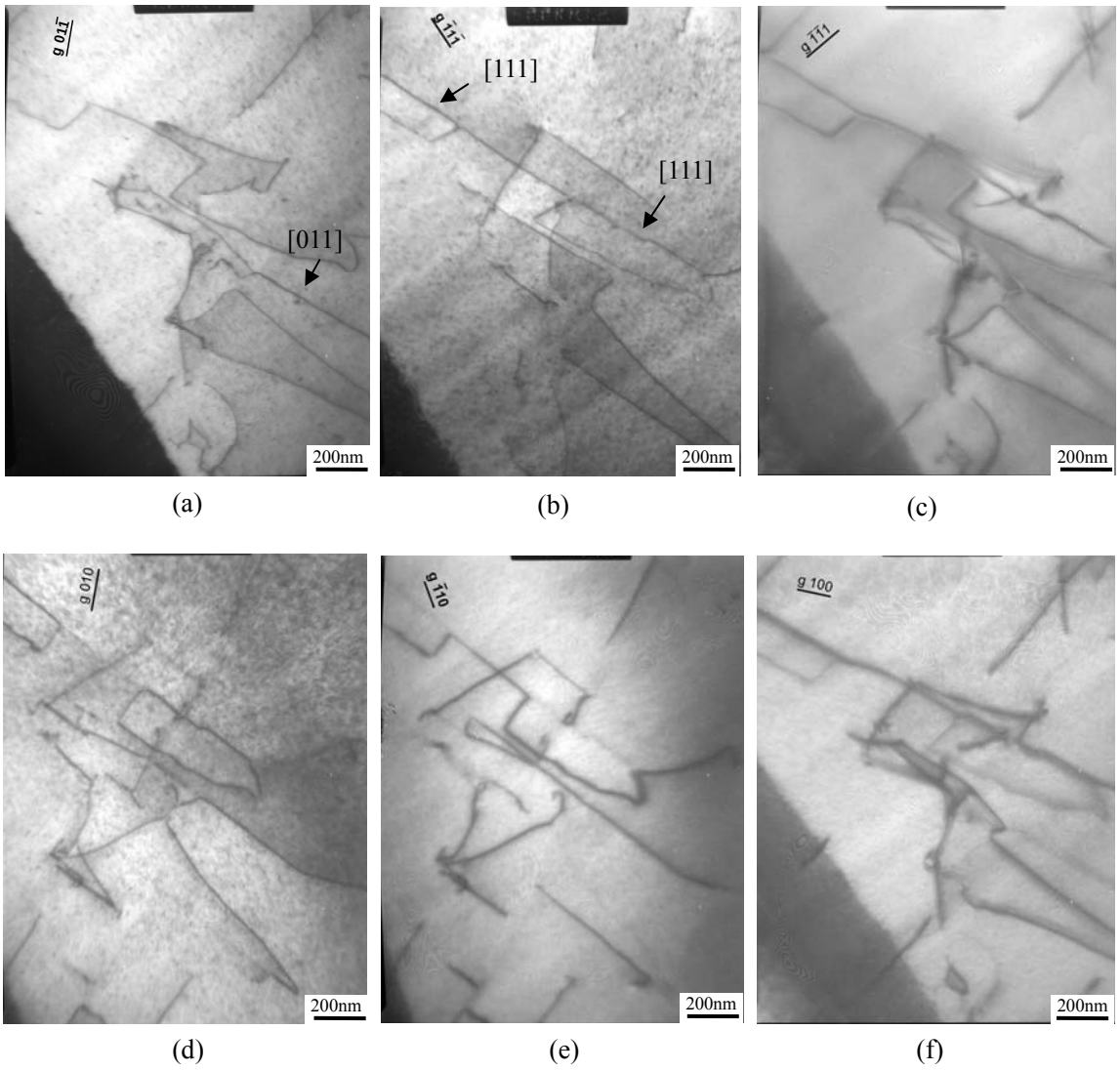

Fig. 3.12 Bright field images of dislocations observed in FIBed TEM foil from 48Ru52Al prior to deformation. Dislocations of [111] type Burgers' vector were identified.

3.1.5 Measurement of Geometrically Necessary Dislocation Densities

Fig. 3.13(a) ~ Fig. 3.13 (b) shows the microstructure and Von Mises effective strain map of 48Ru52Al after 3.65% nominal compression, respectively. The areas for the two OIM scans are marked in Fig. 3.13(a) and the corresponding orientation maps are shown in Fig. 3.13(c) ~ Fig. 3.13(d). The calculated GND results along three particular locations across the boundary from grain "D" to grain "A", marked as line 1, 2 and 3 in Fig. 3.13(d), were selected and plotted against the effective strain

distribution profile extracted from the same location in the strain map. Results are shown in Fig. 3.14(a) ~ Fig. 3.14(c). In addition, a three point box average operation has been applied to smooth the calculated GND data. Note that the scales for strain are identical among the three plots, so thus the scales for total GND density. The grain boundary is outlined with a dotted line in each plot to indicate its location.

Considering the strain distribution profile, there are large gradients in total effective strain across the grain boundary. Further from the boundary, strains plateau and remain fairly constant in grain interiors. When approaching the boundary to within a distance of about 20μm, the strain on both sides sharply increases and finally reaches a peak value, in this case on the grain "A" side adjacent to the boundary. The largest gradients exist mostly within a distance of about 20μm where the transition from peak strain to trough strain occurred across the boundary. The magnitude of reduction within this 20μm distance is between 5%~7%, resulting in corresponding strain gradients of about 0.25~0.35%/μm.

While strains varied to the highest degree in areas that are close to the boundary in both grains, the total dislocation density did not exhibit similar trends. The overall magnitude of total GND density in grain "D" is approximately between $1\times10^{13}\sim 2\times10^{13}m^{-2}$, as measured by the OIM technique. The GND density in grain A varies between $1\times10^{13}\sim 4\times10^{13}m^{-2}$. In addition, a slightly larger variation of total GND density in grain "A" is also observed. There is a trend that higher strain accumulation within individual grains leads to larger total GND density as well as higher degrees of fluctuation in its magnitude. What is also apparent is that within the same grain, the near grain boundary high strain areas have very similar total GND density compared to the inner grain low strain areas. To summarize, for the limited number of grains examined here by the OIM technique, the total GND density remains essentially the same within individual grains regardless of the gradients observed by the strain mapping technique. In fact, similar strain gradients existing in different grains (for example the slope on both sides of the peak in Fig. 3.14(a)) leads to a different magnitude of total GND density. It seems that total GND density is only a function of total strain within each grain and insensitive to the gradient variation within it. This

may, in turn, suggest that incompatibilities due to differential deformation from grain to grain are accommodated over the volume of the grain rather than being localized at grain boundaries.

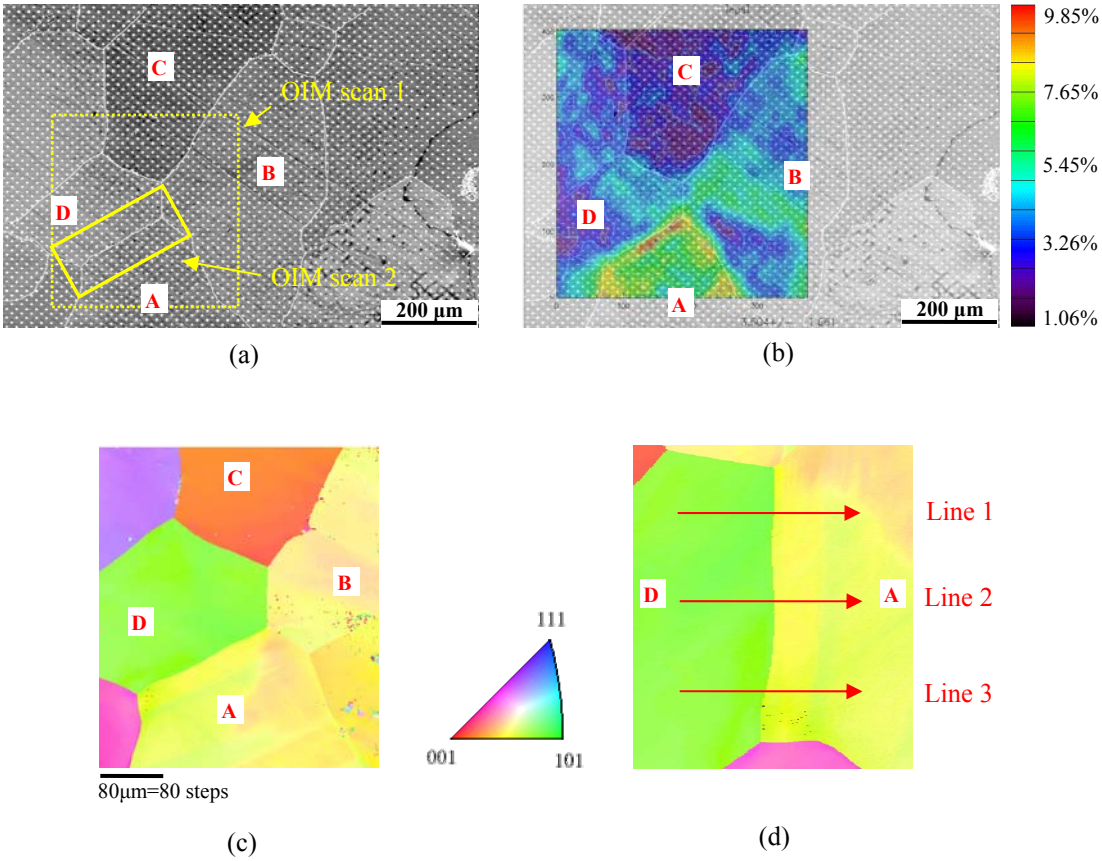

Fig. 3.13 (a) Microstructure of 48Ru52Al with gold markers deposited on the surface, grain boundaries are artificially highlighted for easy recognition; (b) Effective strain maps after 3.65% nominal plastic compression; (c) Orientation map of 48Ru52Al after 3.65% deformation, focused on the entire strain mapped areas with scan step of 1µm; (d) Orientation map of 48Ru52Al after 3.65% deformation, focused on one particular grain boundary with finer scan step of 0.5µm.

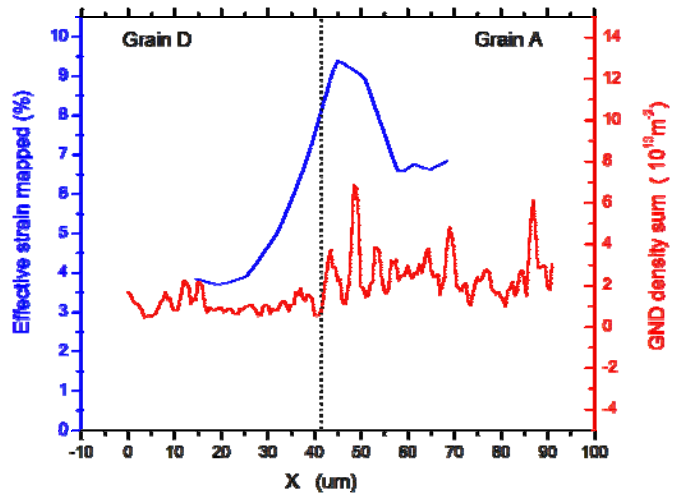

(a)

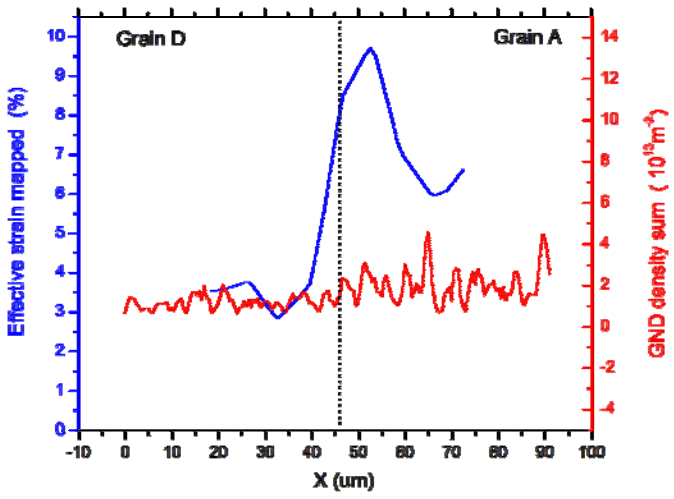

(b)

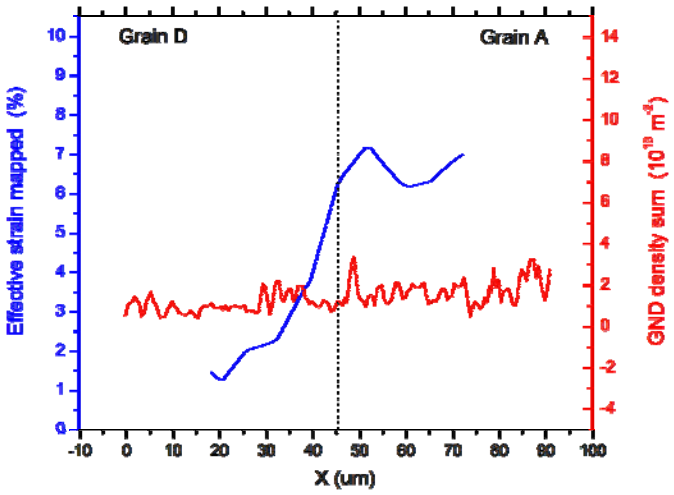

(c)

Fig. 3.14 Effective strain mapped v.s. total GND density along (a) line 1, (b) line 2, and (c) line 3. The dotted line in each plot marks the location of grain boundary

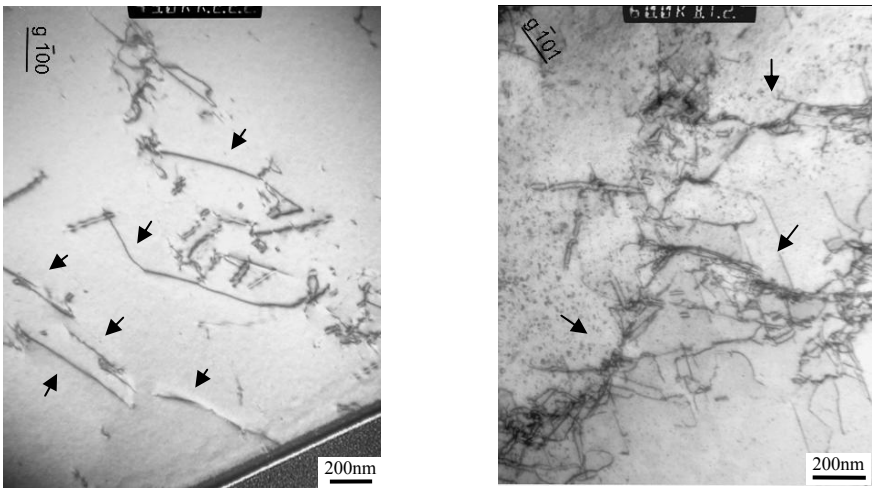

(a) (b)

Fig. 3.15 TEM micrographs of (a) low strain grain "C", and (b) high strain grain "A"

To better understand the role of GNDs, the total density of dislocations stored in the material before and after deformation is estimated by measuring the total projected length of the dislocations within the field of view using TEM micrographs taken from grain “A” and “C”, and divided that by the total volume of the area of interest [68]. Since the strain accumulation in grain “C” is very low, the dislocations within it can be regarded as residual dislocations from processing. The unique FIB-based foil preparation procedures permit a fairly precise measurement of their thickness, which is approximately 120nm in this case. This results in a sample volume of approximately $4.7\times10^{-19}m^3$ for the area imaged under g[$\bar{1}$00] in Fig. 3.15(a) (length = 2.22×10^{-6}m, width = 1.78×10^{-6}m). Assuming all dislocations observed were of either <100>, <110> or <111> type Burgers vectors, under this diffraction vector, two thirds of the <100> dislocations (i.e. [010] & [001]) and one third of <110> dislocations (i.e. [011] & [0$\bar{1}$1]) will be invisible. Most of these invisible dislocations would appear under g[1$\bar{1}$0] in Fig. 3.11(d). However, since only a very small density of dislocations is visible under g[1$\bar{1}$0] according to Fig. 3.11(d), g[$\bar{1}$00] dislocations represent the majority of the population within that area. The total projected length of

the 6 long segments of dislocations (marked by arrows in Fig. 3.15(a)) can be easily measured, which gives approximately 4200nm. The total length of the remaining short entangled dislocations, however, is difficult to calculate accurately. The best attempt to measure their individual length yields a total number of 8400nm, with the error estimated to be no more than 50% below the true value. Therefore the total projected length of dislocation within Fig. 3.15(a) is approximately 12600nm. Hence the dislocation density within the sample volume in Fig. 3.15(a) is roughly $2.7\times 10^{13}m^{-2}$. However, since the area imaged in Fig. 3.15(a) was one of the few high density areas, a number of random surveys of dislocation density covering other areas of the foil suggested that a factor of one tenth needs to be taken into account for estimating average dislocation density within the entire foil. This yields the final average dislocation density stored in grain "C" of approximately $2.7\times 10^{12}m^{-2}$. It is necessary to point out that the inevitable presence of errors in this measurement approach makes it possible to estimate the density of dislocation only within the range of an order of magnitude.

Similarly, the density of dislocation stored in grain "A" after deformation can be estimated. The sample volume shown in Fig. 3.15(b) is roughly $2.6\times 10^{-19}m^3$ (length = 1.66×10^{-6}m, width = 1.33×10^{-6}m). The best attempt to measure the individual length of the dislocations within the three bundles (marked by three arrows in Fig. 3.15(b)) yields the total length of approximately 26800nm. Among all the dislocations presented, i.e. <100>, <110> and <111>, only one third of the <100> dislocations (i.e. [010]) and one sixth of the <110> dislocations (i.e. [101]) were invisible under this g[$\bar{1}$01] diffraction vector. Given that the contribution of <100> dislocation to the overall line length is only trivial in this <110> slip dominating grain, the total projected length after taking into account invisible dislocations is approximately 32160nm. Therefore, the average dislocation density within the sample volume is approximately $1.2\times 10^{14}m^{-2}$. Surveys over other areas of the foil indicated the common presence of such high density areas, and the number $1.2\times 10^{14}m^{-2}$, therefore, can be regarded as the average total density in grain "A". Again, this is only a lower bound estimation given the difficulty of measuring individual dislocations from their

highly entangled state. However, the true value should well lie within this order of magnitude.

Compare these two estimated total density values of dislocations that were stored inside the material before and after deformation, i.e. $2.7\times10^{12}m^{-2}$ for before and $1.2\times10^{14}m^{-2}$ for after, to the measured GND density sum of $1\times10^{13}\sim 4\times10^{13}m^{-2}$ (take with a mean value of $2.5\times10^{13}m^{-2}$), it is apparent that the density of GND measured through OIM only constitutes approximately one fifth of the total density of dislocations (including GNDs and SSDs) that were stored inside the lattice after deformation. In another word, the ratio of SSDs to GNDs in the post deformation materials was approximately 4:1. However, considering that the estimation of dislocation density in post deformation materials only accounts for those "easily-observed" dislocations, the total density of stored dislocations should be higher in reality. Given that the density of GNDs is known through OIM measurement of lattice curvature, this means that the real ratio between SSDs and GNDs should be higher than 4:1.

3.2 Two Phase 52Ru48Al

3.2.1 Microstructure

Fig. 3.16 shows the microstructure of 52Ru48Al alloy. It is observed that the secondary Ru-rich δ phase, which appears as the brightly contrasting precipitates, not only exists as a thin film of approximately 5μm in extent at the grain boundaries, but also as precipitates in the grain interiors. The grain size was similar to those of single phase 48Ru52Al and roughly in the range between 200~400μm.

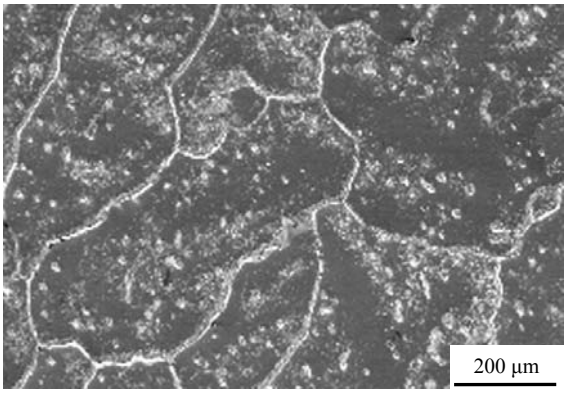

Fig. 3.16 SEM image of the microstructure of two phase 52Ru48Al alloy. δ phase existed both at grain boundaries and inside grains.

3.2.2 Displacement and Strain Maps

Fig. 3.17 ~ Fig. 3.23 show the maps of calculated displacement and strain components including: x–displacement maps, y–displacement maps, root mean square displacement maps, x–strain maps, y–strain maps, xy–strain maps (shear) and Von Mises effective strain maps, after each of the 4 stepped loading compression tests of the same cluster of grains. As in previous strain maps, "x" denotes the direction perpendicular to the external loading direction while "y" denotes the direction parallel to the external loading direction. Grain boundaries were highlighted artificially within the maps for easy recognition. For each of the displacement and strain components, the four maps are plotted under the same linear color scale.

In the x-displacement map, Fig. 3.17, the degree of heterogeneity increased as the external loading increased after each loading step. The displacement contour on the left portion of the map exhibited a correlation with the grain structure.

In the y-displacement map, Fig. 3.18, the displacement field after step 1 remained fairly uniform. Heterogeneity gradually developed in the subsequent loading steps and became prominent after step 4. The contour in the left portion of the maps also partly followed the grain structure, as observed in the x-displacement. The maximum of positive and negative again are roughly equal to each other.

In the root mean square displacement maps, Fig. 3.19, the heterogeneity can be seen through contours that developed into a triangular shape near the center after the four step loading tests. The contours in the left portion of the map followed part of the grain boundary as expected from results in x and y displacement maps.

In the x-strain map, Fig. 3.20, strains were mostly homogeneous following the first two steps of loading but areas of enhanced strain concentration, particularly near some of the grain boundaries started to appear after step 3. Another high strain area appeared to be initiated from a grain boundary triple point and extended further into nearby grains. After step 4, the initially high strain areas continued to experience enhanced straining. Interestingly, within the mostly tensile straining microstructure there was also some amount of compressive strains existing near the central areas of the maps, similar to those observed in single phase 48Ru52Al.

In the y-strain map, Fig. 3.21, strains also initially appeared fairly uniform and their average magnitude increased with external loading after the first two tests. A large degree of non-uniformity appeared following step 3 and 4. The areas that showed the highest strain concentration were essentially the same locations as those with high strain concentrations in the x-strain maps. One appeared near grain boundaries at lower left portion of the map and one near a grain boundary triple point in the right portion of the maps. But the intermixing of high and low strain areas in y-strain maps was more pronounced than in the x-strain maps.

In the shear strain maps, Fig. 3.22, just as in the x and y strain maps the strain distribution was fairly uniform after step 1 and 2. Strain heterogeneity became more observable following step 3 and 4. An appreciable amount of both positive and negative shear strains coexisted in the maps. Particularly, the high strain areas of both positive and negative shear tended to appear along or near grain boundary regions.

In the Von Mises effective strain maps, Fig. 3.23, strain heterogeneity started to develop after step 2, progressed into step 3 and became most prominent after step 4. Along some, but not all boundaries, there was enhanced straining. These enhanced straining areas appeared along the grain boundaries and extended into adjacent grain interior on both sides. Individual grains did not strain uniformly, with strains varying

as much as an order of magnitude within a single grain. Interestingly, bands with particular orientations—about 35˚ ~55˚ with respect to the external compressive axis also developed. The width of these enhanced strain bands was approximately 40μm on average. Detailed examination shows that some of these high strain bands, for example, the major one on the right of the map, appeared in δ-free regions that were sandwiched between δ abundant areas, indicating signs of precipitation hardening. Similar to single phase 48Ru52Al, the highest strains invariably appeared at grain boundary triple points. Low strain areas existed both in grain interiors as well as along grain boundaries, including triple points. Comparison among the strain maps reveals again a pattern of strain distribution developing at the very early stage of deformation and progressing in a self-similar manner to the higher strain levels.

Statistics of the effective strain maps are summarized in Table 3.2. The maximum to average ratio of strain within the maps was about a factor of 3, while the minimum to average ratio of strain was about a factor of 10 except for step 4. These ratios were very similar to the case of single phase 48Ru52Al.

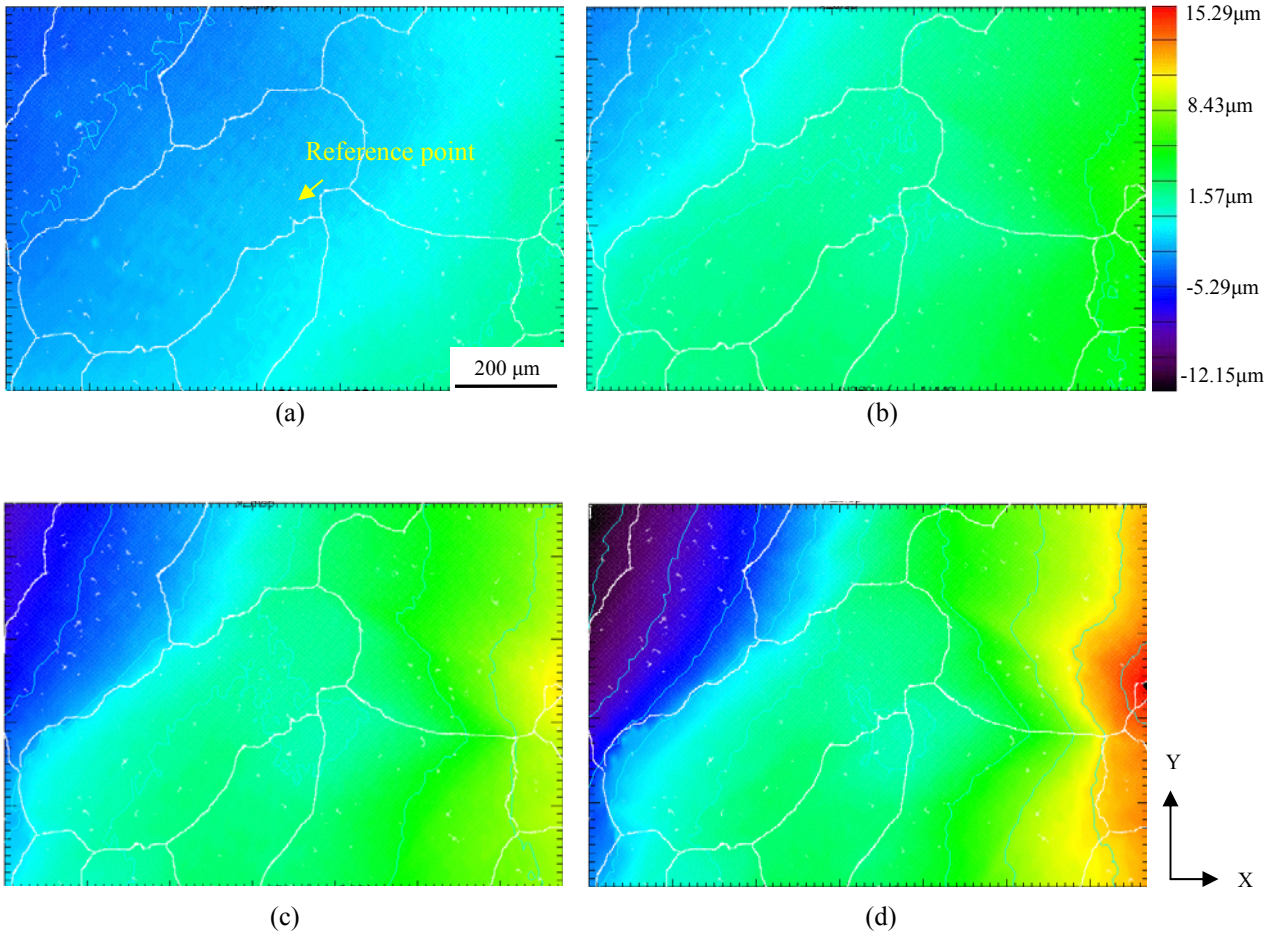

Fig. 3.17 X-displacement maps of two phase 52Ru48Al after (a) step i, 1.12% plastic strain; (b) step ii, 1.78% plastic strain; (c) step iii, 2.99% plastic strain and (d) step iv, 3.96% plastic strain.

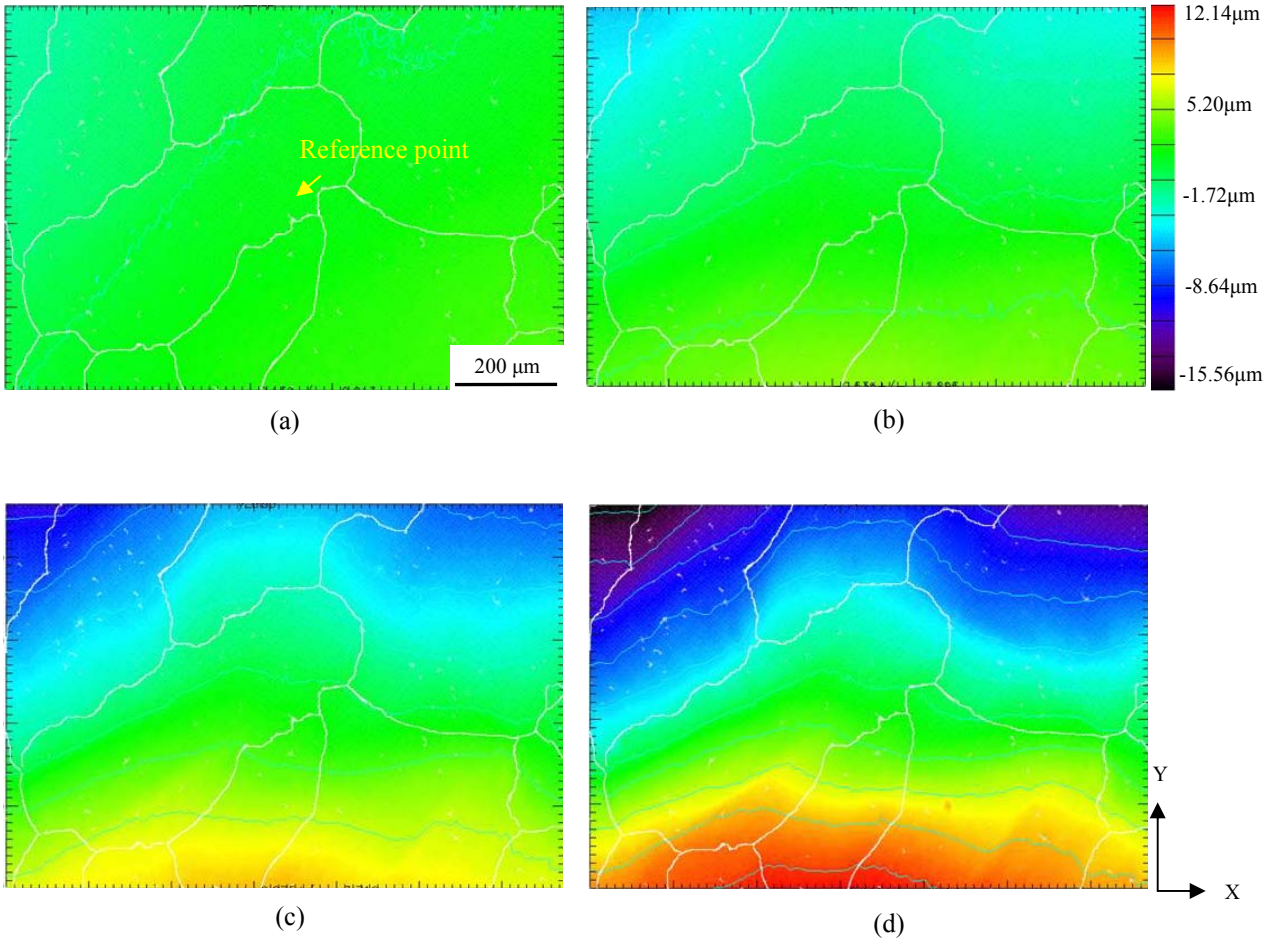

Fig. 3.18 Y-displacement maps of two phase 52Ru48Al after(a) step i, 1.12% plastic strain; (b) step ii, 1.78% plastic strain; (c) step iii, 2.99% plastic strain and (d) step iv, 3.96% plastic strain.

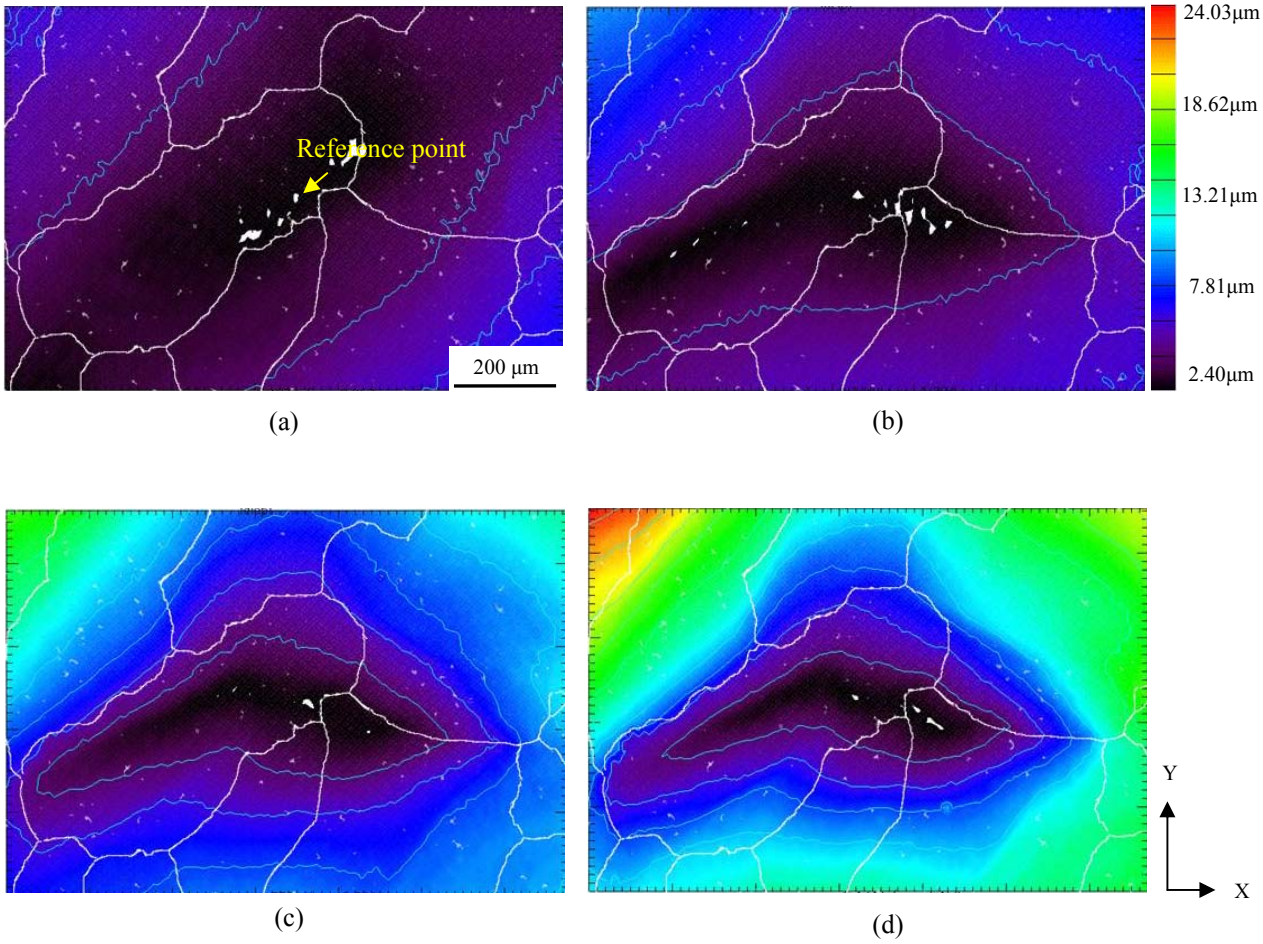

Fig. 3.19 Root mean square displacement maps of two phase 52Ru48Al after (a) step i, 1.12% plastic strain; (b) step ii, 1.78% plastic strain; (c) step iii, 2.99% plastic strain and (d) step iv, 3.96% plastic strain.

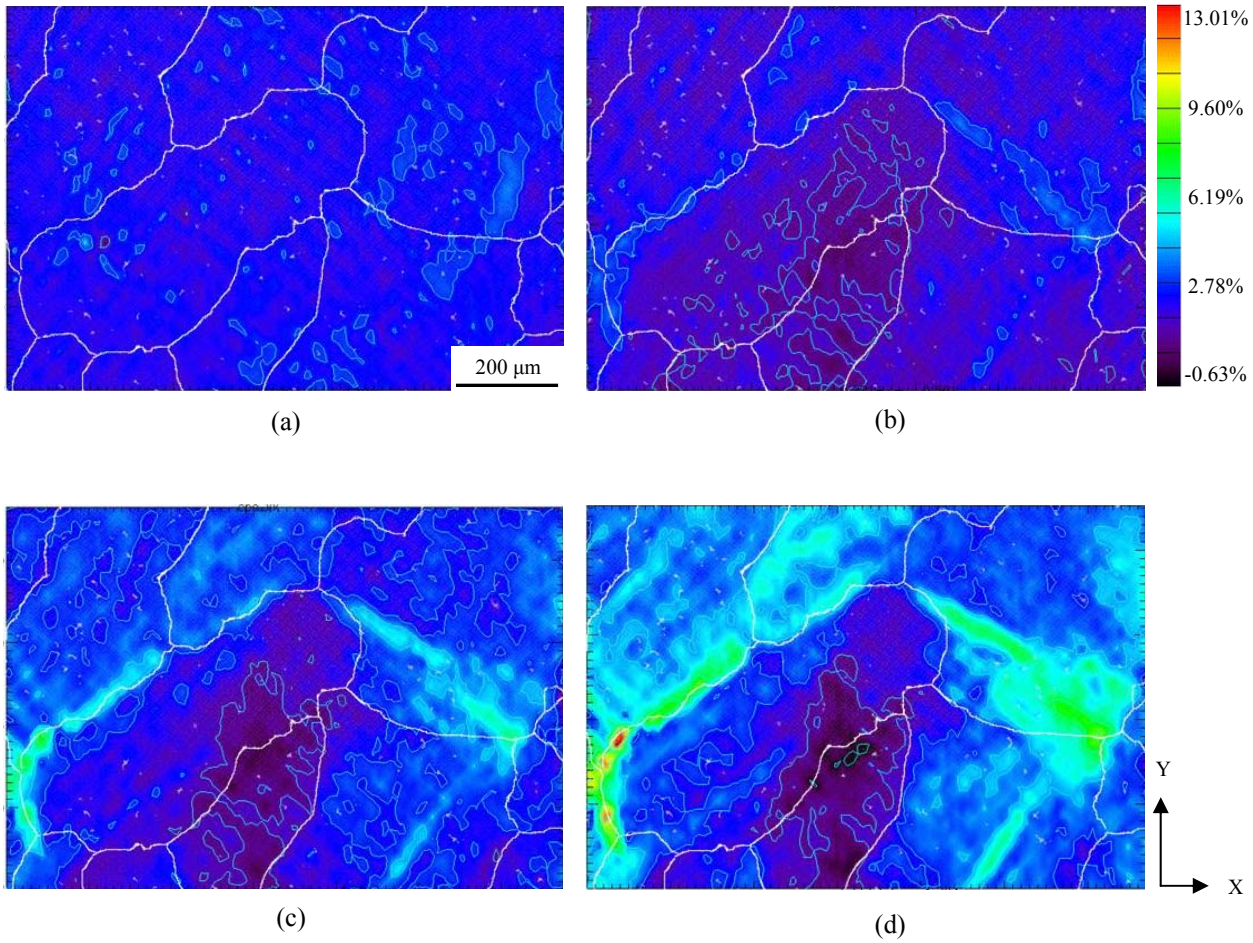

Fig. 3.20 X-strain maps of two phase 52Ru48Al after (a) step i, 1.12% plastic strain; (b) step ii, 1.78% plastic strain; (c) step iii, 2.99% plastic strain and (d) step iv, 3.96% plastic strain.

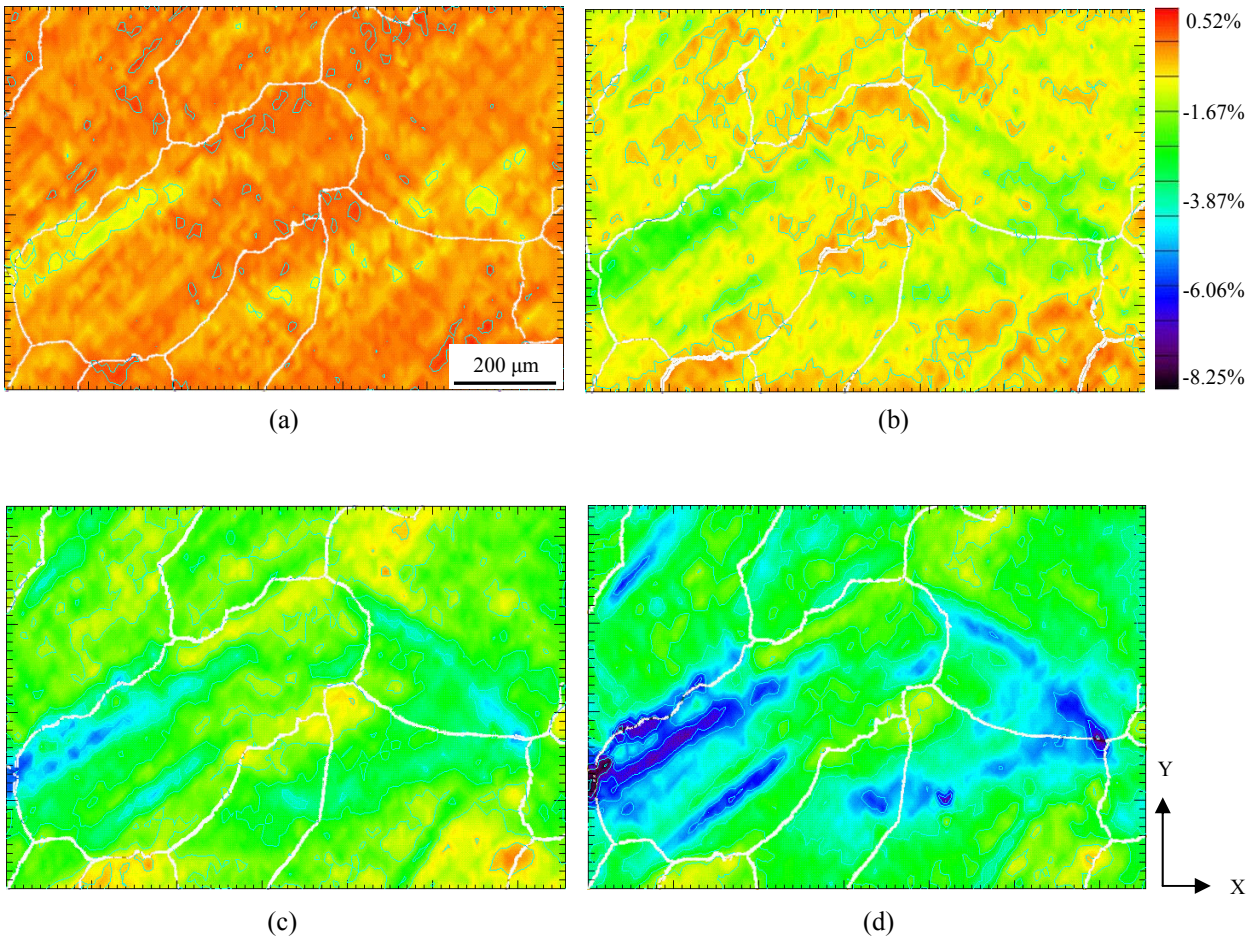

Fig. 3.21 Y-strain maps of two phase 52Ru48Al after (a) step i, 1.12% plastic strain; (b) step ii, 1.78% plastic strain; (c) step iii, 2.99% plastic strain and (d) step iv, 3.96% plastic strain.

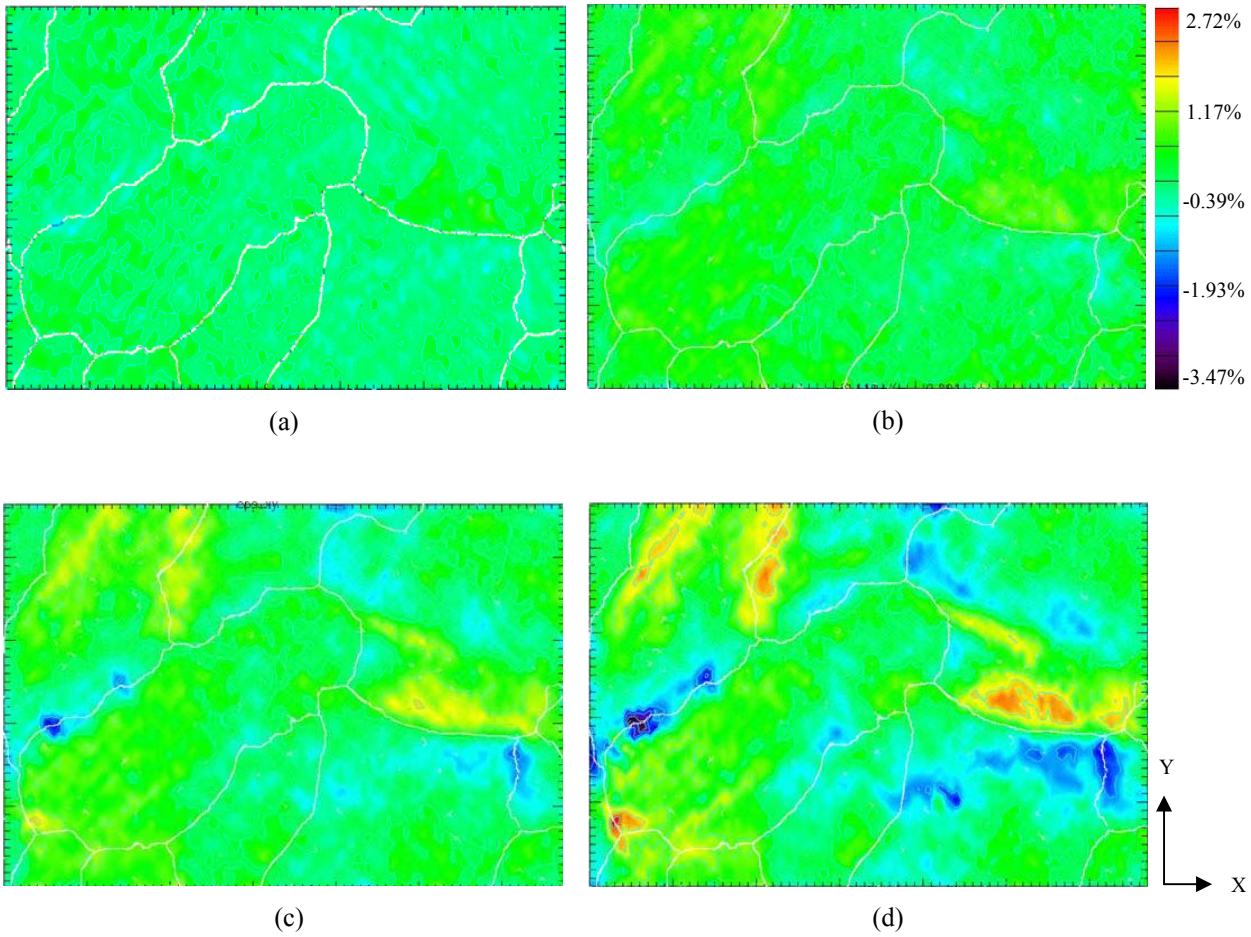

Fig. 3.22 XY-strain maps of two phase 52Ru48Al after (a) step i, 1.12% plastic strain; (b) step ii, 1.78% plastic strain; (c) step iii, 2.99% plastic strain and (d) step iv, 3.96% plastic strain.

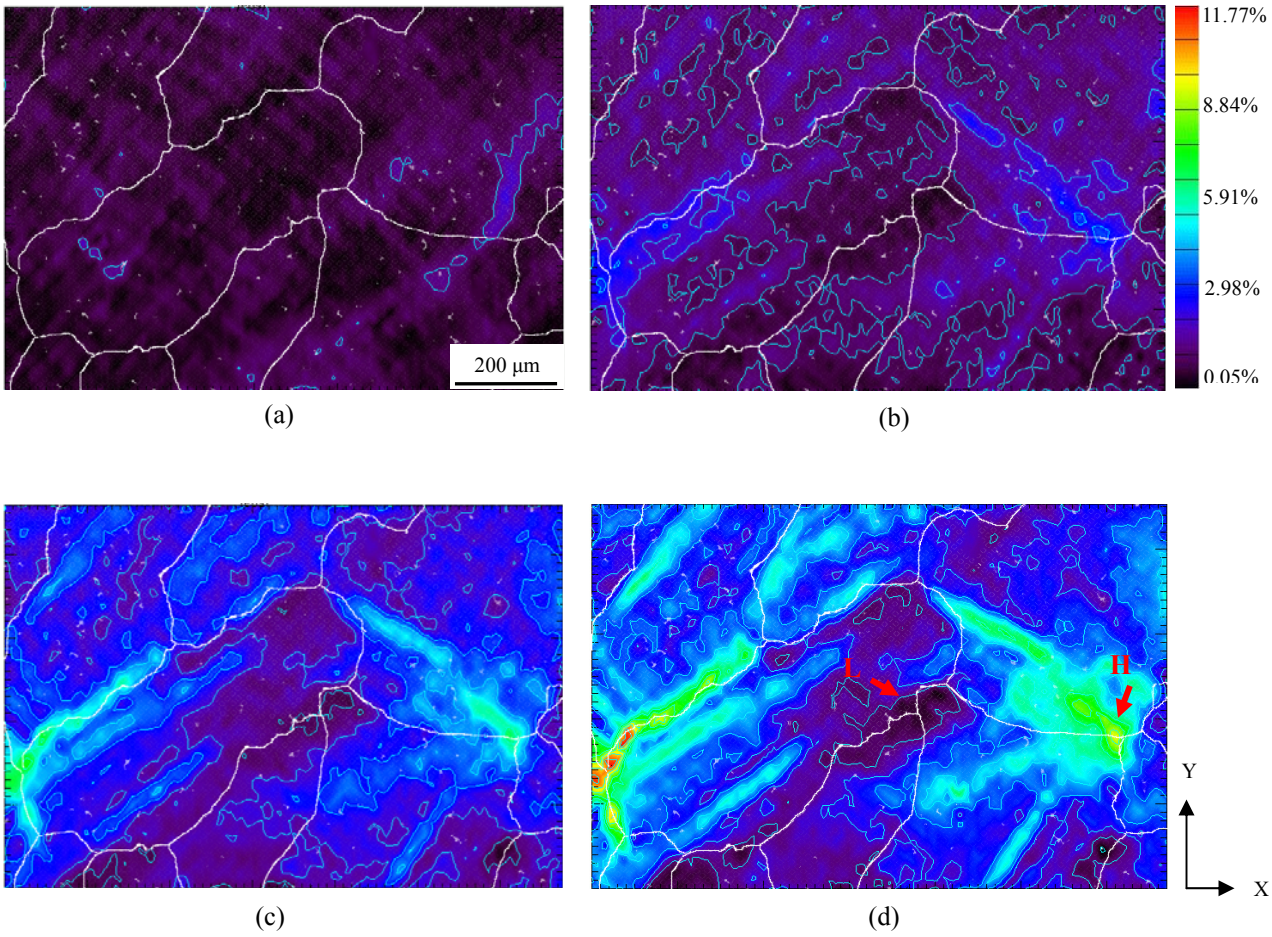

Fig. 3.23 Von Mises effective strain maps of two phase 52Ru48Al after (a) step i, 1.12% plastic strain; (b) step ii, 1.78% plastic strain; (c) step iii, 2.99% plastic strain and (d) step iv, 3.96% plastic strain.

Table 3.2 Statistics of effective strain maps of two phase 52Ru48Al alloy

	Nominal imposed strain	Avg. strain in the map	Std. dev. of Avg. strain	Max. in the map	Max. /Avg. strain ratio	Min. in the map	Min/Avg. strain ratio
Step 1	1.12%	0.84%	0.35%	2.12%	2.53	0.05%	0.06
Step 2	1.78%	1.26%	0.46%	3.51%	2.78	0.13%	0.10
Step 3	2.99%	2.56%	0.91%	7.35%	2.87	0.34%	0.13
Step 4	3.96%	3.89%	1.38%	11.77%	3.03	0.87%	0.22

3.2.3 Schmid Factor Calculation

Crystallographic orientations of the grains being investigated by strain mapping were also analyzed by EBSD before sample deformation. The results are shown in Fig. 3.24(a). Note that the 5μm step size used in the EBSD scan was ineffective for accurate identification of the Ru-rich δ phase and thus their orientation was not studied here. The composite Schmid plot as well as the Schmid plots for individual slip systems were also calculated and results are presented in Fig. 3.24(b)~(d).

According to the plots, there was a fairly large difference of the Schmid factors among neighboring grains, both reflected in the composite and individual Schmid factors plots. However, there existed no explicit correlation between large Schmid factors and enhanced strain concentration within individual grains. This is apparently due to the fact that high strain areas were mostly associated with grain boundary regions and also because the non-uniform distribution of δ precipitates influenced the overall strain distribution.

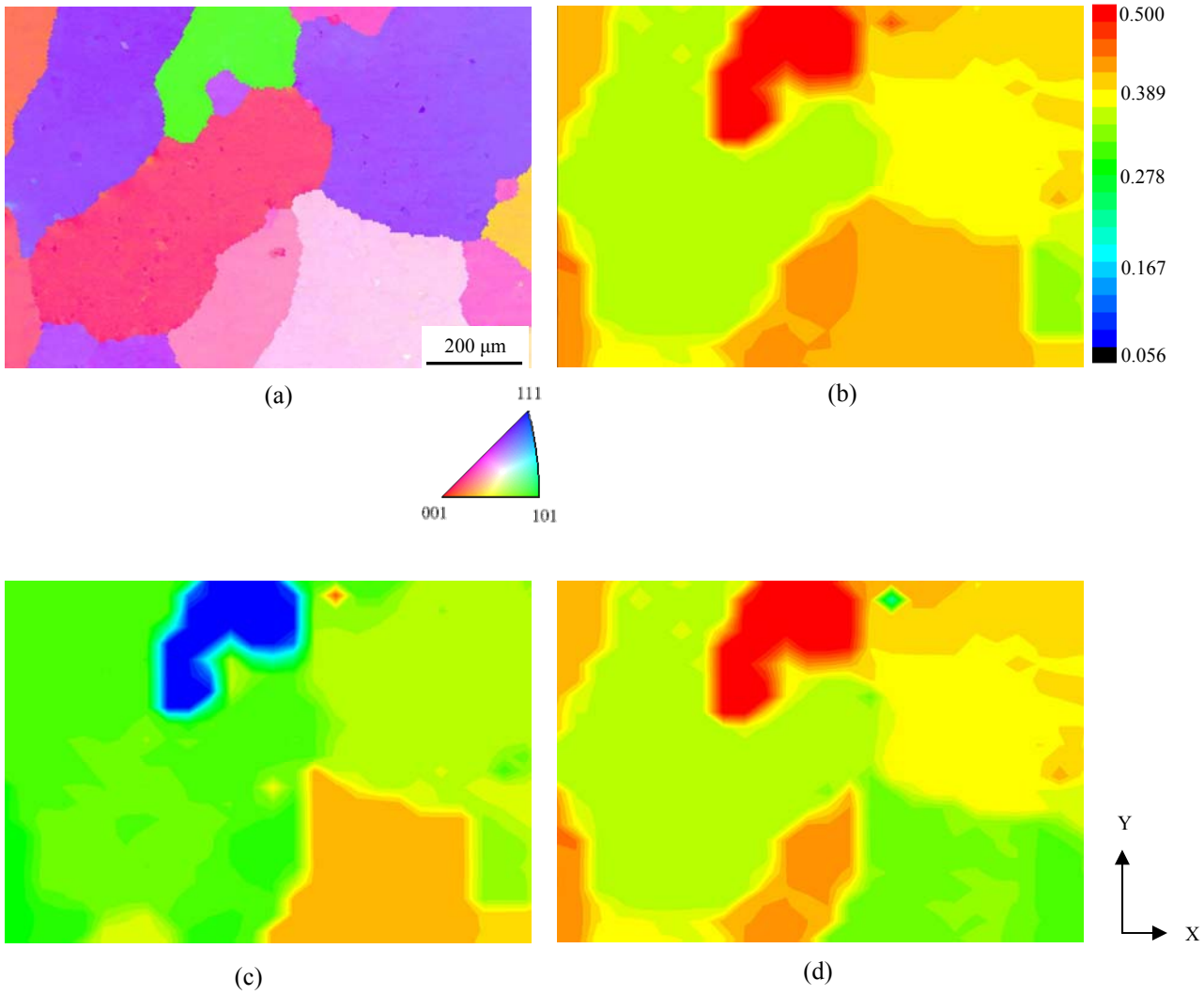

Fig. 3.24 (a) Grain orientation map of two phase 52Ru48Al, obtained by EBSD, (b) Composite Schmid factor plot for the maximum of <100>{110} or <110>{110}slip, (c) Schmid factor plot for <100>{110} slip system, (d) Schmid factor plot for <110>{110} slip system

3.2.4 Nanoindentation Tests

Nanoindentation experiments were conducted on the two existing phases in this alloy both before and after 3.96% nominal deformation. For nanoindentation prior to deformation, the indentation sites were randomly chosen from a large surface area of the sample. In tests of the post-deformation sample, the indentation sites were chosen from two representative locations: one close to a high strain grain boundary (indicated by "H" in Fig. 3.23(d)), one close to a low strain grain boundary (indicated by "L" in Fig. 3.23(d)). The applied load used in the tests was 12000μN (c.a. 1.2g), which was selected through a series of trial tests on the same material. Such loading was appropriate in that it can not only limit the indents to within the grain boundary phases, as shown in Fig. 3.25(a), but also efficiently minimizes the substantial fluctuations in the measured values typically seen at the low range of indentation loading [23].

Fig. 3.25(b) shows the result from the undeformed sample. It was observed that on average the measured hardness of the RuAl intermetallic (8.14GPa) is higher than that of Ru-rich δ phase (6.99GPa) before deformation. The scatter in these data is likely a combined result of minor microstructure variation and sample surface undulation. In addition, given that the softer Ru-rich δ phase was invariably confined between the slightly harder RuAl within areas that were comparable to the indentation size, as can be seen in Fig. 3.25(a), its measured hardness value may be somewhat higher than what would be measured in otherwise unconstrained volumes.

Fig. 3.25(c)~(d) are the results of nanoindentation experiments on the deformed sample, with Fig. 3.25(c) measured at the high strain location and Fig. 3.25(d) measured at the low strain location. It is observed that the hardness of Ru-rich δ phase increased significantly after deformation in both high strain and low strain regions; while that of RuAl intermetallic only increased slightly. The average measured hardness of Ru-rich δ phase after deformation was 10.80GPa, which increased by 54.5% compared to pre-deformation value. While that of RuAl intermetallic was 8.45GPa, which only increased by 3.8% compared to pre-deformation value. The

different hardness increment indicates that the grain boundary Ru-rich δ phase was likely to have deformed preferentially during straining.

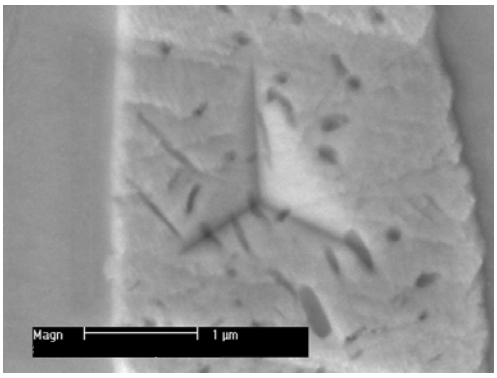

(a)

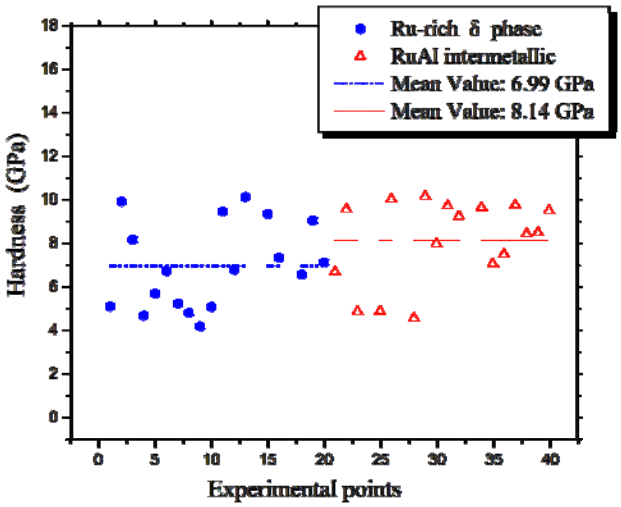

(b)

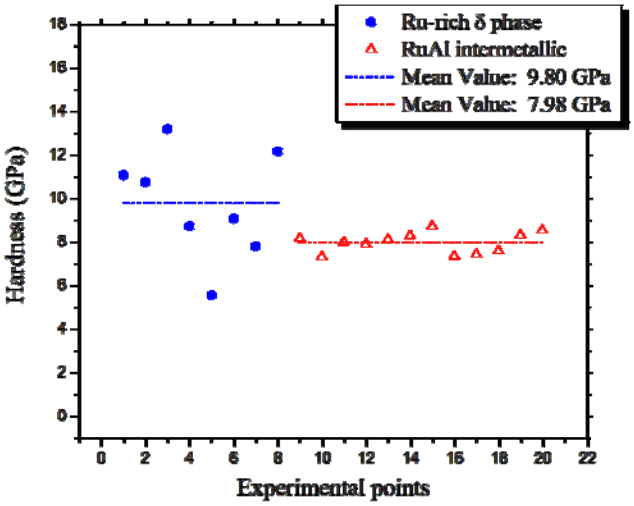

(c)

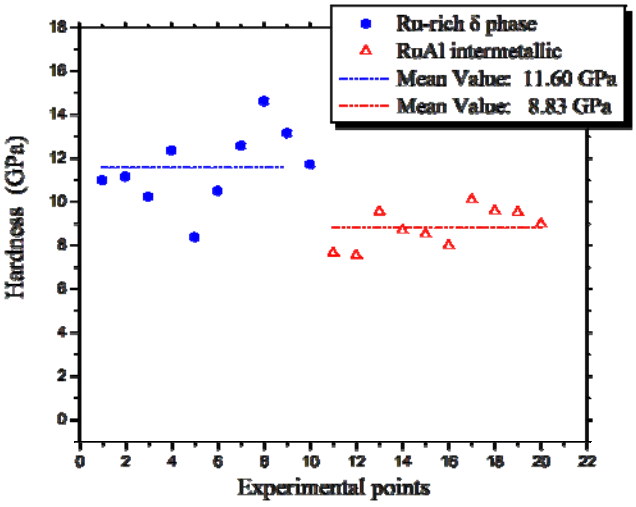

(d)

Fig. 3.25 (a) Indentation made on Ru-rich δ phase under 12000μN (c.a. 1.2g) load force, (b) Hardness data of undeformed two phase 52Ru48Al, (c) Hardness data of two phase 52Ru48Al after 3.96% nominal strain, at high strain boundary region, and (d) at low strain boundary region.

3.3 Two Phase 48Ru50Al2Nb-0.5B

3.3.1 Microstructure

Fig. 3.26 shows the microstructure image of this alloy. There was only intermediate amount of Ru-rich δ phase within this alloy with no precipitation in grain interiors. The δ phase only existed at grain boundaries as thin films of about 5μm thick. The grain size was also roughly in the range between 200~400μm.

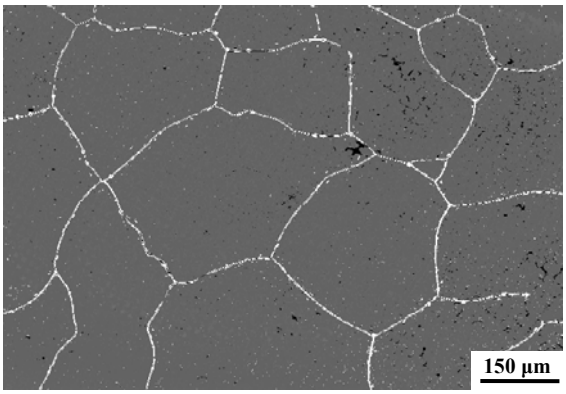

Fig. 3.26 SEM image of microstructure of two phase 48Ru50Al2Nb-0.5B alloy. δ phase existed along grain boundaries.

3.3.2 Displacement and Strain Maps

Fig. 3.27 ~ Fig. 3.28 show the displacement maps and strain maps after the only step of loading of 1.61% nominal strain conducted on this alloy. All the maps were superimposed with the microstructural image along with surface markers.

In the displacement maps, Fig. 3.27(a) ~ Fig. 3.27(c), a unique character is that the displacement contours followed many of the grain boundaries very closely. This is not observed in the previous cases of RuAl alloys, where there were δ precipitates in the grain interiors.

At 1.61% nominal compression, there exists large strain heterogeneity within the local microstructure. This is in sharp contrast to the other two alloys where the local strain distribution was fairly uniform at the stage below 2.0% nominal compression.

Moreover, the strain distribution pattern is similar to that of the two-phase 52Ru48Al alloy in that high strain areas mostly appeared along grain boundary regions, but only with a much stronger tendency. Typically, enhanced straining was observed within very narrow regions along grain boundaries and the immediate grain interiors no more than 10~15μm away. Note that the straining seems to be concentrated along grain boundaries that have a high degree of inclination relative to the stress axis. Most grain interiors, with one exception, all underwent a significantly lower level of straining, indicating that very steep strain gradients exist within grains. Again, the highest strains appear at one triple point of grain boundaries.

Statistics of the effective strain map, summarized in Table 3.3, display a maximum to average ratio of strain a factor of 4.35, currently the highest in this sort. The minimum to average ratio of strain was more than a factor of 10, similar to the observation in other alloys.

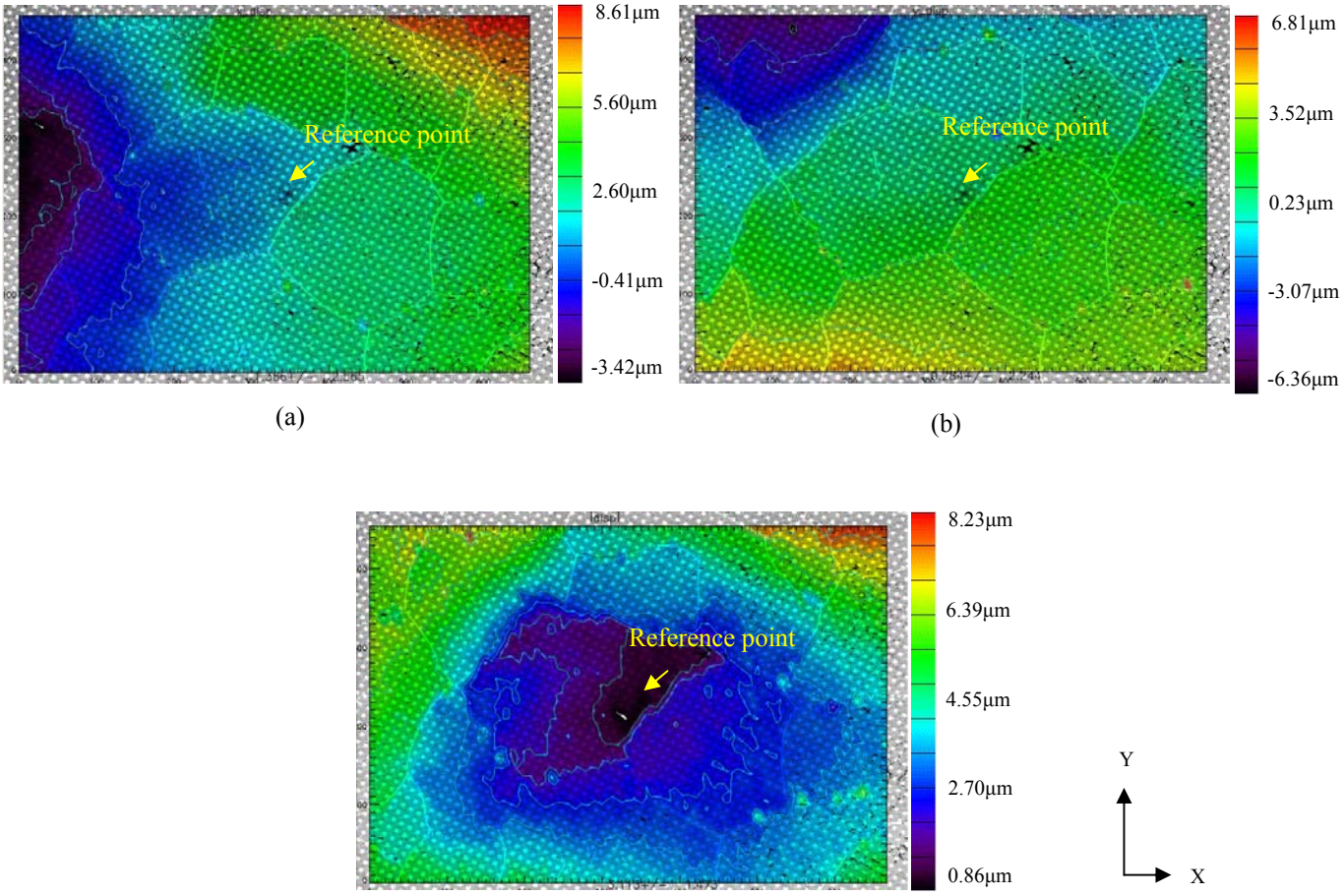

Fig. 3.27 (a) X displacement map, (b) Y displacement map, and (c) Root mean square displacement map of 48Ru50Al2Nb-0.5B after 1.61% nominal plastic strains

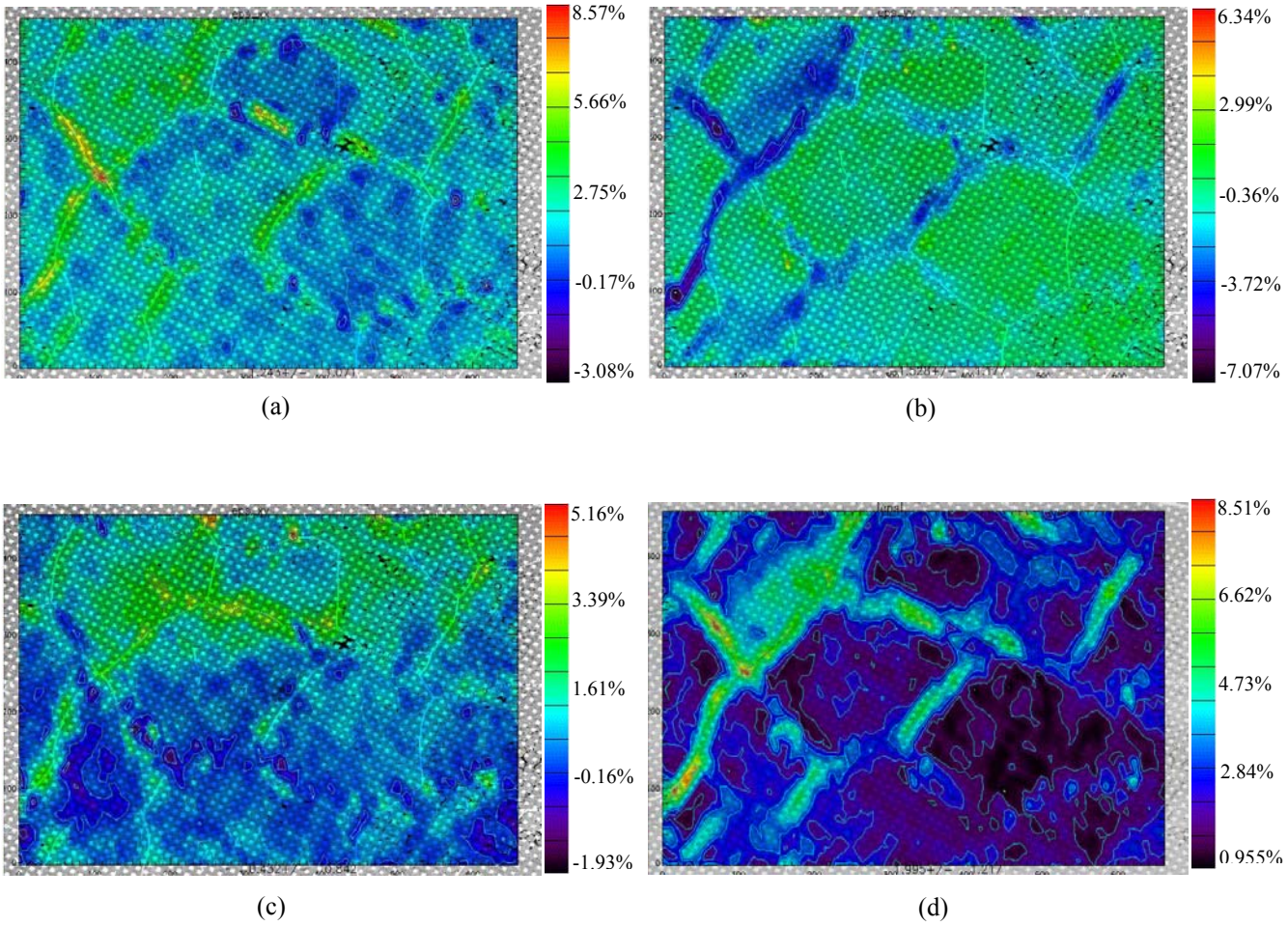

Fig. 3.28 (a) X strain map, (b) Y strain map, (c) XY strain map, and (d) Effective strain map of 48Ru50Al2Nb-0.5B after 1.61% nominal plastic

Table 3.3 Statistics of effective strain maps of two phase 48Ru50Al2Nb-0.5B alloy

	Nominal imposed strain	Avg. strain in the map	Std. dev. of Avg. strain	Max. in the map	Max. /Avg. strain ratio	Min. in the map	Min/Avg. strain ratio
Step 1	1.61%	2.00%	1.21%	8.61%	4.35	0.12%	0.06

CHAPTER 4

DISCUSSION

The unique combination of a variety of experimental techniques used in the current research provides a rich amount of information for assessment of the plastic behavior of RuAl from a multidimensional perspective. To the authors' knowledge, these are the first studies that directly connect the macroscopic straining patterns with the local microstructure features as well as the underlying dislocation activity. The results not only aid in understanding how the activities of different slip systems and the presence of ductile secondary phase influence the heterogeneous straining behavior of RuAl, but also provide broader insights into more general issues such as the strain gradient theory and the formulation of finite element models for local straining. In this chapter, individual sections discuss these issues in more detail.

4.1 Deformation Heterogeneity in RuAl

The Von Mises effective strain maps of different compositions of RuAl alloys show considerable strain heterogeneity after a few percent of nominal compressive strain, with substantial influence of local microstructure. Strains vary by a factor of 3 (higher) to 10 (lower) from the mean imposed strains within the neighborhood of several grains. This is interesting, given the availability of two different slip systems in this material. The details of strain heterogeneity vary from alloy to alloy and are sensitive to the amount of Ru-rich δ phase present. In the single phase 48Ru52Al, different grains accumulated different amounts of strain after each step of loading, indicating that some grains were initially more favorable for deformation. In the two-phase RuAl materials, however, the strain distribution patterns were completely different with the presence of δ phase. Instead of displaying a grain-wise difference of strain concentration with some grains accumulating a higher amount of total strain

than others, the enhanced strains tend to appear at regions near grain boundaries. This effect becomes more pronounced in 48Ru50Al2Nb-0.5B where the δ phase only existed at the boundaries. In this case, strains were largely concentrated within narrow regions along grain boundaries, leaving most inner grain areas with strains significantly lower than the macroscopically imposed value. The appearance of δ phase within grain interiors, as in 52Ru48Al, was accompanied by higher strain concentration within inner grain areas. Detailed examination shows that the inner grain high strain regions were loosely associated with δ free regions that were sandwiched between δ abundant areas. Given the characteristics of strain redistribution in the cases of two phase alloys, it is likely that the presence of δ phase introduced an additional precipitate hardening effect into the overall plastic response of the local microstructure. With a different crystal structure (HCP) and active slip system, the phase boundary between RuAl and δ can serve as an effective barrier to dislocation glide, which manifests itself through high strain concentration in the δ free region.

Multi-grain crystal plasticity modeling has demonstrated that strain heterogeneity is a typical feature following deformation [4, 69, 70]. Modeling of deformation in polycrystalline intermetallic lamellar γ/α_2 TiAl also reveals a large degree of strain heterogeneity [4]. More intriguing is that in the modeling results of TiAl, the ratio between effective strain and nominal imposed strain ranges between 3.5X ~ 0X at 1% nominal strain level, very similar to the current observations in RuAl compounds. However, strain mapping presents more details of heterogeneity at the individual grain level than has been predicted by crystal plasticity. For example, strain mapping results obtained from experiments with a similar level of nominal straining reveal the presence of patchy-like uneven distributions of high and low strain regions within individual grains in single phase RuAl alloy. Additionally, bands of enhanced strains at or near grain boundary regions were observed in two phase RuAl alloys. Conversely, inner grain strain distributions in the plasticity modeling results for TiAl typically display a gradual transition between different strain levels across the entire individual grain. The inability of plasticity modeling of TiAl to capture greater details

of strain heterogeneity may be a result of assumptions regarding operative slip modes as well as due to the use of a coarse mesh, which fails to provide high enough spatial resolution. Compared to over a hundred markers per grain utilized in strain mapping, the modeling of TiAl only has approximately 20 mesh grid points per grain in a two dimensional setting. Nevertheless, the fact that the much coarser grid used in the modeling of TiAl yields a similar degree of strain heterogeneity on a grain-to-grain basis compared to current experimental observations on several RuAl alloys is interesting. The degree to which this heterogeneity can be attributed to differences in grain orientations compared to lamellar orientations is unclear. Further modeling with assumptions more relative to the RuAl plastic behavior would clearly be interesting.

Another distinctive feature of the strain maps is the appearance of self-similar straining patterns at different stages of loading, as was evident in both single phase 48Ru52Al and two phase 52Ru48Al, where the high strain regions appeared in the first loading stage persisted through all the subsequent stages of increased imposed strain and, ultimately, achieved maximum values of approximately 10% effective strain. According to the basic laws used in crystal plasticity modeling, i.e. the Schmid law, softer (more favorably) oriented grains will preferentially deform in the early stages of deformation. For materials that display normal hardening behavior, it is generally anticipated that when the softer areas harden and become more difficult to deform, further deformation will be mostly concentrated within grains that undergo relatively less amount of deformation during initial straining. Under these conditions, local deformation will not display self-similar strain heterogeneity patterns during different stages of straining. It is interesting to note that such self-similar straining patterns were also observed in experiments conducted on TiAl alloys [71]. Given the high strain hardening rates in these intermetallics [72], this behavior is somewhat unexpected. Since no previous experiments have been focused this closely on the initial stages of finite straining in materials, the current literature fails to address in any detail what extent of hardening is required to shift loading from softer grains to initially harder ones. Therefore, the significance of these self-similar straining patterns remains to be elucidated. More systematic strain mapping experiments that cover

higher strain loading spectra are needed to provide further insights into this phenomenon.

4.2 Analysis of Slip Activity in Single Phase 48Ru52Al

4.2.1 Dominance of <110>{110} Slip System in RuAl

Coupled with strain mapping, the application of EBSD grain orientation analysis and FIB-assisted TEM dislocation investigation with targeted foil removal provides a unique opportunity to isolate and assess the influence of individual slip systems on the local straining behavior of RuAl. Prior studies on dislocation substructures in RuAl have typically revealed the presence of both <100> and <110> dislocations [7, 18]. Thus it has been unclear which system would be preferred in terms of the ease of activation of the system. In the case of single phase 48Ru52Al, the results of composite Schmid factor calculation, Fig. 3.9(b), did not correlate well with the actual strain development profile. This might be anticipated since at least some difference in the critical resolved shear stress between the <100> and <110> slip systems could be expected, due to the difference in the magnitude of the Burgers vectors. Calculation of dislocation line tensions [67] have indicated a lower energy for <100> dislocations compared to <110> dislocations. Thus it might be expected that initiation of <100> slip would be easier than <110> slip under equal conditions. It is interesting that <110>{110} slip system is dominant within the grains studied here, as confirmed both by the results of Schmid factor analysis and dislocation substructure investigations, where within the most heavily deformed grain “A”, a larger <110>{110} Schmid factor coincided with a higher density of <110> dislocations.

The plastic behavior of the two phase materials was qualitatively different from the single phase RuAl. The Schmid factor calculations for two phase 52Ru48Al found no explicit correlation between high strain concentrations and large Schmid factors for either slip system. The fact that high strains tended to be concentrated near the grain boundary indicates that the stress/strain state developed within the

microstructure of the two phase alloys is different from within grains and at boundaries in the single phase alloy. It is likely that the presence of Ru-rich δ phase both at inner and inter grain regions triggered a redistribution of stress during loading not only around the periphery of individual grains but also inside them. The collective impact of such a complicated local stress state may no longer be approximated by a simple uniaxial loading scenario.

The dominant presence of <110> slip in the single phase 48Ru52Al could be influenced by a number of factors, including availability of <100> v.s. <110> dislocation sources within individual grains, difference in the critical resolved shear stress (CRSS) between the two slip systems, and the specific mechanical constraints imposed on the locally straining grains. TEM analyses of the as-cast microstructure have revealed the existence of both <100> and <110> dislocations [67]. The uneven distribution of such pre-existing dislocations together with other easily activated dislocation sources along with variations in Schmid factors from grain to grain could alter the local straining behavior in a manner that favors a certain type of slip with the most abundantly available sources.

Regarding the CRSS of the two slip systems in RuAl, the authors are not aware of any detailed measurement of their values; this is apparently due to the difficulty of growing single crystals of this high melting point, high Al content compound. Nevertheless, the dominant presence of <110> dislocations observed in this study and the correlation between <110>{110} Schmid factors and the strain distribution collectively suggests that the critical resolved shear stress for <110>{110} slip is lower than <100>{110}. Previous studies have also observed a slightly higher density of <110> dislocations, compared to <100> type following room temperature straining [6, 7]. Since these investigations combined have covered alloys with varying composition including Ru-rich, stoichiometric and Al-rich alloys, the influence on slip activation due to small departures from stoichiometry can be largely ruled out. It is possible that the more frequent activity of <110> dislocations is a result of the different core structure of the <100> compared <110> dislocations that leads to their different CRSS. The core structures of <100> and <110> dislocations are known to be

very different in NiAl, where <100> dislocations have compact cores and <110> dislocations undergo frequent dissociation and decomposition, subsequently limiting their mobility [73]. This leads to a dominance of <100> dislocations in the deformation of NiAl at room temperature. The difference in dislocation core structure between different slip systems in RuAl is unlikely to be as large as that in NiAl, given that both types of dislocations appear in the post-deformed materials. However, additional high resolution TEM experiments are needed to reveal the details of the core structures of the <100> and <110> dislocations in RuAl.

Last but not least, although local geometry constraints almost certainly affect the straining behavior of individual grains, given the strain concentrations in the vicinity of grain boundaries, their influence on the distribution of <110> v.s. <100> dislocations did not appear to be strong. A more detailed examination of this issue would be possible with bicrystal straining experiments conducted with the assistance of strain mapping.

4.2.2 Implications for Failure Modes

The dominance of <110>{110} dislocations in certain individual grains following the deformation of single phase 48Ru52Al raises concerns on the potential loss of local grain-to-grain compatibility during deformation, since the availability of <110> slip alone cannot produce the five independent slip systems necessary to meet the Von Mises criteria for compatible deformation. Therefore, grains with only one slip system dominant during straining may have the tendency to serve as “flaws” within the microstructure, potentially leading to premature failure. However, the effective strain maps showed that even though the total strain was as high as 9.8% near the boundary between grain “A” and “D”, the grain boundary managed to maintain its integrity without failing. It is unclear whether additional <100> slip systems beyond the <110> slip systems were triggered due to the need for slip transfer between neighboring grains [74, 75], or it is simply because that this particular pair of grains did have the sufficient slip systems required to maintain local compatibility. Additional orientation analysis as well as dislocation substructure studies on areas across the boundary

region may shed light on the issue.

Premature failure along grain boundaries is a complex process. It could be aided by contamination, intrinsic structural defects, geometry of the boundaries and/or the orientation of the boundaries with respect to external loading. While contamination and intrinsic structural defects have been subjects of research on the ductility of FeAl and NiAl [76-80], very limited efforts have been placed on RuAl. The only minor element known to affect the behavior of the grain boundary is boron, which helps shift the fracture mode from brittle to ductile and thus improves the ductility of polycrystalline aggregates [6]. However, little has been established as to how boron may affect the grain boundary of polycrystalline aggregates of RuAl [24].

Another potential problem with grain boundaries in RuAl is the Al enrichment at the boundaries, which could result in as much as 10 at.% higher of Al concentration at grain boundaries than in the matrix [6]. Such a large degree of deviation from stoichiometry could introduce additional phases at the grain boundaries. The latest Ru-Al binary phase diagram reveals a Al_3Ru_2 intermetallic phase existing near the composition of 60 at% Al [19], as shown in Fig. 1.2. The crystal structure of Al_3Ru_2 has been identified as tetragonal, which is of lower symmetry compared to the B2 structure of RuAl. The possible existence of multiple phases with different crystal structures at the grain boundaries is likely to complicate the mechanical response of the boundaries. While no such phases were observed in the present study, further TEM phase identification work is needed to study the structure of the grain boundaries across a range of composition.

4.3 Strain Gradients and Geometrically Necessary Dislocations

During plastic deformation, dislocations will nucleate, glide, and interact with each other. As a result, some dislocations glide through the entire crystal lattice and exit from the bulk material either at free surfaces or at grain boundaries that act as sinks of dislocations. Some interact with dislocations of opposite Burgers vectors and get annihilated; and some interact with other dislocations and become trapped inside the material. Among the dislocations that are finally stored inside the bulk material, a

portion of them exist in an ordered manner in order to support the distorted crystal lattice. These are the so-called geometrically necessary dislocations.

The observed strain heterogeneity following deformation of single phase 48Ru52Al is the result of complex dislocation activity encompassing all the aforementioned types. Using the simple Orowan relationship between dislocation density and macroscopic shear strain [81], one can estimate the density of the dislocations that are necessary to produce the strain by gliding through the crystal lattice during the plastic process:

$$\gamma = \rho b \bar{x} \qquad (4.1)$$

where γ is the macroscopic strain, ρ is the dislocation density, b is the Burgers vector, and $\bar{x}$ is the average slip distance of the dislocations. Two bounding assumptions are considered for $\bar{x}$. In the first case, assuming $\bar{x}$ to be the same as the grain size, which is approximately 200μm; while in the second case, the dislocations glide and are immobilized by interaction with the grown-in dislocations in the as-processed condition. In this case, $\bar{x}$ equals to the inverse square root of the density of grown-in dislocations (ρ=4.5×$10^{12}$$m^{-2}$), which is 4.7×$10^{-7}$m

Applying this relation to high strain grain "A" and assuming the effective strains were approximately 10%, the range of density of mobile dislocations to accomplish this strain would be between 1.2×$10^{12}$$m^{-2}$ and 5.1×$10^{14}$$m^{-2}$ (*a=0.298nm, b=1.41a*). Given that the estimated density of dislocations that are stored inside the lattice in this grain following deformation is approximately 1.3×$10^{14}$$m^{-2}$, this suggests that the average glide distance of dislocations is only a very small fraction of the grain size. This further suggests that a large fraction of the gliding dislocations involved in the plastic straining process were ultimately trapped inside the grains; i.e., the majority of the observed dislocations are "statistically stored dislocations". Only those that were initially close to the free surfaces or grain boundaries were able to exit the grains and reduce the distorted state of crystal lattice behind them.

In order to assess the relationship between strain gradient and GNDs, a distinction needs to be made between the gradients of strain measured by strain

mapping and those that are treated in strain gradient plasticity theory. What strain mapping measures is the total distortion of the material, including both plastic and elastic distortions. On the other hand, the gradients that are thought to be associated with GNDs are plastic strain gradients [35]. Therefore, strictly speaking the strain gradient measured by strain mapping is not directly associated with GNDs. However, given the ratio of the total measured density of SSDs to the total measured density of GNDs, i.e. at the very least 4:1 (and this ratio is likely to be even higher at the near boundary high strain region in grain A, for ρ_{SSD} is expected to be higher while ρ_{GND} remains relative constant according to the measured results), the total strain gradients measured by strain mapping primarily reflect the magnitude of the real plastic strain gradients caused by inhomogeneous deformation of grain A, but do not provide a direct indication of the gradients required to maintain compatibility between grains. Based on these observations, there is no explicit correlation between the presence of large strain gradients and the existence of large density of GNDs under the local microstructural conditions studied. From this one could further infer that no substantial hardening results from these GNDs. For GNDs to become significant to hardening, the statistical glide process would need to be suppressed and the GNDs distributed differently than observed in this study. Whether this could happen at grain sizes less than 10μm is unclear.

To summarize, although GNDs serve the role to supporting lattice curvature, their linkage to the abnormal hardening of materials at the micro scale may not be as important as originally thought by many researchers. Application of the present research approach to finer grain materials and/or to different loading paths could provide further insight.

4.4 Role of Intergranular Phases and Precipitates

Using an indentation method, Wolff *et al.* [22] found that the intergranular δ phase observed in all of the three ternary alloy systems based on RuAl was harder than the RuAl intermetallic matrix in the as-solidified condition. They suggested that the improved toughness in Ru-rich two phase alloys was due to the additional

deformability of HCP δ phase under local constraints. However, there remain concerns on the validity of comparing hardness data obtained under significantly different indentation loading as applied in their research. When conducting the indentation measurement, Wolff *et al.* applied a 1kg load when measuring the hardness of RuAl intermetallic and only a 25g load when measuring the hardness of δ phase, obviously due to its much localized existence. Nonetheless, it is well known that the size of indent has substantial influence on the resultant measured value of the hardness [23], particularly in the small loading spectrum. Under the loading difference as large as two orders of magnitude, any attempt to reveal the true hardness difference between these two phases will be very difficult. Thus, a more reliable way to compare the relative hardness between the RuAl intermetallic phase and grain boundary δ phase needs to be carried out using identical indentation loading.

In the present study nanoindentation experiments using a 12000μN (c.a. 1.2g) load force for both phases showed that the δ phase was indeed softer than the RuAl intermetallic phase before deformation. The average of 54.5% hardness increase of δ phase following the nominal 3.96% deformation indicated that it underwent significant hardening during deformation at both high strain and low strain grain boundaries. The hardness of RuAl intermetallic grains, on the other hand, only gained a slight average increase of 3.8% after the deformation. This confirmed that the Ru-rich δ phase is softer and does deform preferentially than RuAl intermetallic during straining, just as the typical behavior of a compliant layer in a brittle matrix. This suggests that the two phase structure of RuAl has the potential to achieve improved toughness through a manner similar to the compliant layer toughening mechanism found in other composites and alloy systems [82-87].

The ductile phase toughening mechanism has previously been observed in several alloy systems, such as WC/Co [82, 83], Al_2O_3/Al [84, 85], MgO/Ni, Fe or Co [86] and TiAl/Nb [87]. The mechanisms that result in an overall improved toughness in the otherwise brittle matrix can be attributed to the presence of a secondary ductile phase that causes crack bridging, blunting or deflection, or all of them during deformation. Similar ductile phase toughening, involving the γ' phase (Ni_3Al) was also observed in

B2 β-NiAl intermetallic with more extensive subsequent research. The first study to identify possible advantages of a β + γ' microstructure was conducted by Pank *et al.* [88] in Ni-20Co-30Al system. The two phase structure resulted in 0.5% ductility in tensile tests compared to nearly zero ductility of single phase β alloy. Later study by Ishida *et al.* [89] also revealed significant improvement of room temperature ductility in the Ni-Al-X system, with X being either Fe, Co or Cr. More recently, room temperature tensile ductility as high as 10~12% was achieved in the directionally solidified Ni-30Fe-20Al alloy by Misra *et al.* [90].

A study on the interface of the two phases using TEM has pinpointed traces of slip transmitted from ductile γ' phase into the harder β-NiAl phases through the nucleation of dislocations at the interphase interface [90-92]. This slip transfer mechanism was believed to largely account for the improved ductility of the alloys. Calculation of slip geometry across the interface suggested that the slip transfer between two different phases can also be similarly explained through a mechanism that was used to describe slip transfer between grain boundaries in polycrystalline single phase alloys [74, 93]. This particular mechanism requires three criteria to be met before a successful slip transmission can happen: 1.) The angle between the lines of the intersection of incoming and outgoing slip planes at the boundary should be minimized (shown as angle α in Fig. 4.1), 2.) The resolved shear stress on the out going slip system from the pile up dislocations at the boundary should be maximized, 3.) The magnitude of the Burgers vector of the residual dislocation left at the boundary after completion of slip transfer should be minimized.

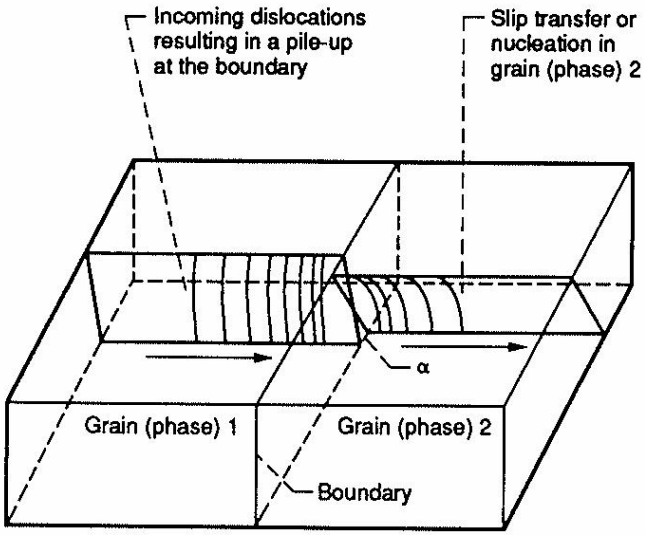

Fig. 4.1 Slip transfer across a grain/phase boundary, adapted from Noebe *et al.* [94]

Similarities between the microstructure of two phase NiAl and two phase RuAl certainly indicate a potential for RuAl to exhibit similar deformation behavior. Based on current strain map observations, the enhanced strain concentration along some of the grain boundaries after deformation could both be signs of precipitate strengthening and/or signs of a certain degree of slip transfer through the grain boundary δ phase into the immediate RuAl intermetallic matrix. The injection of mobile dislocations into the nearby RuAl matrix may readily induce a higher degree of plastic deformation of the matrix near the boundary as compared to those inner grain areas that lack such addition dislocations. Conversely, the availability of diverse active slip systems within the RuAl matrix also makes it easier to satisfy the slip geometry requirement across the phase boundary.

The ductile phase toughening of RuAl, if true, could be potentially superior to other high temperature intermetallic systems in that the ductile phase has an even higher melting temperature than the intermetallic matrix. This eliminates the drawback of limiting the high temperature capability due to a lower melting temperature of the ductile phase compared to matrix such as in the case of β+ γ' NiAl

system [94].

Although no direct evidence has been found so far for the existence of a slip transfer mechanism in the deformation of RuAl, the experimental techniques applied in the current research are certainly well suited to further research with that focus.

The presence of a softer Ru-rich δ phase also seems to provide additional strengthening effects through precipitation hardening, as was evident by the appearance of some of the high strain bands within a δ-free region of the grain interior that was sandwiched by nearby δ-abundant areas. Although the precipitated δ phase was softer than the matrix, with a crystal structure different than that of the matrix, the interface between precipitate and matrix can provide an effective barrier to prevent dislocations from cutting through the precipitate, and the matrix is therefore strengthened. Since the size of δ precipitates is no larger than the size of individual markers, the high strain areas observed around δ are likely the mixed result of preferential deformation of δ and the hardening of the matrix around these softer precipitates. In addition, grain boundary geometry, structure and the availability of nearby dislocation sources can also be factors that result in the observed strain enhancement effect. Areas that lack dislocation sources will be difficult to deform and remain in a relatively low straining state compared to others that are abound in dislocation sources.

4.5 Implications for Finite Element Modeling

Finite element modeling of crystal plasticity has gone from the early stage of modeling plastic behavior of single crystals [95, 96] into the more advanced level of understanding the plastic response of polycrystalline aggregates [69, 97, 98]. Recent efforts have focused on incorporating strain gradients into the constitutive relations in an attempt to capture the missing length scale ubiquitously present in all plasticity modeling [25, 31-33, 35, 99-101]. By using finer meshes and improved constitutive relations, the intra and inter grain behavior can be captured with higher precision [70]. However, within current plasticity models, some of the key microstructure features that have significant impact on the overall plastic response of materials, for example

the behavior of grain boundary and the random initial distribution of dislocations and defects, are still missing. Understandably, there will be a certain degree of inaccuracy in any plasticity models due to the lack of such critical information, particularly at the low strains relevant to intermetallics. As shown in the current study of RuAl alloys the measured local plastic response, in this case among a few neighboring grains, has a higher degree of variation than plasticity modeling can predict [4, 69]. This is obviously due to the fact that deformation of real microstructures is subjected to the complex local conditions that are beyond the consideration of any currently available anisotropic hardening laws. Although at the meso-scale, large strain plasticity modeling may easily neglect the aforementioned microstructure features, as the modeling scale becomes increasingly smaller and overall strains are lower, these challenges need to be addressed. In fact, the success of any strain gradient plasticity theory that is scale sensitive may partly lie in its ability to incorporate the behavior of key microstructural features, such as the grain boundary region which acquires an increasingly larger fraction of the entire material as the grain size decreases, into the governing law of deformation.

Easily imagined, the challenges faced when attempting to incorporate a full spectrum of microstructure features into the crystal plasticity model are daunting. It not only requires astronomical computational power but also demands a complete understanding of the characteristics of the relevant microstructure features. For example, with respect to grain boundary regions, the study of 48Ru52Al shows that the strains in the vicinity of the grain boundaries under certain loading conditions can be very different within the neighborhood of just a few grains. While some boundaries fail at less than 2% effective strain, others can sustain strain as high as almost 10%. Such variation of strength could be due to intrinsic (boundary structure variation) as well as extrinsic (local constraints and interaction with neighbors) factors which are difficult to quantify. The scale at which such inhomogeneities exist calls for suitable techniques that can be used to explore relevant plasticity issues at the same scale. The combination of strain mapping and several other advanced experimental techniques adopted in the current research provides an effective avenue for gaining such crucial

insights. It is foreseeable that with an adequate amount of experimental information generated on the local microstructural scale, the behavior of key microstructures can be statistically integrated into the governing laws of crystal plasticity and contribute to the establishment of new models that may eventually be applied to any length scale.

Last but not least, the successful implementation of strain mapping also provides a unique way to experimentally verify the effects of mesh refinement in finite element modeling. Since the spacing of markers is an ideal one to one experimental representation of the mesh size, comparison between strain mapping results obtained by using increasingly smaller markers to the results of modeling using a finer mesh will certainly shed light on the choice of optimum mesh size that balances modeling accuracy and computation efficiency. In addition, the detailed strain distribution present in strain maps clearly indicates the magnitude and extent to which gradients are likely to appear. All these can be very valuable information to crystal plasticity theorists who are struggling to incorporate strain gradients into their new models.

CHAPTER 5

CONCLUSIONS

1. Surface displacement mapping is an effective tool for the study of strain development at the local grain scale.
2. The local straining behavior of RuAl alloys exhibits a significant degree of heterogeneity, with the total strain varying by a factor of 10~300% from the average value within the neighboring grains.
3. The strain distribution patterns varied from alloy to alloy and are sensitive to the amount and location of Ru-rich δ phase present.
4. The Ru-rich δ phase is softer than the RuAl intermetallic and deforms preferentially during straining.
5. In single phase alloys, different grains accumulated different amounts of strain, while in two phase alloys, enhanced strains tended to concentrate at the grain boundaries. All the alloys studied displayed self-similar straining pattern during different stages of loading.
6. Using FIB-assisted TEM dislocation analysis, in single phase 48Ru52Al, a grain that exhibited higher concentration of effective strains was shown to possess a higher dislocation density compared to another grain that displayed a low concentration of effective strains. A higher density of <110> dislocations compared to <100> dislocations was observed in the most heavily strained grain.
7. Based on strain mapping, EBSD grain orientation analyses and dislocation substructure investigation, the <110>{110} slip system is favored over the <100>{110} slip system for the local microstructural conditions studied in single phase 48Ru52Al.
8. In single phase 48Ru52Al alloy, higher total strains within individual grains

resulted in a higher GND density as well as a higher fluctuation in its magnitude. On a one to one basis, the presence of large total strain gradients did not result in a detectable increase of total GND density.

CHAPTER 6

FUTURE WORK

Current research has pointed out a few key issues that should be addressed in future studies. The information generated through these investigations would significantly improve the overall understanding of the plastic behavior of RuAl and would be generally relevant to other polycrystalline materials.

1. The CRSS of <110>{110} & <100>{110} individual slip systems

This issue is important to the in-depth understanding of the plastic behavior of RuAl and would be a high priority item for future research. The experimental attempts at measuring the CRSS of these systems have been unsuccessful because of the difficulty of fabricating single crystal specimen for mechanical testing. However, the latest advancements on micro scale mechanical testing [102] provides an experimental alternative to the aforementioned dilemma. Using FIB, single crystal micro cylindrical samples can be fabricated from individual grains in polycrystalline material for compression testing using nanoindentation with a modified flat tip indenter. A prior survey using OIM would need to be conducted to select grains with proper orientations. It should be pointed out that the size of the cylindrical specimen should not be too small such that size effects may arise during compression testing and complicate the following analysis.

2. Possible Slip Transfer Mechanism between Grains and Phases

The improved ductility in two phase NiAl alloys points to possible improvement of the ductility and toughness in RuAl. Therefore, it is important to see if the deformation of RuAl bears similar characteristics. The combined application of strain

mapping, OIM, FIB-assisted TEM enables a more detailed characterization of the slip transfer mechanism in that it can take into account the influence of local straining status and the orientations of neighboring grains/phases with respect to external loading direction. This research will require the study of dislocation substructure across the grain/phase boundaries where the information of strain concentration and the orientations of the involved microstructure are readily available through strain mapping and OIM.

3. Grain Boundary Structure

Since strong grain boundaries are one of the important factors for robust microstructures in polycrystalline materials, it is necessary to study factors that have potential impact on the local mechanical response of the grain boundary of polycrystalline RuAl. This will include TEM investigation of possible structural variation at grain boundaries due to Al enrichment, Auger electron spectroscopy study of grain boundary contaminations and effects of boron on modifying the strength of grain boundaries.

4. Self-similarity of heterogeneous pattern at higher strains

The self similar straining pattern observed during stepped loading tests suggests a behavior not yet been revealed by plasticity modeling. It will be interesting to see to what degree of deformation this type of behavior continues. More systematic tracking of strain heterogeneity from low to high strains is necessary to gain further insights into the development of strains. Corresponding FIB-assisted TEM investigation of dislocation substructure evolution at different level of straining will be very helpful in this case. However, since this inevitably involves the destruction of local microstructure, more intelligent ways of experimentation are needed to meet the requirement of both techniques.

APPENDIX

APPENDIX I

Composite Schmid factor of <110>{110} & <100>{110} slip

```
%%%%%%%%%%%%%%%%%%%%%%%%%%%%%%%%%%%%%%%%%%%%%%%%%%%%%%%%%%%%%%%%%%%%%%%%%%%%
%
%  This code is used for the case when external system (RD TD ND) is rotating
% about itself and bring itself into accordance with crystallographic
% system <100>----Bunge's definition of Euler angle
%
%%%%%%%%%%%%%%%%%%%%%%%%%%%%%%%%%%%%%%%%%%%%%%%%%%%%%%%%%%%%%%%%%%%%%%%%%%%%

% Open OIM scan file (*.ang)
fid1=0;
  while fid1<1
   filename=input('Open file:','s');
   [fid1, message]=fopen(filename,'r');
   if fid1==-1
   disp(message)
   end
  end
% Open file for storing the calculated schmid_factor_matrix
fid2=fopen('100&110 Schmid factor summary-es rotate.txt','w');
fprintf(fid2,'\tX \tY \tphi1 \tPHI \tphi2 \tSchmid Factor \tSlip system
activated \n');

fid3=fopen('100&110 Schmid factor summary for origin-es
rotate.txt','w');
fprintf(fid3,'\tX \tY \tSchmid Factor\n');


% Skip the annotation lines starting with '#' in .ang file
finish=1;
while (feof(fid1)==0) & (finish==1)
  finish=0;
  line=fgetl(fid1);
  matches=findstr(line, '#');
  if matches==1
    finish=1;
  end
end


% Read the first 5 data from each line;
% These 5 data correspond to: phi1, PHI, ph2, x, y of each scanning point
while feof(fid1)==0            % Not at the end of the file
   A=fscanf(fid1,'%20f',9);    % Read in the first 5 data

   bad_point=0;
   if A(7)==-1.0
        bad_point=1;

% confidence index = -1.0 meaning the data point is a bad one we then set
% the schmid factor of these point to be zero;

    end

% Calculate the indice of RD in the crystallographic coordinate system
```

```
% base on Bunge' definition of Euler angle
 u=cos(A(1))*cos(A(3))-sin(A(1))*sin(A(3))*cos(A(2));
 v=-cos(A(1))*sin(A(3))-sin(A(1))*cos(A(3))*cos(A(2));
 w=sin(A(1))*sin(A(2));
 RD=[u v w];


   % Schmid factor of {110}<110> slip systems

M1=abs(((RD*[1;1;0])/(norm(RD)*norm([1;1;0])))*((RD*[1;-1;0])/(norm(R
D)*norm([1;-1;0]))));


M2=abs(((RD*[1;-1;0])/(norm(RD)*norm([1;-1;0])))*((RD*[1;1;0])/(norm(
RD)*norm([1;1;0]))));


M3=abs(((RD*[1;0;1])/(norm(RD)*norm([1;0;1])))*((RD*[1;0;-1])/(norm(R
D)*norm([1;0;-1]))));


M4=abs(((RD*[1;0;-1])/(norm(RD)*norm([1;0;-1])))*((RD*[1;0;1])/(norm(
RD)*norm([1;0;1]))));


M5=abs(((RD*[0;1;1])/(norm(RD)*norm([0;1;1])))*((RD*[0;1;-1])/(norm(R
D)*norm([0;1;-1]))));


M6=abs(((RD*[0;1;-1])/(norm(RD)*norm([0;1;-1])))*((RD*[0;1;1])/(norm(
RD)*norm([0;1;1]))));

   % Schmid factor of {110}<100> slip systems

m1=abs(((RD*[1;1;0])/(norm(RD)*norm([1;1;0])))*((RD*[0;0;1])/(norm(RD
)*norm([0;0;1]))));


m2=abs(((RD*[1;-1;0])/(norm(RD)*norm([1;-1;0])))*((RD*[0;0;1])/(norm(
RD)*norm([0;0;1]))));


m3=abs(((RD*[1;0;1])/(norm(RD)*norm([1;0;1])))*((RD*[0;1;0])/(norm(RD
)*norm([0;1;0]))));


m4=abs(((RD*[1;0;-1])/(norm(RD)*norm([1;0;-1])))*((RD*[0;1;0])/(norm(
RD)*norm([0;1;0]))));


m5=abs(((RD*[0;1;1])/(norm(RD)*norm([0;1;1])))*((RD*[1;0;0])/(norm(RD
)*norm([1;0;0]))));


m6=abs(((RD*[0;1;-1])/(norm(RD)*norm([0;1;-1])))*((RD*[1;0;0])/(norm(
RD)*norm([1;0;0]))));

   % Find the slip system with the largest schmid factor
```

```
   % then store the calculated value together with the activated
   % slip system representation;
   B=[M1 M2 M3 M4 M5 M6 m1 m2 m3 m4 m5 m6];
   [y,i]=max(B);           % y stores the maximum value, i stores the
                         % the indice of the maxima in the vector


   switch bad_point
      case 0
        fprintf(fid2,'%10.3f %10.3f    %10.3f %10.3f %10.3f
\t%10.3f',A(4:5),A(1:3),B(i));
        fprintf(fid3,'%10.3f  \t%10.3f  \t%10.3f\n',A(4:5),B(i));

% Write the result into file including the coordinates of the scanning
% point, which is x=A(4) & y=A(5)

      case 1
        fprintf(fid2,'%10.3f %10.3f    %10.3f %10.3f %10.3f
\t%10.3f',A(4:5),A(1:3),0);
        fprintf(fid3,'%10.3f  \t%10.3f  \t%10.3f\n',A(4:5),0);

% fid2 and fid3 are two different files


   end

   switch i
      case 1
        fprintf(fid2,'\t(1,1,0)[1,-1,0]\n');
      case 2
        fprintf(fid2,'\t(1,-1,0)[1,1,0]\n');
      case 3
        fprintf(fid2,'\t(1,0,1)[1,0,-1]\n');
      case 4
        fprintf(fid2,'\t(1,0,-1)[1,0,1]\n');
      case 5
        fprintf(fid2,'\t(0,1,1)[0,1,-1]\n');
      case 6
        fprintf(fid2,'\t(0,1,-1)[0,1,1]\n');
      case 7
        fprintf(fid2,'\t(1,1,0)[0,0,1]\n');
      case 8
        fprintf(fid2,'\t(1,-1,0)[0,0,1]\n');
      case 9
        fprintf(fid2,'\t(1,0,1)[0,1,0]\n');
      case 10
        fprintf(fid2,'\t(1,0,-1)[0,1,0]\n');
      case 11
        fprintf(fid2,'\t(0,1,1)[1,0,0]\n');
      case 12
        fprintf(fid2,'\t(0,1,-1)[1,0,0]\n');
   end


end  % End while
fclose(fid1);
fclose(fid2);
fclose(fid3);
```

Schmid factor of <110>{110} slip

```
%%%%%%%%%%%%%%%%%%%%%%%%%%%%%%%%%%%%%%%%%%%%%%%%%%%%%%%%%%%%%%%%%%%%%
%%%%%%
%%%     This code is used for the case when external system (RD TD ND)  %%%
%%%  is rotating about itself and bring itself into accordance with      %%%
%%%  crystallographic system <100>----Bunge's definition of Euler angle
%%%
%%%%%%%%%%%%%%%%%%%%%%%%%%%%%%%%%%%%%%%%%%%%%%%%%%%%%%%%%%%%%%%%%%%%%

% Open OIM scan file (*.ang)
fid1=0;
  while fid1<1
   filename=input('Open file:','s');
   [fid1, message]=fopen(filename,'r');
   if fid1==-1
   disp(message)
   end
  end

% Open file for storing the calculated schmid_factor_matrix
fid2=fopen('110 Schmid factor summary-es rotate.txt','w');
fprintf(fid2,'\tX \tY \tphi1 \tPHI \tphi2 \tSchmid Factor \tSlip system
activated \n');

fid3=fopen('110 Schmid factor summary for origin-es rotate.txt','w');
fprintf(fid3,'\tX \tY \tSchmid Factor\n');

% Skip the annotation lines starting with '#' in .ang file
finish=1;
while (feof(fid1)==0) & (finish==1)
  finish=0;
  line=fgetl(fid1);
  matches=findstr(line, '#');
  if matches==1
    finish=1;
  end
end



% Read the first 5 data from each line;
% These 5 data correspond to: phi1, PHI, ph2, x, y of each scanning point
while feof(fid1)==0           % Not at the end of the file
```

```
   A=fscanf(fid1,'%20f',9);    % Read in the first 5 data

   bad_point=0;
   if A(7)==-1.0            % confidence index = -1.0 meaning the data
                            % point is a bad one
      bad_point=1;          % we then set the schmid factor of these point
                            %  to be zero;
   end

% Calculate the indice of RD in the crystallographic coordinate system
% base on Bunge' definition of Euler angle
 u=cos(A(1))*cos(A(3))-sin(A(1))*sin(A(3))*cos(A(2));
 v=-cos(A(1))*sin(A(3))-sin(A(1))*cos(A(3))*cos(A(2));
 w=sin(A(1))*sin(A(2));
 RD=[u v w];

% Schmid factor of {110}<110> slip systems

M1=abs(((RD*[1;1;0])/(norm(RD)*norm([1;1;0])))*((RD*[1;-1;0])/(norm(R
D)*norm([1;-1;0]))));

M2=abs(((RD*[1;-1;0])/(norm(RD)*norm([1;-1;0])))*((RD*[1;1;0])/(norm(
RD)*norm([1;1;0]))));

M3=abs(((RD*[1;0;1])/(norm(RD)*norm([1;0;1])))*((RD*[1;0;-1])/(norm(R
D)*norm([1;0;-1]))));

M4=abs(((RD*[1;0;-1])/(norm(RD)*norm([1;0;-1])))*((RD*[1;0;1])/(norm(
RD)*norm([1;0;1]))));

M5=abs(((RD*[0;1;1])/(norm(RD)*norm([0;1;1])))*((RD*[0;1;-1])/(norm(R
D)*norm([0;1;-1]))));

M6=abs(((RD*[0;1;-1])/(norm(RD)*norm([0;1;-1])))*((RD*[0;1;1])/(norm(
RD)*norm([0;1;1]))));


   % Find the slip system with the largest schmid factor
   % then store the calculated value together with the activated
   % slip system representation;
   B=[M1 M2 M3 M4 M5 M6];
   [y,i]=max(B);           % y stores the maximum value, i stores the
                        % the indice of the maxima in the vector
```

```
   switch bad_point
      case 0
         fprintf(fid2,'%10.3f %10.3f    %10.3f %10.3f %10.3f
\t%10.3f',A(4:5),A(1:3),B(i));   % Write the result into file including
                                  % the coordinates of the scanning point
         fprintf(fid3,'%10.3f  \t%10.3f  \t%10.3f\n',A(4:5),B(i));
                                  % which is x=A(4) & y=A(5)
      case 1
         fprintf(fid2,'%10.3f %10.3f    %10.3f %10.3f %10.3f
\t%10.3f',A(4:5),A(1:3),0);      % fid2 and fid3 are two different files

         fprintf(fid3,'%10.3f  \t%10.3f  \t%10.3f\n',A(4:5),0);
   end

   switch i
      case 1
        fprintf(fid2,'\t(1,1,0)[1,-1,0]\n');
      case 2
        fprintf(fid2,'\t(1,-1,0)[1,1,0]\n');
      case 3
        fprintf(fid2,'\t(1,0,1)[1,0,-1]\n');
      case 4
        fprintf(fid2,'\t(1,0,-1)[1,0,1]\n');
      case 5
        fprintf(fid2,'\t(0,1,1)[0,1,-1]\n');
      case 6
        fprintf(fid2,'\t(0,1,-1)[0,1,1]\n');
   end


end  % End while
fclose(fid1);
fclose(fid2);
fclose(fid3);
```

Schmid factor of <100>{110} slip

```
%%%%%%%%%%%%%%%%%%%%%%%%%%%%%%%%%%%%%%%%%%%%%%%%%%%%%%%%%%%%%%%%%%%%%%%%
%%%%%%
%%%     This code is used for the case when external system (RD TD ND)  %%%
%%%  is rotating about itself and bring itself into accordance with      %%%
%%%  crystallographic system <100>----Bunge's definition of Euler angle
%%%
%%%%%%%%%%%%%%%%%%%%%%%%%%%%%%%%%%%%%%%%%%%%%%%%%%%%%%%%%%%%%%%%%%%%%%%%

% Open OIM scan file (*.ang)
fid1=0;
  while fid1<1
   filename=input('Open file:','s');
   [fid1, message]=fopen(filename,'r');
   if fid1==-1
   disp(message)
   end
  end

% Open file for storing the calculated schmid_factor_matrix
fid2=fopen('100 Schmid factor summary-es rotate.txt','w');
fprintf(fid2,'\tX \tY \tphi1 \tPHI \tphi2 \tSchmid Factor \tSlip system
activated \n');

fid3=fopen('100 Schmid factor summary for origin-es rotate.txt','w');
fprintf(fid3,'\tX \tY \tSchmid Factor\n');

% Skip the annotation lines starting with '#' in .ang file
finish=1;
while (feof(fid1)==0) & (finish==1)
  finish=0;
  line=fgetl(fid1);
  matches=findstr(line, '#');
  if matches==1
    finish=1;
  end
end



% Read the first 5 data from each line;
% These 5 data correspond to: phi1, PHI, ph2, x, y of each scanning point
while feof(fid1)==0           % Not at the end of the file
   A=fscanf(fid1,'%20f',9);    % Read in the first 5 data
```

```
   bad_point=0;
   if A(7)==-1.0            % confidence index = -1.0 meaning the data
                             % point is a bad one
       bad_point=1;         % we then set the schmid factor of these point
                             % to be zero;
   end

% Calculate the indice of RD in the crystallographic coordinate system
% base on Bunge' definition of Euler angle
 u=cos(A(1))*cos(A(3))-sin(A(1))*sin(A(3))*cos(A(2));
 v=-cos(A(1))*sin(A(3))-sin(A(1))*cos(A(3))*cos(A(2));
 w=sin(A(1))*sin(A(2));
 RD=[u v w];

% Schmid factor of {110}<100> slip systems

m1=abs(((RD*[1;1;0])/(norm(RD)*norm([1;1;0])))*((RD*[0;0;1])/(norm(RD
)*norm([0;0;1]))));

m2=abs(((RD*[1;-1;0])/(norm(RD)*norm([1;-1;0])))*((RD*[0;0;1])/(norm(
RD)*norm([0;0;1]))));

m3=abs(((RD*[1;0;1])/(norm(RD)*norm([1;0;1])))*((RD*[0;1;0])/(norm(RD
)*norm([0;1;0]))));

m4=abs(((RD*[1;0;-1])/(norm(RD)*norm([1;0;-1])))*((RD*[0;1;0])/(norm(
RD)*norm([0;1;0]))));

m5=abs(((RD*[0;1;1])/(norm(RD)*norm([0;1;1])))*((RD*[1;0;0])/(norm(RD
)*norm([1;0;0]))));

m6=abs(((RD*[0;1;-1])/(norm(RD)*norm([0;1;-1])))*((RD*[1;0;0])/(norm(
RD)*norm([1;0;0]))));

% Find the slip system with the largest schmid factor
% then store the calculated value together with the activated
% slip system representation;
B=[m1 m2 m3 m4 m5 m6];
[y,i]=max(B);           % y stores the maximum value, i stores the
                         % the indice of the maxima in the vector


   switch bad_point
```

```
     case 0
        fprintf(fid2,'%10.3f %10.3f    %10.3f %10.3f %10.3f
\t%10.3f',A(4:5),A(1:3),B(i));   % Write the result into file including
                                 % the coordinates of the scanning point
        fprintf(fid3,'%10.3f  \t%10.3f  \t%10.3f\n',A(4:5),B(i));
                                   % which is x=A(4) & y=A(5)
     case 1
        fprintf(fid2,'%10.3f %10.3f    %10.3f %10.3f %10.3f
\t%10.3f',A(4:5),A(1:3),0);      % fid2 and fid3 are two different files

        fprintf(fid3,'%10.3f  \t%10.3f  \t%10.3f\n',A(4:5),0);
  end

  switch i
    case 1
      fprintf(fid2,'\t(1,1,0)[0,0,1]\n');
    case 2
      fprintf(fid2,'\t(1,-1,0)[0,0,1]\n');
    case 3
      fprintf(fid2,'\t(1,0,1)[0,1,0]\n');
    case 4
      fprintf(fid2,'\t(1,0,-1)[0,1,0]\n');
    case 5
      fprintf(fid2,'\t(0,1,1)[1,0,0]\n');
    case 6
      fprintf(fid2,'\t(0,1,-1)[1,0,0]\n');
  end


end  % End while
fclose(fid1);
fclose(fid2);
fclose(fid3);
```

REFERENCES

1. Yamaguchi M, Umakoshi Y. Prog Mater Sci 1990;34:1.
2. Baker I. Mater Sci Eng A 1995;192-193:1.
3. Biery N, De Graef M, Beuth J, Raban R, Elliott A, Austin C, Pollock TM. Metall Mater Trans A 2002;33A:3127.
4. Brockman RA. Int J Plast 2003;19:1749.
5. Fleischer RL, Zabala RJ. Metall Trans A 1990;21A:2709.
6. Fleischer RL, Field RD, Briant CL. Metall Mater Trans A 1991;22A:403.
7. Lu DC, Pollock TM. Acta Mater 1999;47:1035.
8. Pollock TM, Lu DC, Shi X, Eow K. Mater Sci Eng A 2001;317:241.
9. Nandy TK, Feng Q, Banerjee D, Gigliottf MFX, Pollock TM. in *Defect Properties and Related Phenomena in Intermetallic Alloys* 2003, Warrendale, PA, 2003, p. 89.
10. Nandy TK, Feng Q, Pollock TM. Script Mater 2003;48:1087.
11. Feng Q, Nandy TK, Tryon B, Pollock TM. Intermetallics 2004;12:755.
12. Spitsberg IT, Darolia R, Jackson MR, Zhao J, Schaeffer JC. U.S. Patent #6, 306, 254. 2001.
13. Tryon B, Cao F, Murphy KS, Levi CG, Pollock TM. JOM 2006 in press.
14. Miracle DB. Metall Mater Trans A 1993;41:649.
15. Noebe RD, Bowman RR, Nathal MV. Int Mater Rev 1993;38:193.
16. Nabarro FRN, de Villiers HL, *The Physics of Creep*. 1995, Bristol: Taylor & Francis. 310.
17. Von Mises R. Z Angew Math Meth 1928;8:161.
18. Nandy TK, Feng Q, Pollock TM. Intermetallics 2003;11:1029.
19. Miicklich F, Ilic N. Intermetallics 2005;13:5.
20. Fleischer RL, McKee DW. Metall Trans A 1993;24A:759.
21. Wolff IM. JOM 1997;49:34.
22. Wolff IM, Sauthoff G. Metall Mater Trans A 1997;45:2949.
23. Fischer-Cripps AC, *Nanoindentation*. 2002, New York: Springer-Verlag.
24. Fleischer RL. Metall Mater Trans A 1993;24A:227.
25. Fleck NA, Muller GM, Ashby MF, Hutchinson JW. Acta Metall Mater 1994;42:475.
26. Evans AG, Stolken JS. Acta Mater 1998;46:5109.
27. Stelmashenko NA, Walls MG, Brown LM, Milman YUV. Acta Metall Mater 1993;41:2855.
28. Ma Q, Clarke DR. JOM 1995;10:853.
29. Nix WD, Gao H. J Mech Phys Sol 1998;46:411.
30. Lloyd DJ. Int Mater Rev 1994;39:1.
31. Fleck NA, Hutchinson JW, *Strain gradient plasticity*, in *Advances in Applied Mechanics*, Hutchinson JW,Wu TY, Editors. 1997, Academic Press: New York. p. 295.
32. Gao H, Huang Y, Nix WD, Hutchinson JW. J Mech Phys Sol 1999;47:1239.
33. Acharya A, Bassani JL. J Mech Phy Sol 2000;48:1565.
34. Gurtin ME. J Mech Phys Sol 2000;48:989.
35. Ashby MF. Phil Mag 1970;21:399.

36. Nye JF. Acta Mater 1953;1:153.
37. Sun S, Adams BL, King WE. Phil Mag 2000;80:9.
38. El-Dasher BS, Adams BL, Rollett AD. Script Mater 2003;48:141.
39. Biery N, De Graef M, Pollock TM. Metall Mater Trans A 2003;34A:2301.
40. Kobayashi AS, *Handbooks on Experimental Mechanics, Society for Experimental Mechanics, VCH*. 1993, New York.
41. Ziebs J, Bresers J, Frenz H, Hayhurst DR, Klingelhoffer H, Forest S. *Proceedings of the International Symposium on Local Strain and Temperature Measurement in Non-uniform Fields at Elevated Temperatures* 1996, Woodhead, Cambridge, UK.
42. Walker CA. Experimental Mechanics 1994:281.
43. Hartman G, Nicholas T. Experimental Mechanics 1987:24.
44. Wernicke D, Osten W, *Holografische Interferometrie, Physik Verlag, VEB Fachbuchverlag*. 1982, Leipzig.
45. Yamaguchi I. Opt Acta 1981:1359.
46. Wissucheck J, Mackin TJ, De Graff M. Experimental Mechanics 1996:173.
47. Demirel MC, Kuprat AP, George DC, Rollett AD. Phy Rev Lett 2003;90:016106.
48. Saylor DM, Fridy J, El-Dasher BS, Jung K-Y, Rollett AD. Metall Mater Trans A 2004;35A:1969.
49. Meibom R, Rupp EV. Z Phys 1933;82:690.
50. Boersch H. Z Tech Phys 1937;18:574.
51. Randle V, *Microtexture Determination and its Applications*. Second ed. 2003, London: Maney Publishing.
52. El-Dasher BS, *Dislocation-grain boundary interactions in columnar aluminum*, in *Materials Science and Engineering*. 2002, Carnegie Mellon University: Pittsburgh.
53. Tabor D, *The hardness of metals*. 1951, Oxford: Oxford University Press.
54. Bhushan B, *Handbook of micro/nanotribology*. 2nd ed. 1999, Boca Raton: CRC Press.
55. Bulychev SI, Alekhin VP, Shorshorov MKH, Ternovskii AP, G.D. S. Zavod Lab 1975:1137.
56. Fischer-Cripps AC, *Introduction to Contact Mechanics*. 2000, New York: Springer-Verlag.
57. Melngailis J. J Vac Sci Tech B 1987;5:469.
58. Stewart DK, Doyle AF, Casey JD, Jr. Proc SPIE 1995;2437:276.
59. Ward BW, Economou NP, Shaver DC, Ivory JE, Ward ML, Stern LA. Proc SPIE 1988;923:92.
60. Stewart DK, Stern LA, Foss G, Hughes G, Govil P. Proc SPIE 1990;1263:21.
61. Daniel JH, Moore DF, Walker JF, Whitney JT. Microelectronic Engineering 1997;35:431.
62. Brugger J, Beljakovic G, Despont M, de Rooij NF, Vettiger P. Microelectronic Engineering 1997;35:401.
63. Reyntjens S, Puers R. Journal of Micromechanics and Microengineering

2001:287.
64. Somani MC, Muraleedharan K, Birla NC, Singh V, Prasad RVRK. Metall Mater Trans A 1994;25A:1693.
65. Giannuzzi LA, Drown JL, Brown SR, Irwin RB, Stevie FA. Microscopy research and technique 1998;41:285.
66. Giannuzzi LA, Stevie FA. Micron 1999;30:197.
67. Lu DC, *The dislocation substructures and mechanical properties of RuAl-based intermetallics compounds*, in *Materials Science and Engineering*. 2000, Carnegie Mellon University: Pittsburgh.
68. Hirsch PB, Howie A, Nicholson RB, Pashley DW, *Electron Microscopy of Thin Crystals*. 1965, New York: Plenum Press.
69. Dawson PR, Mika DP. Acta Mater 1999;47:1355.
70. Buchheit TE, Wellman GW, Battaile CC. Int J Plast 2005;21:221.
71. Biery N, *Local deformation and bulk properties in Gamma-TiAl based alloys*, in *Materials science and engineering*. 2000, Carnegie Mellon University: Pittsburgh.
72. Gray GT, Pollock TM, *Strain hardening*, in *Intermetallic Compounds*, Westbrook JH,Fleischer RL, Editors. 2002, John Wiley & Sons, Ltd: West Sussex. p. 361.
73. Mills MJ, Miracle DB. Acta Metall Mater 1993;41:85.
74. Shen Z, Wagoner RH, Clark WAT. Acta Metall 1988;36:3231.
75. Lee TC, Robertson IM, Birnbaum HK. Phil Mag 1990;62:131.
76. Liu CT, Lee EH, McKamey CG. Metall Mater Trans A 1989;23:875.
77. Westbrook JH, Wood DL. J Inst Met 1962-63;91:174.
78. George EP, Liu CT. Metall Mater Trans A 1990;5:754.
79. Vitek V, Chen SP. Metall Mater Trans A 1991;25:1237.
80. Petton G, Farkas D. Metall Mater Trans A 1991;25:55.
81. Courtney TH, in *Mechanical Behavior of Materials*. 2000, McGraw-Hill Companies. p. 132.
82. Sigl LS, Exner HE. Metall Trans A 1987;18A:1299.
83. Sigl LS, Mataga PA, Dalgleish BJ, McMeeking RM, Evans AG. Metall Mater Trans A 1988;36:945.
84. Newkirk MS, Urquhart AW, Zwicker HR, Breval E. Metall Mater Trans A 1986;1:81.
85. Flinn BD, Ruhle M, Evans AG. Metall Mater Trans A 1989;37:3001.
86. Hing P, Groves GW. J Mater Sci 1972;7:427.
87. Odette GR, Deve HE, Elliott CK, Hasegawa A, Lucas GE. Interfaces in Metal-Ceramics Composites; Anaheim, California; USA; 18-22 Feb.1990 1990:443.
88. Pank DR, Nathal MV, Koss DA. Metall Mater Trans A 1990;5:942.
89. Ishida K, Kainuma R, Nishizawa T, Ueno N. Metall Mater Trans A 1991;22A:441.
90. Misra A, Gibala R. Metall Mater Trans A 1999;30A:991.
91. Huang S-C, Field RD, Krueger DD. Metall Mater Trans A 1990;21A:959.

92. Yang R, Leake JA, Cahn RW. in *High-Temperature Ordered Intermetallic Alloys V* 1993, Pittsburgh, Pennsylvania, p. 489.
93. Lee TC, Robertson IM, Birnbaum HK. Metall Trans A 1990;21A:2437.
94. Noebe RD, Misra A, Gibala R. Metall Mater Trans A 1991;31:1172.
95. Hill R, Rice JR. J Mech Phys Sol 1972;20:401.
96. Asaro RJ, Rice JR. J Mech Phys Sol 1977;25:309.
97. Dawson PR, Mika DP. Mater Sci Eng A 1998;257:62.
98. Barbe F, Cailletaud G, Decker L, Jeulin D. Int J Plasti 2001;17:513.
99. Shu JY, Fleck NA. J Mech Phys Sol 1999;47:297.
100. Fleck NA, Hutchinson JW. J Mech Phys Sol 1993;41:1825.
101. Fleck NA, Hutchinson JW. J Mech Phys Sol 2001;49:2245.
102. Uchic MD, Dimiduk DM, Florando JN, Nix WD. Science 2004;305:986.